CROSSTEX: A DESCRIPTION OF THE EXPERIMENTAL CONDITIONS, WAVE CLIMATE, AND INNER SURF ZONE HYDRODYNAMICS

A Thesis

Presented to the Faculty of the Graduate School

of Cornell University

in Partial Fulfillment of the Requirements for the Degree of

Master of Science

by

Peter J. Rusello

May 2007

ABSTRACT

The Cross Shore Sediment Transport Experiment (CROSSTEX) is a group of experiments examining sediment transport processes in the near shore environment with the goal of improving process based models for sediment transport. This is accomplished via large scale lab experiments utilizing advanced instrumentation, controlled, repeatable wave conditions, and a natural sand beach. One section of these experiments examined sediment transport in the swash zone, the alternating wet and dry portion of the beach, with the goal of examining the smallest scales of sediment motion, that of individual grains. The data collected in this portion of CROSSTEX will be used to develop and validate several numerical models under development at Cornell. Velocity data was collected from outside the breaker line into the surf zone, along with free surface measurements throughout the tank. Additional instrumentation to measure optical backscatter, sediment grain velocity and water pressure was deployed in the near shore. Waves consisted of regular, 5th order Stokes waves with wave heights ranging from 12 cm to 30 cm, two runs with a simple bi-chromatic wave train and one run with random waves. An analysis of wave climate stability and wave repeatability indicates the wave tank approaches a steady, repeatable wave climate after approximately 5 minutes although bathymetry changes ultimately affect repeatability in the near shore. Comparison of the time averaged mean free surface with empirical estimates shows good agreement with other studies conducted in both the field and wave tanks. Phase averaged velocity profiles taken in the offshore by an Acoustic Doppler Current Profiler (ADCP) indicate a 2-D flow environment with minimal

along shore flow and repeatable wave conditions. An alternate processing scheme was developed for the ADCP data to allow redundant estimates of each velocity component which was used to assess flow uniformity in the offshore. Phase averaged velocity data in the surf zone taken from Acoustic Doppler Velocimeters (ADVs) revealed occasional strong along shore flow and more complex flow structure, but supports wave repeatability. Analysis of the bathymetry data in the surf zone revealed strong along shore gradients, which contribute to the more complex flow seen in the surf zone. Surf zone turbulence obtained by applying a linear predictive filter to velocity signals and differencing the filtered and original signals indicates plunging to weakly plunging breaking conditions as well as providing order of magnitude estimates of dissipation. Recommendations for the conduct of future large scale experiments in the surf zone and future work on the present data are provided.

BIOGRAPHICAL SKETCH

Peter J. Rusello, or P.J. as he is more commonly known, received a Bachelor's of Science in Civil and Environmental Engineering from Cornell University in 2002. After graduating he began work as a research technician for Todd Cowen in the DeFrees Hydraulics Laboratory at Cornell, working with a variety of instrumentation and learning a great deal about experimental procedures. His motivation to study environmental fluid mechanics and coastal engineering stems largely from a love of being around water, but also from a desire to see natural resources managed more effectively. In his spare time he has been know to climb rocks, paddle various boats and drink beer. He recommends the use of zip ties, duct tape, and RoboGrips as essential tools in life. He may be contacted regarding this work at pjr25@cornell.edu

In her excellent book, *Against the Tide*, NY Times science editor Cornelia Dean details the history of coastal development, management and protection, and the unfortunate consequences of poorly informed decisions on these matters. Reading her account of a hurricane literally washing away Galveston Island, TX or the devastating effect of Hurricane Andrew on over developed, sand starved south Florida, it is easy to understand human desire to protect the coast. Reading about the consequences of coastal protection systems like groins used to trap sand, which starve beaches downstream of sediment, exacerbating their erosion problems, a quiet rage can build when something with such drastic consequences is still routinely used.

While it is easy to become overwhelmed by the complex nature of the coast and the numerous problems affecting it, this also serves as motivation for continued research into the processes governing the coastal environment. Only through understanding these processes can effective and well informed decisions about coastal policy and management be made. Dean closes her book with a challenge to scientists to effectively communicate their knowledge to policy makers and the public, so that better informed decisions can be made regarding the coast. It is in this spirit that this thesis is dedicated. While technical in nature, it is the author's hope it helps guide future researchers in the direction of better understanding the coastal environment and effective communication with the non-scientific community to sustainably live there.

ACKNOWLEDGEMENTS

I would like to acknowledge the help of the following individuals (in no particular order) throughout the course of my work on CROSSTEX: Todd Cowen, Javier Lopez Lara, Evan Variano, Russ Dudley, Phil Liu, Qian Liao, and Yong Sung Park from Cornell; Tim Maddux, Linda Fayler, Chris Scott, and Jason Magelan, Mick Haller and Tuba Ozkan-Haller from Oregon State; and Paul Devine from RDI. I'm sure several others that have slipped my mind at this point but I am no less thankful for all the help these now anonymous individuals provided.

These experiments were funded by the Nation Science Foundation under grant OCE-0452862.

Finally, I'd like to thank my venerable Apple Powerbook G4 for lasting through several cross country trips, a "vacation" in Hawai'i, a move across the county, several weeks "at sea", and many long nights of work, allowing me to finish my thesis with only one big scare.

TABLE OF CONTENTS

LIST OF FIGURES

LIST OF TABLES

Chapter 1

Introduction

The near shore environment, aside from being of strategic value as a buffer against storms for areas further inland, is also heavily used for commerce, recreation, habitation and unfortunately in many cases, waste disposal. There are many advantages to living near water, and it is essential to our success as a species. But we often take for granted what water and marine environments provide, only noticing their utility when a hurricane comes ashore or the dramatic beach scape in front of our multi-million dollar home erodes away during the course of a season.

It is water's utility and beauty that makes living on a coast attractive to so many people. A recent National Oceanic and Atmospheric Administration (NOAA) report entitled *Population Trends Along the Coastal United States: 1980-2008* (Crossett et al., 2005), estimated 53% of the nation's population lived in a coastal county in 2003. While this proportion has remained relatively constant for the past several decades, the population density in the limited area of the coastal counties continues to increase as the total United States population increases. The current average population density in coastal counties is three times higher then the national average (300 vs. 98 persons per square mile) and only expected to increase.

As population and population density increase along the coast, a greater demand is placed on the environment and the limited resources found there. A recent study by Leatherman et al. (2003) stated 90% of U.S. sandy coasts are eroding. Along the U.S. east coast, beaches are eroding at an average rate of almost 1 meter per year. As beaches erode, the costs associated with protecting or repairing

coastal infrastructure and maintaining navigable waterways increase significantly. As coastal infrastructure increases (or sometimes doesn't in the case of treatment capacity for waste water facilities) further environmental demands are placed on coastal environments and their ability to handle the environmental impact without significant degradation decreases. Their is an economic and environmental cost associated with each of these scenarios.

In recent years, hurricanes have caused increasing amounts of damage. NOAA reports 23 hurricanes in the 20th century have caused in excess of $1 billion in property damage alone (Jarrell, retired). Hurricane Katrina, which came ashore near New Orleans, LA in August 2005, is estimated to have caused over $100 billion in damage, quadrupling the previous high of $25 billion caused by Hurricane Andrew in 1992. The fiscal year 2007 budget for the Army Corps of Engineers seeks $1.9 billion for commercial navigation projects and $1.3 billion for flood and storm damage protection. These two areas comprise almost 70% of the ACE's budget, but there is a 20 year backlog of projects awaiting funding and work. Simply increasing the ACE's funding won't remedy these problems however, as they have proven all to often to be part of the problem when it comes to coastal development (Dean, 2001).

There is still a large amount of research to be done understanding the fundamental processes governing how the coast behaves. Near shore hydrodynamics and sediment transport, the subject of a large body of research, are still poorly understood and have in reality only been studied under a limited set of conditions. Understanding the fundamental processes behind shoreline change, sediment transport and near shore hydrodynamics is the first step in being able to develop effective management practices for the near shore environment.

The present work examines a series of experiments conducted in the Large Wave Flume at the O.H. Hinsdale Wave Research Laboratory located on the campus of Oregon State University in Corvallis, OR. This series of experiments, collectively known as the Cross Shore Sediment Transport Experiment (CROSSTEX), examines cross shore sediment transport at a variety of scales through various regions of the near shore environment. Utilizing existing commercial instrumentation from the laboratory and field and newly developed systems (e.g. a boroscope based PIV system), a more thorough examination of turbulence, sediment suspension and transport was undertaken at near prototype scales under controlled laboratory conditions.

1.1 The Swash Zone

One of the nearshore regions under study is the swash zone, the alternating wet and dry region of the beach where sheet flow dominates the hydrodynamics and sediment transport. High levels of turbulence and complex boundary conditions caused by a porous, mobile bed make the swash zone a difficult region to model with fundamental equations. Those same flow conditions, aeration brought upon by wave breaking and turbulence, and the difficulty of making detailed measurements at scales small enough to capture the fundamental processes occurring in the swash complicate the study of this region experimentally. Yet most erosion and accretion occurs in the swash zone, which on a natural beach can cover tens of meters over a tidal cycle. Simply making due with present models and data will not suffice.

Field experiments (e.g. DUCK94, SandyDUCK, NCEX) have been successful in examining large scale morphological changes, quantifying turbulence, and providing estimates of the mass flux in the swash. Sediment transport rates have been

measured as high as 10 kg/s per meter, higher then rates associated with regions further offshore (Beach and Sternberg, 1991) (Beach et al., 1992), (Katori, 1983), (Thornton and Calhoun, 1972), and (Watts, 1953). Despite these experiments, the swash remains poorly understood, with fundamental mechanisms involved in sediment suspension and transport unknown or unverified experimentally.

Several large scale lab experiments (SUPERTANK, SISTEX) have been conducted in an attempt to quantify and develop models for sediment transport processes by either making measurements in the swash zone or examining similar flow conditions (i.e. sheet flow) in an easier measurement environment. SUPERTANK, sponsored by the Army Corps of Engineers and conducted in the Large Wave Flume at Oregon State University examined undertow (a return flow near the bed generated by conservation of mass), dune erosion, accretion, scour around objects, bar formation and mesoscale morphological changes, as well as swash zone dynamics. The swash zone results from SUPERTANK focused mainly on wave characteristics and sediment grain size distributions, but did not identify the fundamental transport mechanism in the swash or examine sediment grain velocities.

The Small-scale International Sediment Transport Experiment, SISTEX, conducted in the summer of 1999 at the Large Wave Flume at the Forschungs Zentrum Küste in Hanover, Germany, examined near bed sediment transport in the sheet flow region under large waves. Novel instrumentation, specifically a conductivity concentration meter (CCM), was used to measure the concentration and grain velocities in the sheet flow region. Despite the success of SISTEX and the CCM results, the smallest scales of sediment transport have still failed to be resolved, i.e. the motion of individual grains. The measurements during SISTEX also applied only to a flat bed under non-breaking wave conditions. Earlier experiments which

examined sediment transport under breaking waves or near the bed had similar limitations like SISTEX. They were conducted under limited conditions, measurements were taken well offshore, and only low frequency motion was examined due to instrument limitations.

There is no numerical model which has been verified to accurately capture the spatial and temporal structure of turbulence in the swash zone. Modeling sediment transport in the swash zone has lagged behind modeling of the hydrodynamics. Until recently, sediment transport models relied exclusively on the decades old model proposed by Bagnold (Bagnold, 1954) (Bagnold, 1963) (Bagnold, 1966). A primary goal of CROSSTEX: Swash Zone Hydrodynamics and Sediment Transport is to study the small scale sediment transport in the swash zone and test and refine a two phase sediment transport model under development at Cornell University.

As part of the study of swash zone hydrodynamics, a large suite of instrumentation was utilized to characterize the wave climate, bed morphology and provide boundary conditions for the modeling efforts. The present analysis focuses on a description of the wave climate, focusing on wave repeatability, time scale at which the flow becomes stable, and inner surf zone turbulence and it's evolution into the swash zone.

1.2 Surf Similarity and Wave Breaking

Turbulence and bed stress are two important factors in sediment re-suspension and transport. Turbulence generated by breaking waves is the major contributor to the turbulent kinetic energy available to resuspend sediment in the near shore environment. Ting and Kirby (1994) showed quantitative differences in the turbulence under spilling and plunging breaking waves, making it important to know under

what wave breaking condition measurements are made. Many researchers have examined wave breaking and we have available several predictors of how, where and under what conditions a wave will break.

The most common parameter used when discussing wave breaking is the Iribarren number or surf similarity parameter defined by Battjes (1974) as

$$\xi = \frac{\tan(\alpha)}{\sqrt{\frac{H}{L_o}}} \tag{1.1}$$

Where α represents the beach slope, H is the incident wave height and L_o is the deep water wavelength. The Iribarren number, so called because it was first proposed by Iribarren and Nogales in 1949, expresses the ratio of beach slope to wave steepness (the quantity $\frac{H}{L_o}$). Like many dimensionless parameters, there is a certain critical value past which something, in this case wave breaking, will occur. A large number of lab experiments have shown that when ξ falls below the value 2.3, wave breaking will commence. This says that when the wave is sufficiently steep compared to the beach slope, the wave will break. Waves with low steepness or approaching a beach with a very steep slope will not break, and either be completely reflected (a completely vertical beach), or will simply surge onshore without the obvious signs of breaking such as white water and air entrainment.

Further work by Galvin (1972) allows classification of breaking waves into three main categories. The values given for ξ below are only approximate as there are many factors governing the type of breaking a wave will experience, not all of which are understood or parameterized at this point.

For $0.4 < \xi < 2.3$, plunging waves, the classic tube or barrel seen in surfing photos, is likely to occur. Plunging occurs when the wave shape becomes asymmetric and the crest curls forward, forming a prominent jet that plunges into the

trough of the preceding wave.

For $\xi < 0.4$ a spilling breaker will occur. Spilling generally occurs over milder slopes with steeper waves. The wave retains its shape, but foam, bubbles, and turbulence form at the crest of the wave and spill down the face into the trough of the preceding wave.

When $\xi > 2.3$ a collapsing breaker will occur. Collapsing generally occurs very near the shore, when only the face of the wave steepens and forms an abbreviated plunger.

For the present study, a mildly plunging breaking wave was sought ($\xi \approx 0.6$). This type of breaking wave provides high turbulence levels in the inner surf, turbulence generated by the breaking wave can be expected to propagate onshore, and a well formed sheet flow region in the swash zone will develop. It also allows comparison with prior work in the swash zone conducted over an impermeable glass bed (Cowen et al., 2003) (Sou, 2005).

Chapter 2

Experimental Setup, Methods and Error Analysis

2.1 Facility Description

Experiments were conducted during September 2005 in the Large Wave Flume at the O.H. Hinsdale Wave Research Lab at Oregon State University located in Corvallis, Oregon. The Large Wave Flume (LWF) was constructed in 1972 for large scale study of coastal structure stability. In it's 30+ years of operation it has been used to study cross-shore sediment suspension and transport, wave forces on offshore and coastal structures, nearshore hydrodynamics, wave breaking, swash dynamics, undertow, and tsunamis. It is generally assumed to provide a simplified, two dimensional system with no significant cross tank (along shore) gradients present.

The LWF is equipped with a hinged, hydraulic ram actuated wave paddle manufactured by MTS Systems Corporation of Eden Prairie, Minnesota. The wave paddle is controlled by a dedicated computer running a special control software provided by MTS. This software has built in capabilities to generate various regular waves (e.g. 5th Order Stokes), irregular waves, or a user defined wave specified as a time series of wave heights at the paddle. Waves can be generated with periods ranging from 0.5 to 10 seconds and up to a maximum wave height of 1.6 meters. Although equipped with Active Wave Absorption to minimize reflected wave energy, it was not employed in these experiments. An elevated control room houses a computer running the wave maker software, providing a view of the entire

tank.

The LWF is 104 meters long, 3.7 meters wide, and 4.6 meters deep, with a working section of 76 meters. It is constructed of reinforced concrete, with approximately 1 meter rising above ground level and the remaining portion of the tank below ground. Pairs of bolt holes, spaced 8 inches apart with 12 feet between pairs horizontally divide the tank into bays numbered 1 through 21. Bay 1 is located the furthest from the wave paddle. The bolt holes are used for mounting instrumentation at various elevations, with pairs of bolt holes spaced every foot in the vertical.

A Cartesian coordinate system was established following the right hand rule, with $x = 0$ located at the wave paddle's vertical position, $y = 0$ located at the inside of the right wall when looking away from the wave paddle, and $z = 0$ located at the top of the tank wall. Thus, any elevation inside the tank will be a negative value. All coordinates are given in this system.

For CROSSTEX, the LWF was filled with sand sourced from a quarry on the Oregon coast. Sieve analysis showed a $D_{50} = 0.29$ mm with a grain size distribution as in Figure 2.1 for sand sampled in the swash zone. Other samples taken in areas further offshore and processed by Oregon State researchers showed a mean $D_{50} = 0.22$ mm (Scott and Magelan, personal communication), while a sample taken at the still water line showed a $D_{50} = 0.27$ mm.

A typical bathymetry is shown in Figure 2.2. Slope in the offshore section is typically $\approx \frac{1}{12}$. After a transition near the breaker line, the inner surf zone has a slope of $\approx \frac{1}{60}$. The swash and dry beach have a slope of $\approx \frac{1}{14}$. These slopes remained relatively constant through the three week experiment period, with the bed exhibiting no large scale changes in morphology except at the breaker line

where a trough formed under the plunging section of the breaking wave. Still water depths (measured from the bottom of the tank) varied from 3.17 to 3.35 m during the three week swash experiments, placing the still water shoreline between 83-85 m from the wave paddle.

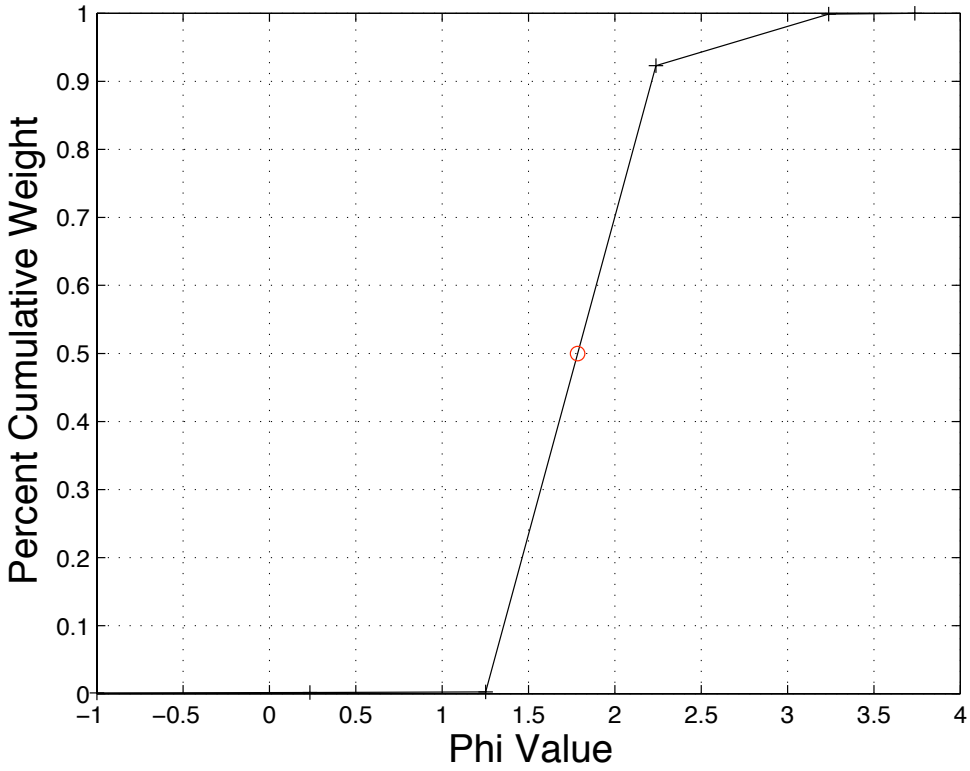

Figure 2.1: Grain size distribution. Phi value for $D_{50} = 0.29$ mm marked with ○.

2.2 Data Collection and Instrumentation

While principally concerned with sediment transport and turbulence in the swash zone, the experiments conducted also hoped to characterize the flow, sediment

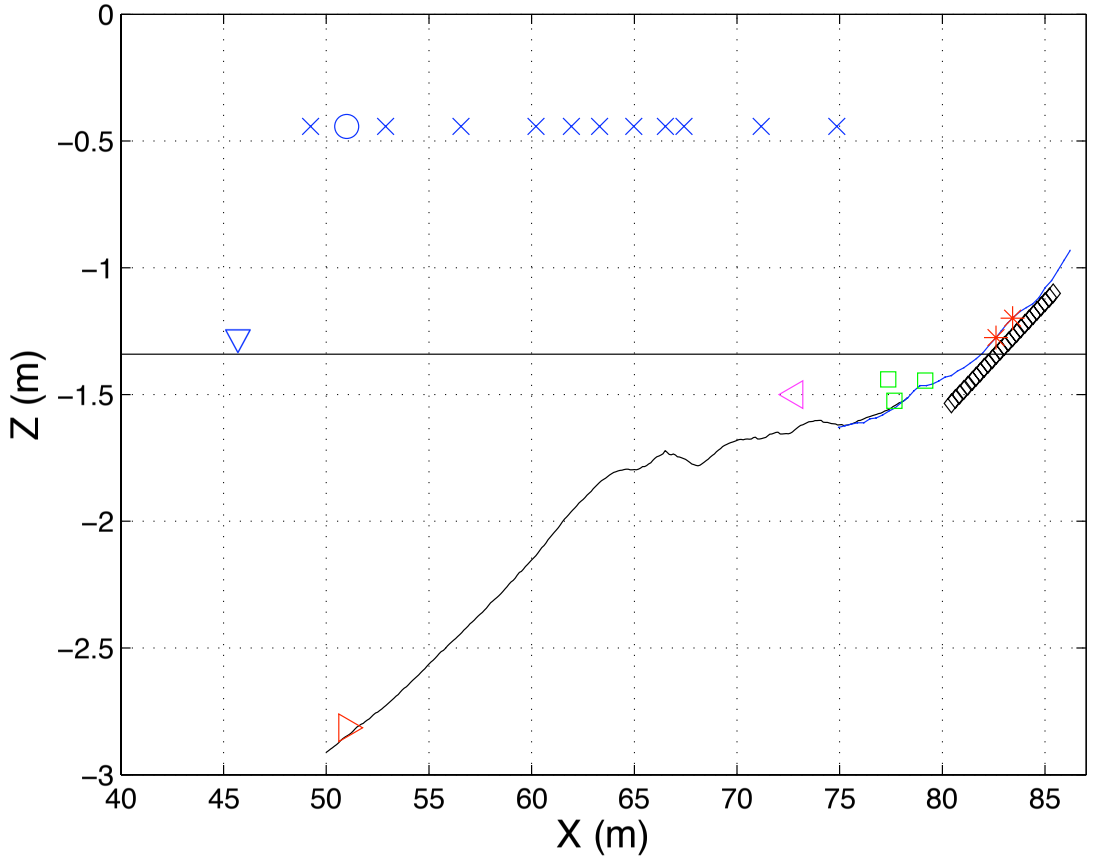

Figure 2.2: Example bathymetry with instrument locations. ▷ ADCP; ◁ Cart ADVs; □ Frame ADVs; ∗ PIV system; ◇ Pressure Sensor; × Wave Gage; ○ Q45U

transport and morphological changes in the bed in the inner surf zone for modeling efforts. Instrumentation was deployed throughout the tank to measure free surface displacement, velocity, sediment concentration, pore water pressure, and sediment and water velocity in the sheet flow region of the swash zone. Each measurement type, the instrumentation used, and the data collection goal is presented below. Specific principles of operation, measurement accuracy and uncertainty, and instrument setup (where applicable) will also be discussed in later sections.

Instrumentation consisted of primarily two types, those which produced an analog voltage output and were recorded on one of three analog data acquisition systems (DAQ) and those requiring proprietary software to operate and record data. One of the analog DAQs was a Personal Computer Interface (PCI) Extensions for Instrumentation (PXI) system provided by Oregon State University. The other two systems were based on National Instruments SCXI hardware and run at the offshore boundary station and swash zone station by Cornell University.

The Oregon State maintained DAQ was based on a National Instruments PXI-1052 chassis with SCXI-1143 lowpass Butterworth filter modules and SCXI-1305 terminal blocks installed. The hardware filters were set with a cutoff frequency of 12.5 Hz, providing a flat frequency response out to 10 Hz and minimal phase delay. The PXI-1052 chassis functions in place of a computer equipped with a data acquisition card. It features an onboard controller running LabView Real-Time to handle data acquisition, and supports signal conditioning, filtering etc. The terminal blocks use multiplexing, or assigning each signal a specific frequency or time slot in a rotation, to allow multiple signals to be collected on one data acquisition channel. They feature BNC (Bayonet Neill Concelman) connectors on the front for use with coaxial cables, allowing quick setup and easy interchange

between sensors. Two PXI systems were operated, one designated the master and producing the timing signals used to trigger sampling on some instrumentation, and the other designated a slave system, beginning sampling upon receipt of a signal from the master. Both PXI systems were controlled using National Instruments Labview software.

At the offshore boundary station, a National Instruments DAQCard-6024E was used to record various analog voltage signals. This PCMCIA card was installed in a Pentium III laptop, and connected via a shielded cable to a small breakout terminal board with screw terminals. The card provides 16, 12-bit single ended inputs (8 differential), 2 analog outputs, 2 24-bit counter/timers, and 8 digital input/output lines. Only the differential inputs were used, with data recorded to a column based text file using National Instruments Labview software.

At the swash station, a National Instruments PCI-6023E providing 16 12-bit single ended analog inputs (8 differential), 8 24-bit digital input/output lines, and digital triggering, was installed in a dual Pentium III based desktop computer. Attached to the PCI-6023E was a SCXI-1000 chassis containing two SCXI-1100 modules, providing 32 $\pm$ 10V multiplexed channels per module (64 total). The SCXI-1100 module multiplexes multiple analog input channels which are then fed into one channel on the PCI-6023E, which filters the combined signal and records each separately. Only analog input functions were used, with data recorded to a column based text file.

Instruments requiring proprietary software to operate were run on the same computing hardware as the two Cornell DAQs as appropriate to their deployment location. Manufacturer's proprietary software was used to configure the instruments and collect data. Once data collection was stopped, additional software was

used to export the proprietary binary formats used by the manufacturers to more usable text based data files, or when available directly to MATLAB's binary data format.

Synchronization of the various data streams was accomplished in the post processing stage. The wave paddle driving voltage was recorded on the various DAQs to provide a common signal for synchronization. Instruments which required proprietary software to operate or record data were generally capable of providing a TTL pulse for synchronization which was recorded on the appropriate DAQ giving at minimum a start time relative to the common wave paddle signal. In cases where the TTL pulse was not recorded or available, the unique ramp up or ramp down signature of the wave height at the beginning and end of wave runs was used in conjunction with already synchronized measurements to synchronize a time series.

A summary of the various instrumentation described in this section is presented in Table 2.2.5 at the close of the section.

2.2.1 Bathymetry

Two different survey techniques were used to conduct bathymetry surveys. The dry beach, swash, and very shallow (< 10 cm water depth) inner surf were surveyed by hand using a regular grid and a survey staff. Readings were taken relative to the deck of a small cart pushed by hand on the level side walls of the flume, with readings taken at one foot intervals. Three separate cross shore survey lines were taken, approximately one quarter, halfway and three quarters across the tank. Each survey line consisted of twenty points spaced 1 foot (.3048 m) apart. Early surveys used only the center survey line with the same one foot grid for cross shore point spacing.

The majority of the tank was surveyed with a Multiple Transducer Array (MTA) manufactured by Seatek Instrumentation and Engineering of Alachua, Fl (www.seatek.com). The MTA consists of 32, 2 MHz acoustic transducers arranged in a linear array spanning 2.55 meters. The array was mounted on the offshore side of the large cart seen in Figure 2.3. From the right wall looking onshore, the first transducer was centered 0.66 m from the wall. The last transducer was centered 0.49 m from the left wall, looking onshore. Each transducer is capable of resolving millimeter scale vertical changes in the bed elevation over a range of 5 cm to several meters.

Each transducer provides a range measurement in a line running the length of the tank, which is output via RS-232 to a terminal program. The along tank position was measured using a laser range finder mounted to the top of the cart. The laser range finder measures the distance to a target (in this case a white board mounted to the wall of the lab) by measuring the time for a reflection to return to the receiver. Generally, the laser is pulsed to improve measurement accuracy and reduce interference. Distance to target is output via RS-232. A National Instruments Labview program combined and synchronized the two RS-232 data streams from the MTA and the laser range finder and recorded them to a plain text file.

Horizontal resolution was governed by the speed of the survey cart in the cross shore direction and the sample frequency of the MTA. For instance, with an output rate of 1 Hz and a cart speed of 5 cm/s, raw MTA survey data provides 5 cm resolution in the cross shore direction. Along shore resolution was set by transducer spacing, fixed at 8 cm by the manufacturing process of the transducer arrays. After processing, along shore resolution remained 8 cm, while the cross shore data was

Figure 2.3: View of the inner surf zone with instruments deployed. The three wings on which the ADVs were deployed are visible at the rear of the cart. The Multiple Transducer Array is visible just under the offshore side of the cart. It was lowered into water at the start of each survey. Just onshore of the cart the frames holding the three inner surf Vectrinos can be seen.

Table 2.1: Summary of free surface measurement locations. Resistance wave gages are designated by a number (0-12). The Q45U ultrasonic measurement is labeled "Q45U".

Wave Gage #	0	1	2	3	4	5	6
Position (m)	0	19.99	49.23	52.89	56.56	60.21	61.94
Wave Gage #	7	8	9	10	11	12	Q45U
Position (m)	63.31	64.98	66.51	67.42	71.18	74.86	51

interpolated onto a 10 cm grid reducing it's nominal resolution by half. Based on acoustic theory, the beam divergence (the angle measured in the far field from transducer centerline to the main lobe of the beam) angle is calculated as 1.1°. Based on this beam divergence, at 1 m, the beam is sampling an area with a radius of 6 cm. The area sampled will decrease with depth.

2.2.2 Free Surface Measurements

Resistance wave gages were deployed from the wave paddle through the inner surf to measure free surface displacement. An analysis of the overall wave climate, its stability, reflected energy and other diagnostic measures can be carried out with this data. Resistance wave gage positions are summarized in Table 2.2.2, along with the position of a single ultrasonic free surface measurement discussed later in this section. Wave Gage 0 (WG0) was mounted directly on the wave paddle for system feedback. Gages were placed approximately every bin around the offshore boundary station with a more dense spacing in the inner surf zone. The closest gage to the swash zone was over 5 m away.

The resistance wave gages were recorded on the Oregon State PXI DAQ. Each

gage outputs a voltage between ± 5V, which is recorded and later converted to a wave height measurement. The response of these gages is linear, so calibration involves taking readings at various known water elevations and recording the voltage output. A best fit line is obtained from all valid water elevation levels at a gage, and a slope is determined for each gage to convert from volts to a length measurement (e.g. meters). No offset is provided for the gages, so only relative changes in the free surface are available. It is not possible to determine the actual water level in the tank from the wire wave gages.

An ultrasonic range gage manufactured by Banner Engineering, model Q45U with analog outputs, was deployed at the offshore boundary station ($x = 51$ m). The Banner Q45U is a linear analog output instrument, with a response between 0-10V. This voltage output was recorded on the Cornell DAQ located at the offshore station.

A near and far sensing limit set the range over which the output voltage is distributed. The nearest detectable range is 0.1 meters and the furthest range is 1.4 meters, with a resolution of 0.25 mm. After setting the near and far sensing limits, the slope of the response can be determined and the appropriate offset applied for calibration. Depending on the order in which limits are set, the Q45U will output a negative or positive slope signal. The sign of the slope determines whether the output voltage is in phase or out of phase with the true free surface displacement (i.e. whether a dropping voltage actually represents a drop in the free surface).

The Q45U will not work in areas with large amounts of white water (such as in the breaking wave region and inner surf) or where the reflecting surface is inclined more then 10 degrees from the transducer face due to loss of return signal. But

in the offshore region, because of its acoustic measurement technique, the Q45U provides a zero drift free surface measurement. The analog voltage output from the Q45U was recorded by the Cornell laptop DAQ at the offshore location.

2.2.3 Offshore Boundary Station

An Acoustic Doppler Current Profiler (ADCP) manufactured by Teledyne-RD Instruments of San Diego, CA was buried in the bed at $x = 51$ m in the middle of the tank to provide a full water column velocity profile in three components. The Banner Q45U measured the free surface displacement above the ADCP.

The ADCP utilizes the Doppler shift to measure velocity along the path of an acoustic beam, referred to as a radial beam velocity. By using various pairs of beams, it is possible to estimate velocity vectors in a variety of coordinate systems from the radial beam velocities. By paying attention to orientation of the acoustic beam paths, additional information about the flow beyond basic velocity information can be measured. The ADCP velocity estimates will be discussed fully in §2.4.

Co-located and also buried in the bed was a Nortek Vector Acoustic Doppler Velocimeter (ADV), manufactured by NortekAS of Norway. The head of the ADV was oriented looking up to measure near bed velocities. ADVs utilize the Doppler shift to measure water velocity, similar to the ADCP. However, they only measure the velocity at a single point instead of in a profile and in a much smaller volume of water and with much higher temporal resolution then the ADCP is capable of. The Vector ADV was positioned near the ADCP to provide a check on the ADCP velocity measurements and a more accurate measurement of the bed stress and turbulence in the offshore. Principles of operation for the ADV will be discussed

in §2.5.

2.2.4 Inner Surf Zone

Eight Nortek Vectrino ADVs were mounted in a vertical stack on three seperate wings of the large cart visible in Figure 2.3 at $x = 72.82$ m. The vertical spacing of the Vectrinos was logarithmic in nature, with tighter spacing near the bed. Relative horizontal and vertical spacing is provided in Figure 2.4. The spacing between the sample volumes of each sensor was fixed at the time of mounting, but the entire array was positionable throughout the water column by repositioning vertically the wings upon which the ADVs were mounted. The cart the wings were mounted on was also positionable along the tank, and the ADVs were placed just inside the breaker line to provide velocity and turbulence measurements there. In contrast to the Nortek Vector and the remaining three ADVs discussed below, the cart ADVs employed triggered sampling, called "sample on synch" by Nortek, where upon receipt of a TTL pulse, the ADV records a sample. Velocity is averaged over the period between pulses the same as for normal, un-triggered operation.

Also mounted on each wing was an Optical Back Scatter sensor (OBS), model OBS-3 manufactured by D&A Instruments of Port Townsend, Washington. The OBS-3 uses the optical backscatter method (ASTM 6677) to measure turbidity and suspended sediment concentrations. Using an pulsed infrared light source, the OBS-3 directly measures the intensity of light scattered back to a receiver and reports this as an analog voltage. It's response must be calibrated at known sediment concentrations using sediment either the same or very similar to the type expected to be measured. It has a nearly linear response over a thousand fold change in sediment concentration and turbidity, with a maximum concentration

before saturation of approximately 50 g/L of sand. Four OBS-3 were also buried in the bed just inside of the cart wings in an attempt to measure sediment concentration near the bed. These sensors proved of limited utility as they were routinely buried by bed forms.

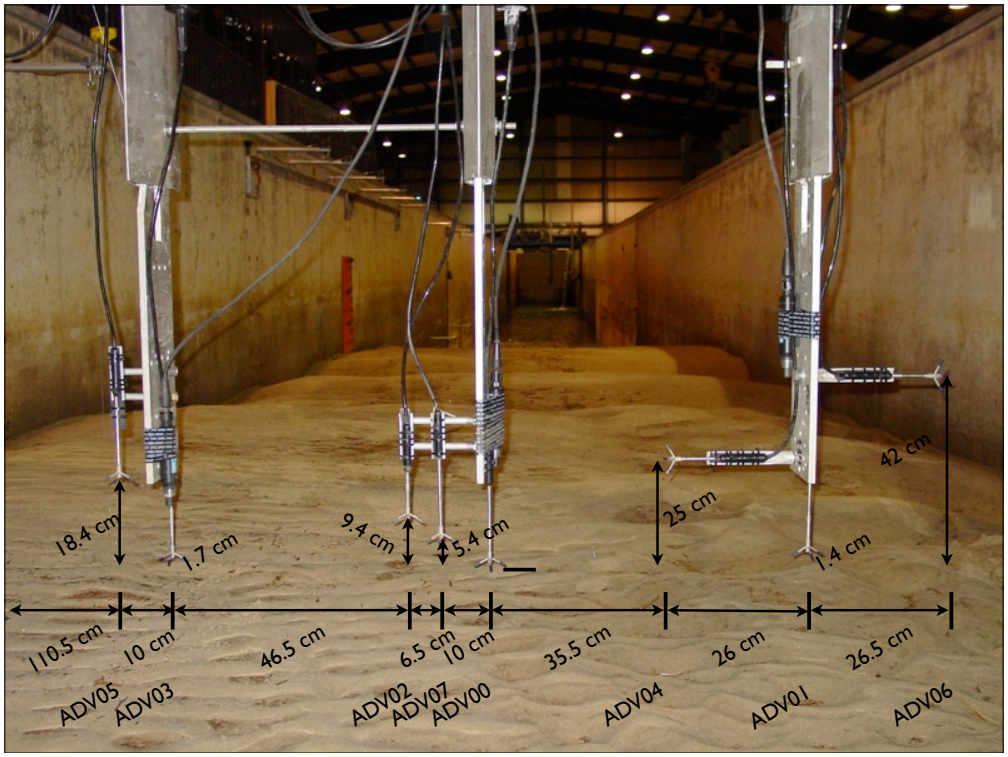

Figure 2.4: View looking offshore of the cart wings. Horizontal and vertical spacing for each of the ADVs from the right wall (looking onshore) is provided below. ADV numbering was arbitrary and assigned by the control software used to trigger the sampling.

Just inside of the cart's location, three Nortek Vectrinos were deployed on two seperate frames in the inner surf. The first frame was located at $x = 77.3$ m, with a pair of ADVs mounted on it. The lower ADV was positioned with its sample

volume approximately 2 cm above the bed. The second ADV was positioned further up in the water column, between 5 to 10 cm above the lower ADV's sample volume. The second frame was deployed further onshore at $x = 79.2$ m, with a single ADV positioned so its sample volume was approximately 2 cm above the bed. Again, the reader is referred to §2.5 for a discussion of ADV measurement error.

2.2.5 Swash Zone

Buried in the bed of the swash zone, three Boroscope Quantitative Imaging Profiler (BQuIP) systems were deployed to capture sediment particle and water velocities. Their operation and data will not be dealt with in this thesis.

Mounted above the BQuIP systems were ultra-sonic range gages similar to the Banner Q45U. These gages, Banner Engineering model S18U with analog voltage outputs, operate on the same principles as the Q45U, but have a shorter sensing range. They provide a relative measure of the beds accretion or erosion throughout a wave run, as well as providing a somewhat imprecise measure of the sheet flow thickness. Assuming only minimal accretion or erosion occurs during the course of a single wave, the distance to bed measurement prior to the arrival of a the bore and the water surface measurement during the downrush phase can be used to determine an approximate sheet flow thickness.

For several experiments, a linear array of pressure sensors was buried in the bed of the swash zone, spanning the region the BQuIPs were buried in. These sensors allow maximum runup height and depth of the sheet flow to be determined in conjunction with the bathmetry surveys and S18U range data. The sensors are Omega Engineering model PX26-005DV wet/wet differential pressure sensors, with

a .35 bar maximum pressure, manufactured by Omega Engineering of Stamford, Conneticut. They are based on silicone strain gage technology, were a strain gage bonded to a silicon membrane measures the deflection of the membrane under a differential pressure. They were potted in a two part urethane compound to allow submersion in water, with one side vented to atmospheric pressure and the other screened to protect against sand grains clogging the port to measure the hydrostatic pressure above the sensor. These sensors produce a mili-volt output calibrated to their excitation voltage and were sampled on the swash zone analog DAQ system at 100 Hz. Factory calibrations were used based upon the excitation voltage provided to each sensor.

2.3 Experimental Procedures

Because data file size for a majority of the instrumentation used was small, all instruments except for the boroscope systems started collecting data prior to waves being generated. A typical sequence involved starting the DAQ in the swash zone, starting the three frame ADVs (synched to start collecting data together), starting the offshore DAQ, starting the ADCP and ADV in the offshore, then moving to the elevated control room to start the Oregon State DAQ (where the cart ADVs, resistance wave gages and OBSs were recorded). Once all instruments were verified to be operating correctly, waves were started and allowed to run for anywhere from 10 to 40 minutes.

Wave conditions varied slightly throughout the experiments, but consisted almost exclusively of fifth order Stokes waves with a period of T=6 seconds. Wave heights were varied to provide more or less energy to the swash zone and vary the conditions under which PIV image sets were taken. The smallest wave height used

Table 2.2: Summary of instrumentation deployed during CROSSTEX, including location, output type, sample rate and any notes relevant to the system.

Instrument	Location	Sample Rate	Output	Recorded at
Wave Gage	see Table 2.2.2	50 Hz	Analog Voltage	OSU Analog Master
Q45U	$x = 51$ m	100 Hz	Analog Voltage	Offshore DAQ
S18U	Co-located with boroscopes	100 Hz	Analog Voltage	Swash Zone DAQ
OBS	$x = 72.82$	50 Hz	Analog Voltage	OSU Analog Master
ADCP	$x = 51$ m	2-4 Hz	Binary	Offshore Station
Cart ADV	$x = 72.82$	50 Hz	Binary	OSU DAQ
Frame ADV	$x = 77.36, 77.66, 79.16$	192 Hz	Binary	Swash Station

was $h = 12$ cm, while the largest was $h = 30$ cm. Two data runs consisted of a simple bi-chromatic wave train and one run was conducted with a random wave field based on the TMA spectra. A summary of the data runs ($N = 25$) is provided in Figure 2.5.

2.4 ADCP Velocity Measurements

The ADCP deployed in the offshore has several assumptions underlying it's use; principle among these is the assumption of horizontal homogeneity in the flow. As the distance from the transducer increases, the separation between the beam velocity measurements used to calculate the orthogonal velocity components increases. If the flow is not nearly homogenous in the horizontal, large errors can result in the velocity components determined from the beam velocities. In the LWF this assumption is not significantly violated, even at the reduced scale of these experiments compared to typical field measurement applications. A comparison of the beam spread at the surface (≈ 2 m) to the typical wave lengths examined in the various wave runs (≈ 22 m) shows an order of magnitude difference in scale. It is therefore expected each cross-shore pair of beams, even under the steepest part of the wave, will measure a very similar velocity.

In the following sections the method used to calculate the various velocity components, consequences of the assumptions made in its deployment, the reason for its orientation, and the additional information gained by deploying it in this manner will be presented. We start with a brief discussion of some basic principles of operation and terminology.

RUN #	Date	Time	Duration (min)	Wave Climate	Water Depth (ft)	OSU_D AQ #	Frame ADVs	Pressure	S18U (# deployed)	Q45U	ADCP	Vector	Survey Before	Survey After
1_1_1	17-Sep	1400	15	Stokes H20cm T6s	10.6	1	Y	NA	0	Y	M11	Y	N	N
2_2_2	17-Sep	1450	15.5	Stokes H20cm T6s	10.6	2	Y	NA	0	Y	M11	Y	N	N
3_3_3	17-Sep	1540	15	Stokes H20cm T6s	10.6	3	Y	NA	1	Y	M11	Y	N	N
4_4_4	17-Sep	1635	20	Stokes H20cm T6s	10.6	4	Y	NA	1	Y	M11	Y	N	N
5_1_3	19-Sep	1540	15	Stokes H20cm T6s	10.55	3	Y	NA	1	Y	M11	Y	091905_1354	N
6_2_4	19-Sep	1630	15	Stokes H20cm T6s	10.55	4	Y	NA	1	C	M11	Y	N	N
7_3_5	19-Sep	1700	20	Stokes H20cm T6s	10.55	Failed	Y	NA	1	C	M11	Y	N	N
8_1_1	20-Sep	1600	13	Stokes H20cm T6s	10.6	1	Y	NA	1	S	M11	Y	092005_0950	N
9_2_2	20-Sep	1630	16	Stokes H20cm T6s	10.6	2	Y	NA	1	C	M11	Y	N	N
10_3_3	20-Sep	1720	15	Stokes H20cm T6s	10.6	3	Y	NA	1	C	M11	Y	N	N
11_4_6	20-Sep	1750		Stokes H20cm T6s	10.6	6	Y	NA	1	C	M11	Y	N	092105_0848
12_1_1	21-Sep	1500		Stokes H12cm T6s	10.8	1	N	NA	1	Y	M11	Y	092105_1205	N
13_1_2	22-Sep	1421	15	Stokes H12cm T6s	10.9	2	Y	NA	2	C	M11	Y	092205_1015	092205_1455
14_2_3	22-Sep	1640	21.5	Stokes H12cm T6s	10.5	3	Y	NA	2	C	M11	Y	092205_1455	092205_1728
15_1_1	23-Sep	949	27	Stokes H12cm T6s	10.5	1	Y	NA	2	S	M11	Y	092205_1728	092305_1036
16_2_5	23-Sep	1238	39	Stokes H12cm T6s	10.5	5	Y	NA	2	C	M11	Y	092305_1036	092305_1355
17_1_2	24-Sep	1010	17.5	Stokes H16cm T6s	10.6	2	Y	Y	2	C	M11	Y	092305_1355	092405_1100
18_2_3	24-Sep	1301	10	Stokes H20cm T6s	10.6	3	Y	Y	2	C	M11	Y	092405_1100	092405_1355
18_2_3	24-Sep	1313	13	Stokes H20cm T6s	10.6	3	Y	Y	2	C	M11	Y	092405_1100	092405_1355
19_3_4	24-Sep	1455	10	Stokes H16cm T6s	10.6	4	Y	Y	2	C	M11	Y	092405_1355	
20_1_1	28-Sep	1338	18.5	Stokes H12cm T6s	11	1	Y	Y	2	S	M11	Y	092705_1312	092805_1442
21_2_2	28-Sep	1553	30	Stokes H30cm T6s	11	2	Y	Y	2	C	M11	Y	092805_1442	092805_1640
22_1_2	29-Sep	949	22	Stokes H24cm T6s	11	1	Y	Y	2	S	M11	Y	092805_1640	092905_1035
23_2_4	29-Sep	1228	30	cornell_5p8_6p2	10.6	2	Y	Y	3	C	M11	Y	092905_1035	092905_1319
24_3_5	29-Sep	1407	30	cornell_5p8_6p2_bigger	10.6	3	Y	Y	3	C	M11	Y	092905_1319	092905_1509
25_4_6	29-Sep	1558	30	Hs=40cm T=3s	10.5	4	Y	Y	3	C	M12	Y	092905_1509	

Figure 2.5: Summary of wave conditions during the swash zone hydrodynamics experiments.

2.4.1 ADCP Principles of Operation

The ADCP relies on the Doppler shift to determine the velocity of particles suspended in the water. It is assumed that these particles are being advected passively with the water and by measuring their velocity, we are measuring the water velocity. At the most fundamental level, the velocity is computed directly from a Doppler frequency shift measured by comparing the transmitted and received signal frequency content. This process, known as incoherent processing, results in a coarse, noisy velocity measurement which requires averaging to reduce the noise to acceptable levels.

An advancement relative to basic incoherent processing is known as broadband processing. It was developed at Teledyne-RD Instruments of San Diego, CA in the mid 1980's. The major difference between broadband processing and incoherent processing is instead of measuring a Doppler frequency shift, the change in phase induced by a Doppler shift is calculated from the return signal. This results in less noise in the data, but results still require averaging to bring noise levels down to an acceptable level. In Teledyne-RDI's instruments, this is referred to as Mode 1.

A major advancement over broadband processing developed in the late 1980's and early 1990's was pulse coherent processing. In pulse coherent processing, a coded pair of pulses is sent out with known phase, and the Doppler shift induced change in phase is calculated from the return signals. The lag between the two pulses (the known phase) sets both the maximum range and maximum measurable velocity by the ADCP. Longer lags between pulses result in more accurate measurements, but the maximum measurable velocity decreases. Pulse coherent processing results in very low noise measurements, and single ping velocity estimates can provide meaningful data with no averaging. However, the environmental

limits under which pulse coherent operation can be successfully used requires maximum velocities under 1 m/s and no excessive shear in the sampling region. System frequency also plays a role, with the ADCP used in CROSSTEX having a maximum pulse coherent range of approximately 3.5 m, but very good small bin size velocity measurements.

For the series of experiments presented here, Teledyne-RDI's improved pulse coherent mode (Mode 11) was used almost exclusively. This is a combination of broadband processing to determine an appropriate velocity range and pulse coherent processing to unambiguously resolve the velocities from the coded pulses with higher accuracy.

In ADCP terminology, a radial velocity estimate, regardless of the number of acoustic pulses used to obtain it is referred to as a ping. Multiple pings when averaged together form an ensemble. Velocities are measured in depth cells or velocity bins (bins for short) centered some distance x from the instrument. The ADCP reports a range to the center of the first bin, measured perpendicular to the instrument, not along the beam path, from which all other bin locations can be determined. Because the reference level for the bin location is not specified, there is a small amount of error associated with vertical location of each bin. For consistency, the bin location is taken from the center of the transducer.

2.4.2 Deployment & Deployment Consequences

Due to transducer ringing, there is an area directly in front of an ADCP where measurements can not be made. This ringing is compensated for in the ADCP measurements by a variable called the blanking distance. This is simply a distance offset to the first velocity measurement location to allow time for the transducers

to stop ringing before listening for reflected energy. To obtain measurements as close to the bed as possible and minimize scour around the instrument housing, the ADCP was buried in the bed.

Standard velocity constructs for an ADCP use opposing beam pairs (Figure 2.6) to obtain estimates of two components of the velocity, one parallel and one perpendicular to the instrument centerline, from each pair. Because we know the coordinate system for the LWF, we could align the ADCP beams with the coordinate system and obtain direct estimates of U,V and W. However, by rotating the beam pairs 45° with respect to the LWF coordinate system, we can obtain additional information about the flow.

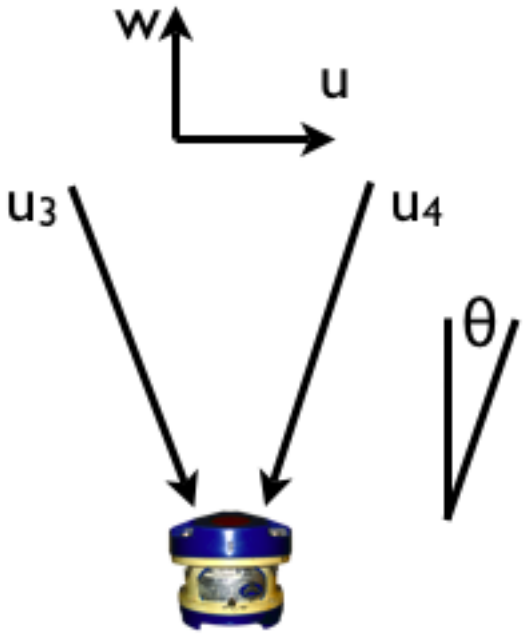

Figure 2.6: ADCP beam configuration, for the instrument used during CROSSTEX, $\theta = 20°$. One pair of beams is in the plane of the page, the second pair is perpendicular to the page.

As seen in Figure 2.7, by using adjacent beams to compose the velocity estimates, we actually obtain estimates of the cross shore velocity, U, spread across the tank. This allows us to verify the flow is 2-D in nature and there are no significant gradients in the along shore direction. An added benefit of the rotation is that we reduce the ratio of beam spread to wave length versus the standard orthogonal orientation.

2.4.3 Velocity Composition

As seen in Figure 2.6, with flow in the plane of a beam pair, each beam sees a weighted sum of the vertical and horizontal velocity components as its beam velocity. By adding or subtracting the beam velocities, estimates of the horizontal or vertical velocity can be obtained. In field applications, a compass and pitch and roll sensor are used to rotate these velocity estimates into an earth coordinate system (East, North and Up) and compensate for instrument heave. In the LWF we know the rotation and have leveled the ADCP so pitch and roll are both constant at zero. Below are the standard formulas used to calculate each velocity component, simplified so that instrument pitch, role and rotation are not considered (Lohrmann et al., 1990) (Stacey et al., 1999).

$$u_3 = U \sin\theta + W \cos\theta \tag{2.1}$$

$$u_4 = -U \sin\theta + W \cos\theta \tag{2.2}$$

$$U = \frac{(u_3 - u_4)}{2 \sin\theta} \tag{2.3}$$

$$W = \frac{(u_3 + u_4)}{2 \sin\theta} \tag{2.4}$$

Similar calculations for the second beam pair (oriented orthogonal to the first)

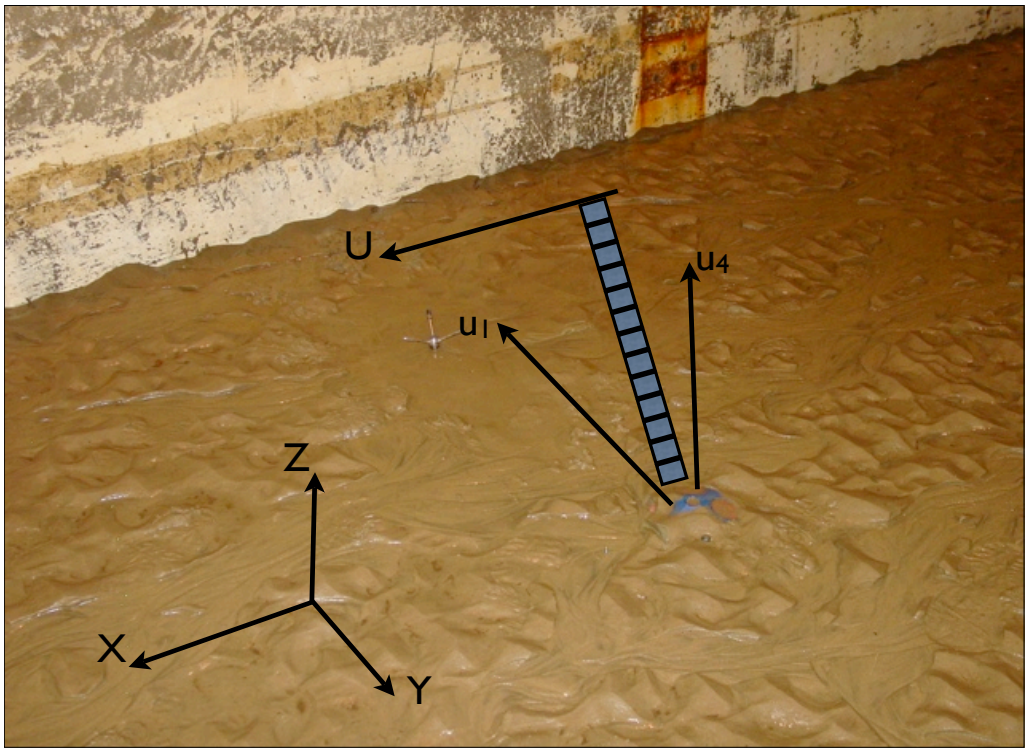

Figure 2.7: Diagram of ADCP beam paths. Beams 1 and 4 are directed ± 45◦ from the negative y-axis and elevated -20◦ from the positive z-axis. Beams 2 and 3, opposite beams 1 and 4 respectively, are the two unlabelled beams. All four beams are rotated 45° to the coordinate system shown in the picture. The blue rectangles represent measurement bins which are spaced along the negative y axis and increase in elevation closer to the wall. A positive onshore velocity is represented by the arrow labeled U. The LWF coordinate system is shown in the lower left.

would yield an estimate of V and a second estimate of W. The difference between the two estimates of W is called the error velocity and is a useful data quality indicator. If it exceeds a certain value, data quality is compromised, either because one or more beam is reporting erroneous velocity information or the flow is no longer homogenous.

Using the above as our basis, we can rewrite the beam velocities for each beam 1-4, for our orientation shown in Figure 2.7, and introducing a rotation angle ϕ, as

$$u_1 = w\cos\theta - u\cos\phi\sin\theta - v\sin\phi\sin\theta \tag{2.5}$$

$$u_2 = w\cos\theta + u\cos\phi\sin\theta + v\sin\phi\sin\theta \tag{2.6}$$

$$u_3 = w\cos\theta - u\cos\phi\sin\theta + v\sin\phi\sin\theta \tag{2.7}$$

$$u_4 = w\cos\theta + u\cos\phi\sin\theta - v\sin\phi\sin\theta \tag{2.8}$$

and combine the above beam velocities to estimate U as

$$U = \frac{u_3 - u_2}{-2\cos\phi\sin\theta} \tag{2.9}$$

$$U = \frac{u_4 - u_1}{2\cos\phi\sin\theta} \tag{2.10}$$

Similar combinations will give us estimates of V. Ultimately, only two velocity components, U and V, can be isolated from combining 2.5 through 2.8. The second component from each beam pair as written is oriented in the plane of the two beams and is a weighted sum of the horizontal and vertical velocities. Without further assumptions we can't estimate W from only two beams as written in 2.5 - 2.8. We instead use the standard opposing beam pairs to estimate W.

While this may seem a convoluted means of obtaining the velocity profile, there are more benefits to operating the ADCP in this manner than drawbacks.

While ADCPs have been around for almost thirty years, it is only in the past several years that they have been used in very shallow environments, laboratories, and highly dynamic environments with much success. As the instruments become slightly cheaper to manufacture (one company already offers custom transducer alignments) and smaller, ADCPs will see more use in laboratories and shallow flows. Because of their profiling ability and the redundant information they provide, allowing post processing to improve their accuracy further, they can provide a non-intrusive replacement for other typical instruments.

2.4.4 Screening ADCP Data

Prior to calculating U, V and W, screening of the beam velocities is done. The ADCP produces two data quality indicators, a correlation measurement and a return signal strength indicator (RSSI), for each beam. A lower limit for correlation is used to screen data. When any single beam measurement falls below it's lower limit, all four beam measurements are discarded. Measurements the ADCP has flagged internally as bad, represented by the value -32768 in the beam velocity records, are also discarded. This is a conservative approach as three beams still provide the ability to measure three components of velocity, but simplifies and standardizes later analysis such as phase averaging. A linear interpolation scheme in time is used to replace the discarded values in each beam. Spatial interpolation (i.e. fitting to the velocity profile and interpolating missing bins at each time step) was employed after the temporal interpolation to replace bins which were consistently bad due to pulse interference.

An iterative Gaussian filter is used after data screening to remove outliers in each beam, again discarding all four beam measurements when any single beam

fails to meet screening criteria. The filter was applied to each bin independently, treating each as a time series. The threshold to discard data was set at 3.5 standard deviations. Linear interpolation in time is used to replace these values. A final step before calculating component velocities is to interpolate the recorded beam velocity time series onto a regular time interval. Teledyne-RDI ADCP's don't force a regular sampling interval between measurements, with variations of several hundredths of a second common. Because of the periodic nature of the flow during CROSSTEX, this causes problems when synchronizing with other measurements, such as the Q45U free surface displacement above the ADCP. Finally, component velocities are calculated and the two estimates for each compoenent are averaged together to produce one estimate each for U, V, and W.

2.4.5 Verifying the 2-D Nature of the Flow

The orientation of the ADCP discussed in section 2.4.2, gives us velocity estimates spread across the width of the tank. By taking the phase averaged difference between the two sides of the tank, we are left with the horizontal equivalent of the error velocity. An example result of this calculation is presented in Figure 2.8. All runs showed behavior similar to this in the offshore region.

From this plot, we can see there is essentially no difference between the two sides of the tank, with the only values significantly larger then zero occurring near the bed and the surface. Minor along shore variations in bathymetry and interference caused by the strong return echo of the surface likely cause these values. We also expect some variation due to each individual transducer's transmit and receive characteristics. We can also infer from this plot the wave height is fairly uniform across the tank and the wave propagates onshore normal to the y axis of the tank,

otherwise we would expect larger differences throughout the water column.

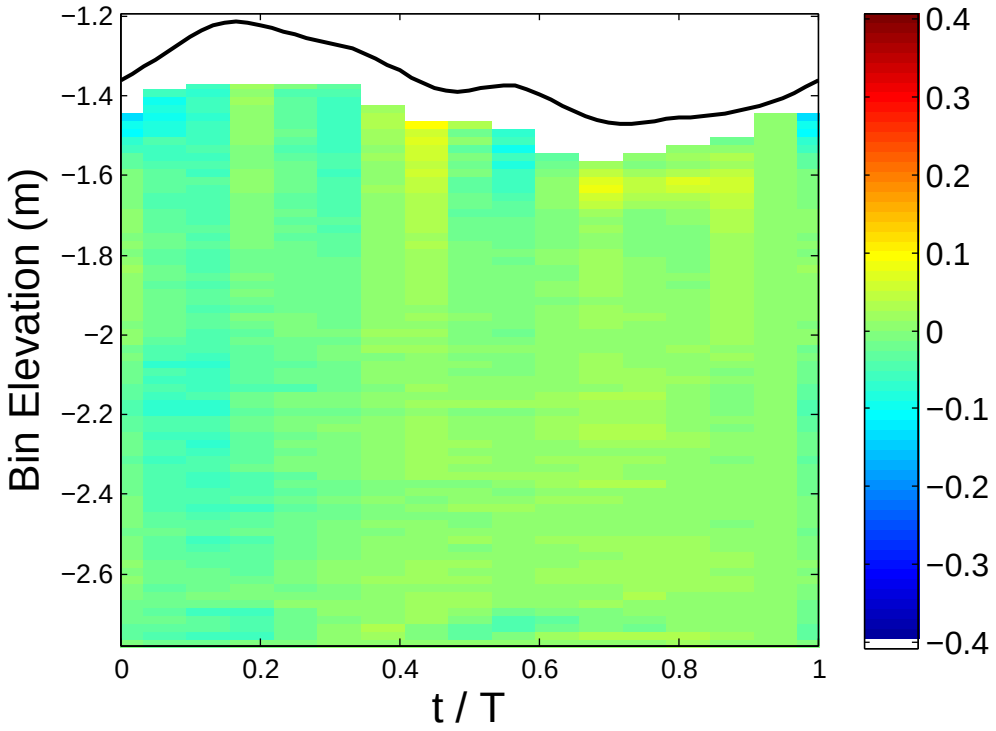

Figure 2.8: Run 6 difference between the two estimates of cross shore horizontal velocity. Note most of the water column has near zero difference, with only areas near the surface and bed showing any marked difference. The phase averaged free surface taken from the Q45U is shown as a solid line.

2.5 ADV Velocity Measurement

Acoustic Doppler Velocimeters rely on the same principles of operation as the ADCP. They operate exclusively in a pulse coherent mode and are bistatic, using different transducers to transmit and receive acoustic pulses. They geometery of the ADV head fixes the center of the sample volume some distance away from the head (Figure 2.9). For the Nortek Vectrinos used in these experiments, this distance is nominally 5 cm. In Figure 2.9 also note 4 receiver arms. Traditionally,

ADVs have used 3 beams, the minimum needed to resolve all 3 components of velocity. The redundant information in the vertical velocity can be used as an additional screening criteria when analyzing data and is analogous to the error velocity discussed for the ADCP. The utility of this operation will need to be investigated further and has not been used when screening velocity information for these experiments. Additionally, because the two horizontal velocity measurements are independent of each other, examining the stress terms that arise from the cross-correlation of these terms is more robust.

The volume of water comprising the sample volume is user selectable on Nortek ADVs. For the Vectrino, it can be set from 3 mm to 9.1 mm (depending on transmit length), for the Vector it can be set between 3.5 mm and 18 mm. By varying the sample volume size (really the length since the diameter is set by the transducer size and focus region), the user has control of the amount of spatial averaging present in the data. This can be important when trying to resolve boundary layers or when working in areas of high shear. Smaller sample volumes generally result in noisier data (Gordon and Cox, 2000), but reduce the averaging present in the data which can be important when examining turbulence. Future work on the effect of each of these parameters on the ADV performance could provide guidelines for minimum sizes of sample volume, transmit length, etc.

Because of their bistatic nature, ADVs are more sensitive to the component of velocity directed into the head, W in the case of Figure 2.9. We can see that for a given velocity $\overrightarrow{v}$, the weighted average velocity the receiver detects is primarily composed of the component directed along the transmit beam. This means the vertical velocity estimate will have a lower level of noise, but also a smaller velocity range over which unambiguous measurements can be made.

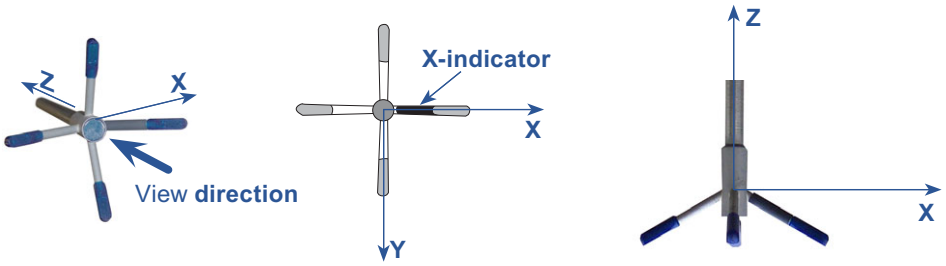

f

(a)

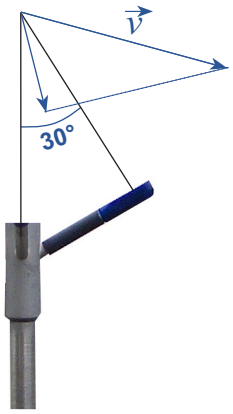

(b) (c)

Figure 2.9: Various views of the Vectrino head, including instrument coordinates. Note in (b) the bistatic axis represented by the short arrow in the interior of the angle. The central transducer in (c) has a diameter of 8.5 mm, and the span of opposing arms is 60.5 mm. Images courtesy of NortekAS.

Table 2.3: Summary of ADV setup at each location during the CROSSTEX experiments.

Instrument	Location (m)	Sample Rate (Hz)	Velocity Range (m/s)	SV Size (mm)	Transmit Power
Vector	$x = 51$	64	0.3	11.8	High
Cart ADVs	$x = 72.82$	50	0.3	7	High-
Frame ADVs	$x = 77.36, 77.66, 79.16$	192 or 200	1 or 0.3	7	High-

With the smaller dimensions associated with the transmit and receive paths, ADVs can sample at significantly higher rates then an ADCP, with data rates as much as 50-75 times faster. A single velocity estimate produced by the ADV is actually an internal average of many individual estimates, averaged down to the user selected sample frequency. Internal sample rates range from 200 Hz to 5000 Hz for the Vectrino. While the Vectrino is capable of producing data at 200 Hz, these experiments show there is little utility in doing this as the instrument's noise floor overwhelms the signal past 50 Hz (Figure 2.10). Note also the lower noise level in the two vertical velocity estimates.

2.5.1 Screening the ADV Velocity

ADV velocity measurements require screening prior to any meaningful conclusions being drawn from them. This is due to the correlation methods used to calculate velocities, the inherent noise in the system, and the conditions under which they are used. Velocity spikes, a consequence of the ADV head geometry and the acoustic technique used to measure velocities, are also a problem. Several methods, such as acceleration filters and a phase-space thresh hold technique have been developed to deal with these spikes.

For measurements located in the inner surf, aeration (bubble entrainment by breaking waves) can significantly impact the return signal and velocity estimates produced by the ADV. Sediment suspension near the bed can also bias water velocity estimates, as the sediment will not necessarily be a passive scatterer and moving at the water velocity. Careful attention must be paid to the criteria used to screen ADV data. Significantly, tests conducted in a tow tank by Snyder and Castro (1999) showed errors in velocity measurements when the ADV head was

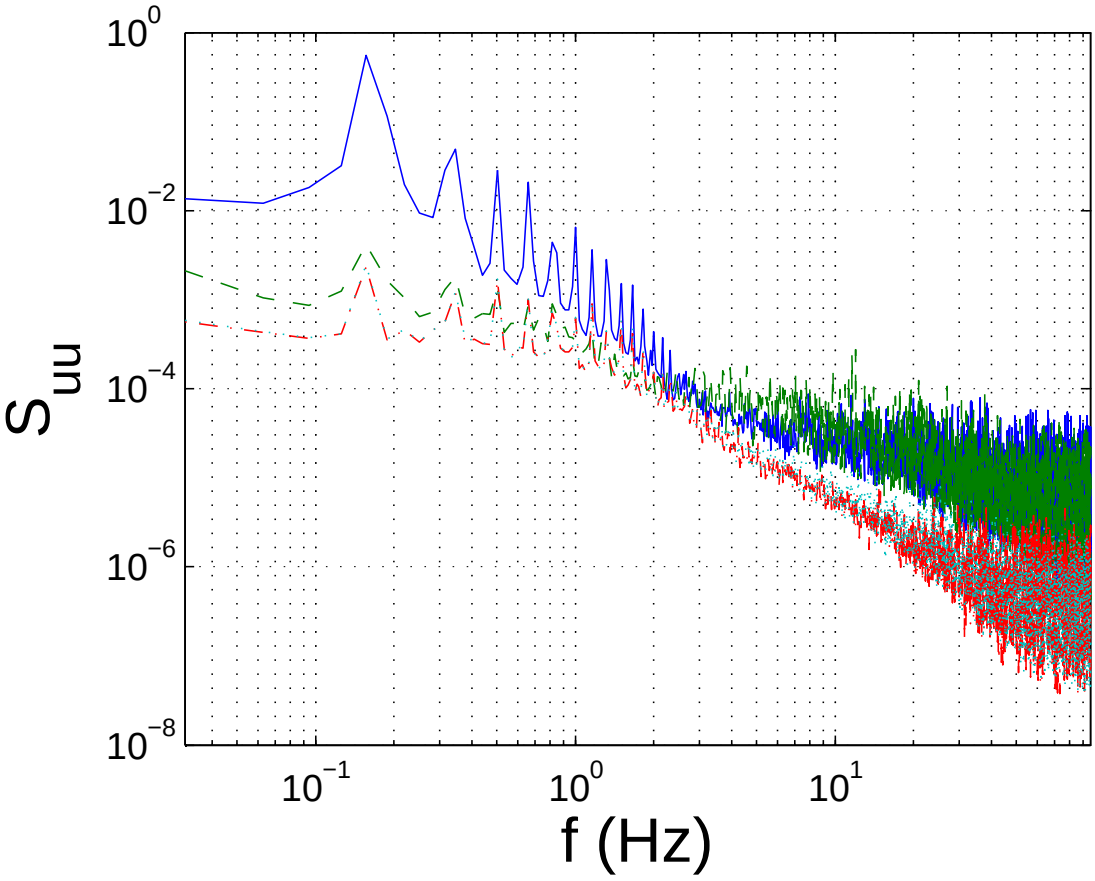

Figure 2.10: Example spectra computed with 32 non-overlapping windows from the offshore high Nortek Vectrino. Data is from Run 6, with T = 6 seconds, and emphH = 20 cm. Note the increased noise past 30 Hz. Sample rate was 192 Hz.

mounted at an angle to the flow (pitch or yaw). Snyder also demonstrated there were errors associated with lower correlation and SNR values meaning appropriate screening is important to obtain unbiased and accurate velocity estimates.

However, the ADVs used in this study, Nortek Vectrinos, are very new instruments and extensive characterization studies have not been conducted to determine appropriate thresholds for SNR and correlation screening. The head is a streamlined design which showed significant improvement in Snyder's tests when angled to the flow. Future comparison studies between older head designs and the newer streamlined head should shed light on appropriate cutoffs for SNR and correlation. For the time being, the Vectrino has performed very well using existing knowledge on ADV performance.

A raw velocity record from an ADV and it's associated data quality indicators are presented in Figure 2.11. Note the spikes in the data, areas of relatively high acceleration and their correspondence to low correlation values. Signal to Noise Rate (SNR) and return signal amplitude also have low values around these spikes. At the start of a run, the signal amplitude and signal to noise ratio are both very low until the first waves come through and scatterers are re-suspended in the water column. After this point, data quality indicators improve significantly, but there are still occasional dropouts needing removal.

Lower limits for SNR, correlation, and signal amplitude are established and points below these thresholds are discarded. As mentioned previously, setting values for the lower limits has no hard and fast rules. Experience with the instrument in known flow conditions can be helpful for learning its operating characteristics and defining these limits. Careful inspection of the raw data also proves useful, with appropriate limits able to be set from visual inspection of plots. We expect

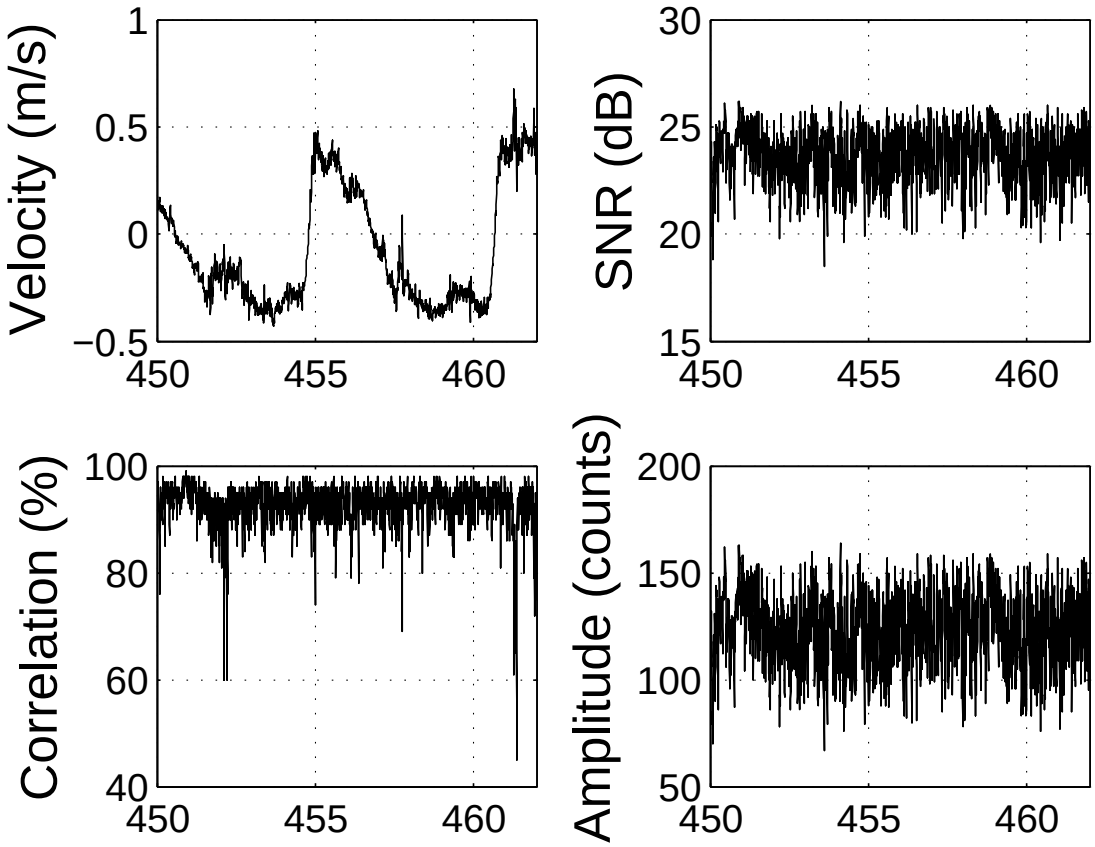

Figure 2.11: Approximately twelve seconds of unprocessed ADV data. Note the velocity spikes around t=457 and t=461.

the ADV to produce generally good results with fairly constant values for a good setup. Wild fluctuations, mid to low range values and unbelievable velocities indicate poor data and instrument setup needing refinement. For CROSSTEX, lower limits varied depending on where in the surf zone and water column the sensor was located. This is due to a desire not to discard a large amount of data for good data runs and again, the new nature of the instrument and it's operating characteristics.

For the offshore frame ADVs, flow depth is deeper and turbulence is not expected to be as strong at the bed (Ting and Kirby, 1994). In this region we can use higher values for all three data quality indicators to increase the quality of our measurements without sacrificing the amount of data significantly. As we move further onshore, the flow depth decreases, turbulence increases, and the water column is more aerated. Associated with the turbulent bore moving past the ADV there is a corresponding drop in signal amplitude, either due to bubbles, transducer wake or flow separation, or the transducers coming out of the water. Lower (less strict) thresholds are used here to increase the amount of data retained at the expense of data quality. In all instances, the same limits were applied to a given record throughout the run.

Once screened for data quality, an iterative, adaptive gaussian filter was used to remove outliers from the record. The number of standard deviations used to define an outlier is selectable, but was generally set at 3.5. On each pass through the gaussian filter, a new standard deviation was calculated after the previous outliers had been discarded. The number of passes varied, with stopping criteria defined as the point at which one or fewer outliers were encountered.

The Gaussian filter worked well to remove obvious spikes which had very high

velocities. Implementing an acceleration filter or the phase space threshold is slightly more difficult with a periodic flow and phase dependent mean and was not carried out in the present analysis. The reader is referred to Goring and Nikora (2002) for a discussion of various acceleration filter methods and an initial implementation of the phase space threshhold technique. Wahl (2003) provides an alternative method of implementing the phase space threshhold which is also available in the free software package WinADV available at http://www.usbr.gov/pmts/hydraulics_lab/twahl/winadv/.

The phase space threshhold shows promise for removing spikes from velocity records. The primary reason it was not implemented at present is time. To successfully use the method, the phase mean needs to be calculated and removed from the record. As discussed in §4.1 and §4.1.1, the phase average in the surf zone is not the best means to remove the mean from a velocity record owing to the variation in the arrival of the bore front and the associated smearing of the phase average. The linear filter introduced in §4.1.1 is likely the best means to remove the mean, but owing to it's larger processing requirements versus the phase average, subsections of the record will need to be processed individually. An exploration of how the predicted signal varies with each section owing to changes in the filter will also need to be included.

The final step in cleaning the frame ADV velocity records was to downsample via ensemble averaging each component to 50 Hz from 192 Hz or 200 Hz depending on the run. This made the time series more manageable for further analysis, reducing the number of points in the time series by a factor of five. Little information is lost because of this averaging since the noise floor of the instrument begins to dominate above 50 Hz (Figure 2.10) and the averaging significantly decreases the

per ensemble uncertainty.

2.5.2 Synchronization and Data Gaps

Due to software and communication problems, the three frame ADVs have numerous data gaps which must be accounted for in the time series analysis conducted here. These gaps are caused by a lack of buffering in the hardware and software controlling data acquisition for the Nortek Vectrinos. Running multiple instruments on the same computer hardware is best accomplished via the use of Nortek's Polysync software, although testing should occur under high CPU loads to ensure all data is being recorded. Running a single instrument off of one computer will also avoid these data gaps but requires more hardware.

Two different counters are used when recording data from the Vectrino. The first counter is the raw data counter which counts from 0 to 255. The second counter is a 24-bit counter (1-16777216) generated during data conversion by introducing a simple loop counter to count the number of times the raw counter has cycled. This counter will be thrown off by gaps longer then the raw data counter cycle time, which is in turn dependent on the sample rate.

The data gaps can be differentiated into two different types. The first type of gap occurs when the missing data does not span an entire raw counter cycle (0-255 samples, time length depends on sample rate). These gaps are easily accounted for by using the Vectrino ensemble counter (the second counter mentioned above) to calculate the time. The second type of gap lasts longer then the raw counter reset time (1.28 seconds at 200 Hz) and is not accounted for by using the ensemble counter to calculate the time since an entire cycle is missed. This type of gap must be corrected for via some other method.

Because of the periodic nature of the velocity, it should be fairly simple to realign the data when long gaps occur. Comparison to a signal with no gaps should allow the length of the longer gaps to be accurately determined and compensated for in the time series. Given an assumption of coherence between the two velocity records and that a long gap does not last longer then one wave period, introducing a time offset at the appropriate point in the record will correct the time string. If multiple long gaps are present, simply stepping through the record from the beginning will allow each subsequent gap to be corrected.

Long data gaps only occur on one of the frame ADVs, the offshore high location. Comparison with the offshore low ADV, 30cm further onshore and lower in the water column, allows the length of the data gaps to be determined and compensated for by using zero upcrossings of the cross shore velocity. This correction was done on lowpass filtered signals with no phase distortion by running the filter forwards and backwards (see MATLAB command *filtfilt*). This removes spikes and smoothes the record for easier zero upcrossing identification. The correctly time stamped signals are then screened in the manner described in §2.5.1.

2.6 Uncertainty Analysis

Kline and McClintock (1953) defined uncertainty as "A possible value the error might have" Any measurement we make is subject to uncertainty, and understanding and placing bounds on the uncertainty associated with a measurement is important in both analyzing and interpreting it. Kline and McClintock suggest the confidence interval approach as an appropriate manner to present the uncertainty in a measurement. Where appropriate, 95% confidence intervals are presented along with the sample statistic (e.g. the mean).

Uncertainty contains two types of error, a systematic bias in the measurement due for instance to an error in calibration, and a random component which affects the spread of the data. Bias estimates come from manufacturer specifications or simple physical arguments (such as when determining absolute position). Bias is considered significant only when comparing data between multiple instruments, being in most cases specific to a particular instrument or technique.

Random error, where appropriate is estimated using the bootstrap technique (Efron and Tibshirani (1994)). Using MATLAB's built in bootstrap function, 1000 replicates of the statistic of interest (usually the mean, although we also consider variance) were calculated and sorted, with the 25th and 975th sorted values taken as the lower and upper bounds of a 95% confidence interval around the statistic.

2.6.1 Bathymetry

The survey staff used in hand surveys provided measurements to 0.01 ft. The uncertainty (bias plus random error) associated with each elevation measurement is O(1 cm) caused by the staff sinking into the sand a variable amount and variations in the cart deck against which measurements were read. Separating random error and bias in these measurements is difficult since only a single measurement was taken at each grid point. Additionally, any bias in the actual reading of the survey staff marking will be consistent among all surveys since the same personnel conducted the survey each time. Error in positioning the cart at each grid point is O(1 cm).

For the MTA, accuracy is given as $\pm$ 1mm by the manufacturer, but real world accuracy will be worse since the MTA was operating in a noisy acoustic environment, and the multiple transducers potentially interfered with one another.

While surveys were conducted during still water conditions, it is likely the acoustic pulse sent out by a transducer penetrated the bed a short distance, biasing range measurements long. It is difficult to separate the bias and random error for the MTA for the same reasons as the hand survey, namely only single measurements were taken at any location. However, the bias in any measurement should be small compared to the random error associated with the instrument. For these reasons, the accuracy of the MTA measurements is placed O(5 mm), which is well within the needs of the present analysis.

2.6.2 Freesurface

The resistance wave gages have a potential calibration bias associated with them. Using the calibration data provided by Oregon State University, the correlation coefficient for the linear calibration is always above 99.9%. This means their response is both highly linear and the error associated with the calibration is minimal, O(1 mm) at the full scale value of the wave gage (5 V) assuming an error on the order of 0.1% and utilizing the calibrated conversion from volts to length units.

Manufacturer stated accuracy of the Q45U is $\pm$ 0.1 % of the measured distance or a minimum of $\pm$ 0.25 mm. For the setup used in CROSSTEX, this amounts to a potential error in the range to the free surface, and thus the free surface elevation, of O(1 mm). Analysis of overnight still tank measurements support the accuracy of the Q45U, with the 95% confidence interval on the mean equal to $\pm 0.6 \times 10^{-3}$ cm.

2.6.3 ADCP

The ADCP velocity estimates have an error associated with them depending on the measurement technique used (broadband or pulse coherent). Manufacturer specifications for a 1200 kHz ADCP place the accuracy of velocity measurements at $\pm$ 0.3% of the water velocity or $\pm$ 0.3 cm/s. Actual measurement error is much higher, but is hard to quantify due to the complex nature and large number of variables governing ADCP operation.

Teledyne-RDI's planning software PlanADCP provides estimates of velocity standard deviation as an estimate of random error. Given the setup (bin size, mode, water temperature) of the ADCP based on equations governing the theoretical response of the instrument, a single ping standard deviation is produced. For Mode 11 this standard deviation is O(1.5 cm/s), weakly increasing with bin size. For broadband modes (used during the last data run) this standard deviation can be O(10-30 cm/s) depending on averaging and bin size. The lower limit is O(10 cm/s) regardless of how much averaging is done for broadband processing, governed by the noise associated with the method used to calculate the Doppler shift.

Near the surface and bed, velocity bins can show significant bias towards zero due to the strong return echo associated with these areas. Teledyne-RDI provides a formula for estimating the portion near a boundary which might be contaminated (Gordon (1996)). For the ADCP used during CROSSTEX this portion is the final 10 cm of the profile (5 bins in most cases). The blanking distance generally accounts for bias in the lower bins, removing the area which would show bias from consideration. However, during CROSSTEX, the ADCP was operated with the blanking distance set to zero. The contaminated bins have not been removed from the displayed records because the appropriate analysis of boundary layer

thickness was not carried out. The bottom 2 bins should thus be regarded with some skepticism in terms of accuracy.

2.6.4 ADV

ADVs have higher accuracy then ADCPs, with manufacturer specifications placing measurement error at $\pm$ 0.5% of the measured velocity or a minimum of $\pm$ 1 mm/s. For typical velocities encountered in the LWF during CROSSTEX, the associated error is $\pm$ 2.5 mm/s. Confidence intervals are provided when discussing mean quantities in later sections. In general, real world accuracy will be lower then this, with quoted values O(1-5%) in literature (Blankaert and Lemmin, 2006).

2.6.5 Spatial Locations

Instrument x locations were surveyed from a reference point, usually a bay bolt hole location nearby using tape measures. Each instrument x location is within 1 cm of it's true location. In order to conduct surveys, the cart and frame ADVs were moved between each run and repositioned using alignment marks. This does not significantly impact the x location of these instruments.

Resistance wave gage locations were surveyed with the laser positioning system on the cart and a plumb line within 1 mm (accuracy of the laser positioning system) of their true location.

Vertical positioning of the ADVs was accomplished using the probe check function provided in the operating software. This presents a display of return signal strength vs. distance, making it easy to identify boundaries by their strong return echo. This allows positioning of the instruments within 1 mm of the desired location.

For the cart ADVs, the vertical distance between probes was calculated using the same probe check function and a level, hard surface placed in the water to provide a strong echo. Distance from each probe was measured, with the difference from the lowest sensor used to determine instrument spacing (Figure 2.4). The two side looking probes were surveyed from an adjacent vertical probe location and suffer slightly less accurate positioning, O(5 mm).

2.6.6 Wave Characteristics

Wave frequency was set in the wave paddle control software by specifying a period. Calculation of spectra from various instruments and the wave paddle driving voltage signal confirm the period produced was the same as set in the control software within $\delta f = 0.001$ Hz.

The deep water wave height was also set in the control software. A wave gage located on the face of the paddle provides feedback to the control software to accurately reproduce the desired wave height. Using this record, the desired wave height is produced with $\pm$ 1 cm accuracy within the first few waves being generated. Wave reflection begins to affect the signal past the first several waves, although a quasi-steady state exists eventually. An example of a wave height time series calculated from zero crossings is presented in Figure 2.12. This data is from Run 21, the largest wave height considered during the swash zone experiments. There is an obvious upwards trend in the wave heights, indicating in increasing amount of reflected energy in the tank.

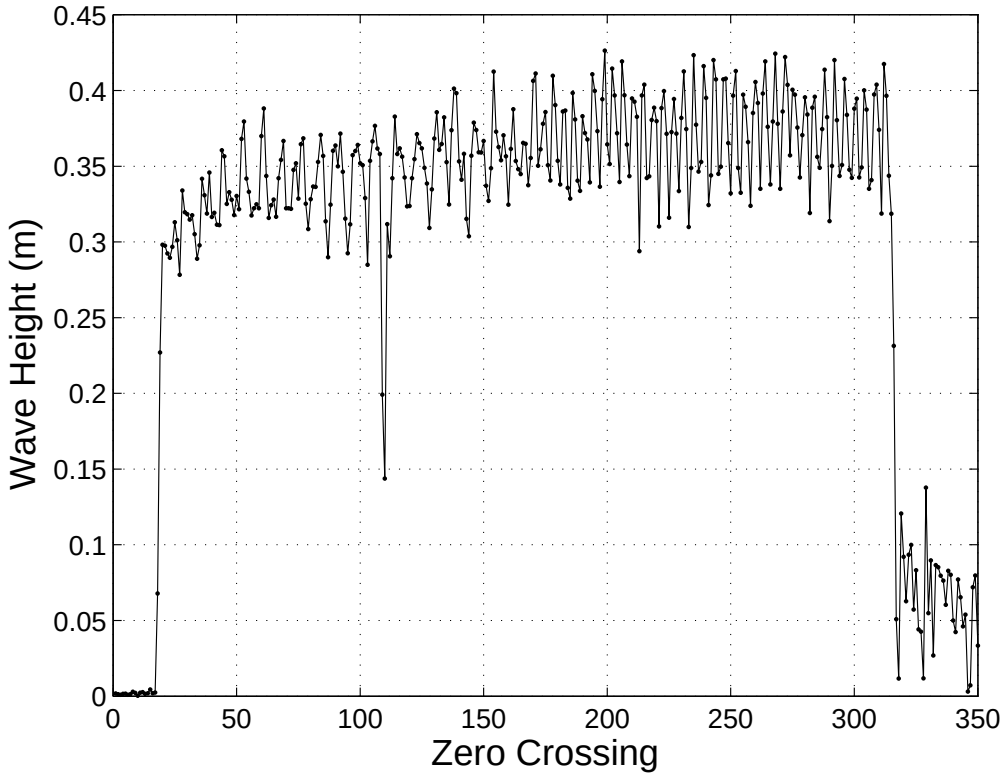

Figure 2.12: Run 21 wave heights calculated by finding the minimum and maximum values around a zero crossing. The desired wave height was 30 cm.

Chapter 3

Wave Characteristics

Our interest in the wave characteristics is to determine at what point the wave and flow fields become stable and how repeatable the wave is once stability has been achieved. To determine stability, short term (1 & 2 wave period) moving averages are calculated, and stability is indicated by a lack of high amplitude oscillations in the average. Wave repeatability is addressed via phase averaged results and root mean square (RMS) deviation from the phase average. A repeatable wave will have narrow confidence intervals (here computed from the bootstrap technique) on the phase average and a low RMS deviation at all points in the phase. For the basic stability and repeatability analysis performed here, either of these conditions is sufficient to call a wave repeatable. The reflection coefficient for each run is calculated using three separate methods which will be discussed in a later section.

3.1 Definitions

Given a sequence of data X, define the length n moving average $< X >^{MA}$ as

$$< X >^{MA} = \frac{1}{n} \sum_{j=i-(n-1)/2}^{i+(n-1)/2} X_j \tag{3.1}$$

That is the ith point in the n=5 point moving average will be calculated as

$$< X >_i^{MA} = \frac{1}{5}(X_{i-2} + X_{i-1} + X_i + X_{i+1} + X_{i+2})$$

The moving average is a Finite Impulse Response filter equivalent to lowpass filtering data. While it can introduce a delay in the signal, it does not distort the

phase. Equation 3.1 is a centered moving average however, and does not introduce a delay because it looks both forward and backward. If it was modified to only examine points before or after, there would a slight delay associated with the average.

The phase average of a periodic signal is simply the average of points separated in time by the dominant period of the signal. Given a signal Y with period T, we can write the phase average as

$$< Y >^{PA} = \frac{1}{N} \sum_{t=t_0}^{t_0+NT} Y(t) \tag{3.4}$$

In practice this is difficult to do because of sample aliasing caused by wave-to-wave variability, uneven time sampling by some instruments, and slow sample rates on some instruments. We modify the above definition to look at a phase bin, an interval around the desired time t, which includes a number of points which are averaged together prior to computing the phase average from Eq. 3.5. This process is equivalent to applying an ensemble average prior to the phase averaged result being calculated. The new formula for calculating the phase average is

$$< Y >^{PA} = \frac{1}{N} \sum_{t=t_0}^{t_0+NT} \frac{1}{M} \sum Y(t - \alpha * 1/fs < t < t + \alpha * 1/fs) \tag{3.5}$$

Where α is a factor used to expand the phase bin larger then the sampling interval, fs is the sample rate and M is the number of points found in the phase bin.

The RMS deviation from the phase average is defined simply as

$$X'_{RMS} = \sqrt{\overline{(X(t) - < X(t/T) >^{PA})^2}}$$

where the bar denotes an arithmetic mean.

3.2 Wave Reflection

Wave tanks do not generally have open boundaries so energy not dissipated by wave breaking, turbulence, or other means remains in the tank. This can severely interfere with measurements as undesirable standing waves can be formed, wave repeatability (and thus phase averaging) is affected, and conditions otherwise unlikely to be encountered in natural systems develop. There are many means used to minimize reflected energy (absorptive material on the beach, active wave height control), but eliminating reflection completely is impossible without an open boundary to allow the energy to leave the system. The ratio of reflected to incident energy is called the reflection coefficient.

There are numerous methods for separating incident and reflected waves and they all perform well in various situations. No single method has gained wide spread acceptance as the definitive means to separate incident and reflected wave energies, but two methods, one popularized by Goda and Suzuki (1976) (GS) and the other by Mansard and Funke (1980) (MF) are widely used in wave tanks. Implementations of these two methods as well as a third method originally developed by Frigaard and Brorsen (1995) and modified by Baldock and Simmonds (1999) (BS) to include linear shoaling are used to calculate the reflection coefficient for each run.

The basic theory behind the estimation of wave reflection is the linear superposition of wave trains at some spatial location, which can be separated by various means (usually a spectral approach) to resolve incident and reflected waves. The method outlined by Goda and Suzuki (1976) is based on measuring the surface elevation at two loctions, and a linear deconstruction of the expected signal at each location. By using spectral methods, the coefficients for the various components

of the wave train (a summation of sin and cos) at the fundamental and higher frequencies are estimated, which are then used to solve for the incident and reflected wave energy as a function of frequency.

The Mansard and Funke (1980) method relies on three gages spaced at preferred intervals based on the wavelengths trying to be resolved. The same underlying assumption of linear superposition of the wave field is employed. Instead of solving directly for the reflected and incident spectra from amplitudes computed from the frequency spectra, a linear least squares fit is employed. The basic method relies on several different spectra and transformations between them, including the cross spectra between gages. Phase differences are used to separate incident and reflected waves, and finally a least squares fit using the calculated phases and frequencies is used to obtain the incident and reflected amplitudes. Owing to its greater complexity and reliance on several different spectra, it is expected the MF method will be the most sensitive to problems with wave gage spacing and the manner in which the spectra are computed. Wave gage spacing was not optimized for the Mansard and Funke (1980) method prior to data collection.

The final method used to examine wave reflection, Baldock and Simmonds (1999), uses a method developed by Frigaard and Brorsen (1995) using two gages. The incident and reflected wave amplitudes are obtained by transforming the recorded signals to the spectral domain, applying theoretical phase shifts to the recorded signals, and then transforming back to the time domain. The incident and reflected waves are then recovered and the reflection coefficient can be calculated. Baldock and Simmonds (1999) applies a linear shoaling model to account for changing bathymetry.

As all three methods rely on spectral or Fourier analysis to resolve the inci-

dent and reflected wave spectra, they are sensitive to choice of Fourier transform length, data windowing, aliasing and side lobe leakage. Attempts to implement GS in MATLAB proved difficult because of these issues, and rather then search for a spectral method which provided reasonable results, existing, working implementations were obtained for use here. Implementations were graciously provided by the following persons to assist in calculating reflection coefficients. The GS and MF implementations were provided by Francisco L. Martin, Grupo de Ingenierìa Oceanogràfica y de Costas (G.I.O.C.) (Ocean & Coastal Research Group), Universidad de Cantabria, Cantabria, Spain. The BS implementation was provided by Dr Tom E. Baldock, Dept. of Civil Engineering, University of Queensland, Brisbane, Australia.

A simple test time series for evaluating each method was generated by superimposing an incident and reflected wave at different locations to generate the data needed for each method. The first two locations were used in all three methods, with the third location used only in MF. The time series at a gage is given by the following equations

$$\eta_i = (\eta_I + \eta_R)_{x=x_i} = A_i \cos \sigma t + B_i \sin \sigma t \tag{3.8}$$

$$A_i = a_I \cos(kx_i + \varepsilon_I) + a_R \cos(kx_i + \varepsilon_R) \tag{3.9}$$

$$B_i = a_I \sin(kx_i + \varepsilon_I) - a_R \sin(kx_i + \varepsilon_R) \tag{3.10}$$

At each location, the wave gage sees a superposition of the incident and reflected waves, offset in phase by the values ε_I and ε_R. By specifying the incident and reflected amplitudes and phases, it is possible to construct a time series at each location. These time series are then used in each method to calculate the reflection

coefficient which is compared to the value known from the incident and reflected amplitudes specified.

As can be seen in table 3.1, no method obtains the reflection coefficient exactly, with values generally low by 1-1.5%. Surprisingly, MF estimates the lowest reflection coefficient. While not an exhaustive comparison, it does indicate none of the three methods will provide an exact value of the amount of reflected energy. The value of the reflection coefficient calculated is thus only approximate and serves as a diagnostic measure of the experiments and nothing more.

Table 3.1: Reflection coefficient for test case calculated with each method. The exact value (first row) is calculated from the ratio of reflected and incident amplitudes specified when generating the time series.

Method	K_r
Exact	0.1
GS	0.084
BS	0.088
MF	0.077

For each run, K_R was calculated with all three methods. Results are summarized in table 3.2. The disparity between the two gage methods and the three gage method is due to the third gage being located in a region of non-linear shoaling. Given the good agreement between the two gage methods, their general agreement with the test time series, and visual observations, a global reflection coefficient, K_R for the tank can be estimated as $\approx 10-12\%$. This is inline with what other exper-

iments have reported and does not seriously affect the analysis and interpretation of data.

Table 3.2: Reflection coefficient with each of the methods (GS, BS, MF). Note the high values in the MF column, likely to due to non-linear shoaling

	K_R		
Run	GS	BS	MF
6	0.116	0.102	0.2415
16	0.104	0.096	0.1854
21	0.096	0.079	0.19

3.3 Tank Seiching

Tank seiching, a long, low amplitude standing wave pattern excited by the incident waves and wave reflection can affect the analysis and interpretation of data. Several long overnight records were taken with the Q45U during the three week experiment period and several shorter records were recorded after some runs while the tank was settling to examine how long the seiche modes remained active in the tank. Models exist to predict the period of various seiche modes over different bathymetries, but the irregular bathymetry of the tank makes an exact value time consuming to calculate. Instead, spectral analysis was employed to look at frequency content of the seiche records in addition to their amplitudes, and comparisons to simple bathymetries have been made.

In Figure 3.1, data from one long overnight record and two post-run records is

presented on a log scale. The first two seiche modes, predicted for a rectangular basin 85 m long are marked by vertical lines on the graph, as well as the driving frequency for the wave runs (0.167 Hz). In all cases the first two modes occur, with the third run, corresponding to the largest incident wave height, showing the most energy at the Mode 1 seiche. Two peaks not accounted for by low modal number seiching that occur in all three records are a small peak around 0.0025 Hz (a period of ≈7 minutes) and a similar peak at 0.255 Hz (a period of ≈4 seconds). One possibility for the higher frequency component is a seiche aligned with the tank width instead of its length, although this seems a bit unlikely given the tank geometry. The period of this higher frequency peak does coincide with a very high modal number (≈9) seiche in the lengthwise direction. This is a very high modal number however and it seems unlikely such a high mode would be selected to receive so much energy. Since this higher frequency component seems to increase in energy with wave height, it could be tied to the paddle motion and drive system. The low frequency component is harder to explain, but could be a subharmonic of the mode 1 seiche that because of the bathmetry remains active longer then surrounding harmonics. An alternative explanation might be a surface motion introduced by the pore water entering and exiting the beach under changing hydrostatic conditions.

Figure 3.2 shows the spectral energy represented as amplitudes in centimeters. The third run excites the largest mode 1 seiche as expected and transmits more energy to other seiche modes (the small bumps on the amplitude plot) which is not unexpected. This ringing effect occurs in the other two records with less energy overall.

How long this seiche energy remains in the tank is also of interest. While it is

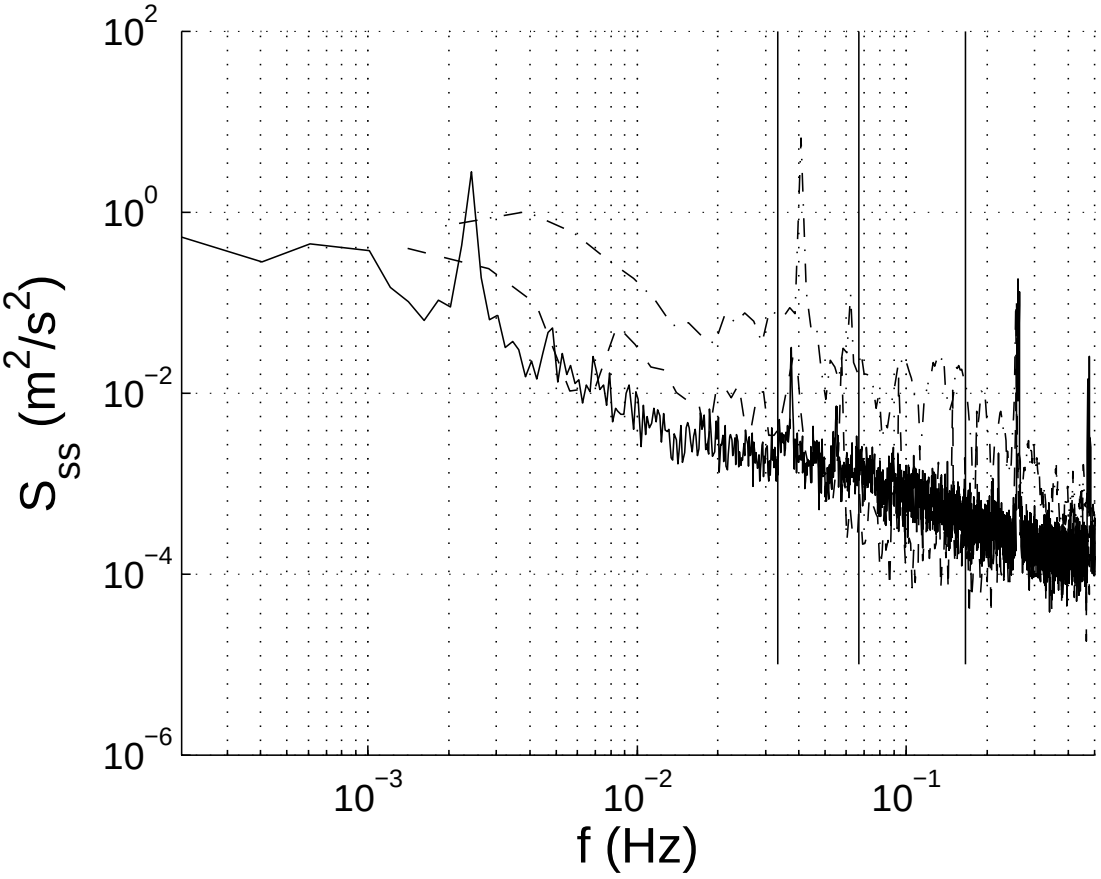

Figure 3.1: Power spectral density of seiche data from the three runs considered in this analysis. Run 6 (overnight record) −,Run 16 −−, Run 21 −·−. From left to right, the three vertical lines represent the Mode 1 and 2 seiche frequencies in a rectangular basin and the driving frequency (T = 6 sec) for the waves generated for each run.

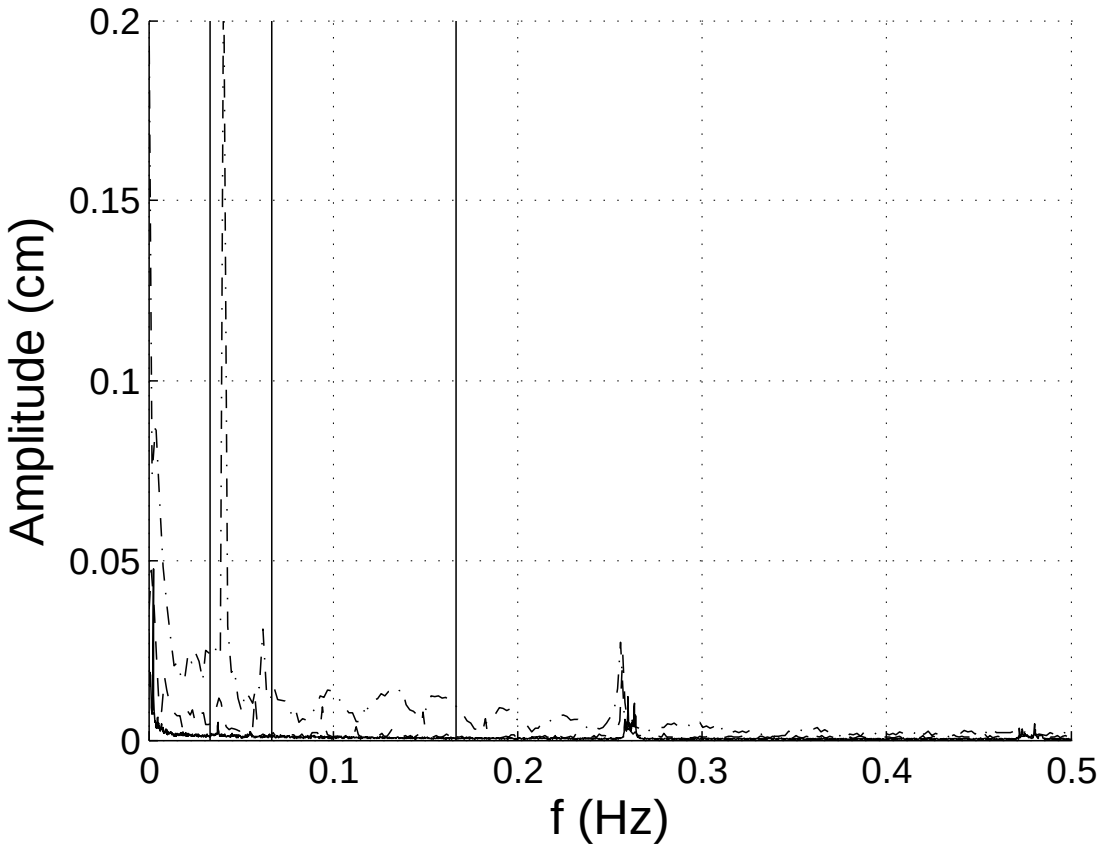

Figure 3.2: Power spectral density of seiche data from the three runs considered in this analysis. Run 6 (overnight record) $-$,Run 16 $--$, Run21 $-\cdot-$. From left to right, the three vertical lines represent the Mode 1 and 2 seiche frequencies in a rectangular basin and the driving frequency (T = 6 sec) for the waves generated for each run.

two and half decades lower in terms of energy, the mode 1 seiche is still apparent in the overnight record (approximately 11 hours of data), as is the higher frequency signal. The lack of decay in the energy of the mode 1 seiche is shown Figure 3.3. While unfortunate, it is not surprising the seiche energy remains this long. There is little damping and dissipation associated with the seiche since it never enters a non-linear regime where turbulence is generated. The time scale for this energy to die out is on the order of days not hours. While it does contribute to the irregularity of the flow and swash zone size, it is probably much less important than the effect localized bathymetry plays in those same areas.

3.4 Wave Length, Incident Wave Height, and Surf Similarity Parameters

For the runs presently considered, various descriptive parameters for each run are provided in table 3.3. These parameters are used to describe the breaking condition of the wave (important for analyzing and interpreting the turbulence later) and for various scaling used throughout when interpreting data between runs. Offshore data is taken at the Q45U location, while surf zone data is taken at the location of wave gage 8 (x = 64.98 m). The wavelengths presented in Table 3.3 do not account for changing water depth, and are calculated as instantaneous values at the two locations using the mean water depth.

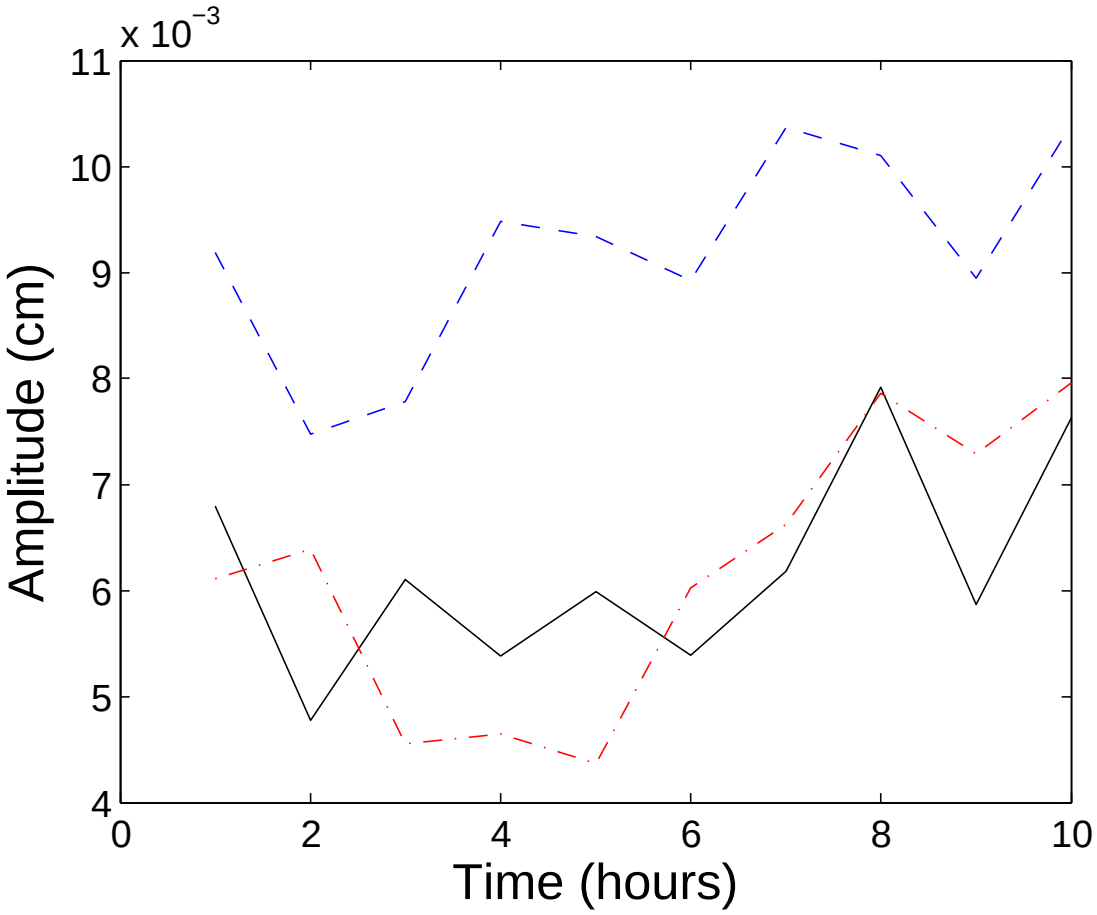

Figure 3.3: Seiche amplitude of the mode 1 seiche and the neighboring frequency bands from the run 6 overnight record. There is essentially no decay in the seiche amplitude overnight.

Table 3.3: Offshore and Surf Zone wave height (H), wave number (k), and wave length (λ) calculated at the offshore boundary station, run Iribarren number (ξ) and breaking wave height to water depth ratio (γ).

	Offshore			Surf				
Run	H m	k	λ m	H m	k	λ m	ξ	γ_B
6	0.193	0.282	22.3	0.324	0.505	12.36	0.678	0.74
16	0.145	0.283	22.2	0.201	0.489	12.85	0.437	0.72
21	0.355	0.27	23.3	0.525	0.423	14.85	0.653	0.92

3.5 Wave Climate Stability

3.5.1 Offshore

Instruments located outside of the breaker line include the ADCP, Nortek Vector ADV, the Q45U and wave gages 1-7. Using equation 3.1, moving averages of 1, 2 and 25 periods were calculated for each wave gage, the Q45U, and the ADCP for each run. Figures 3.4 through 3.6 show the results for select wave gages over each moving average interval. Free surface signals generally show a longer stability time then velocity signals (ADCP results not shown). For the three runs considered here, stability times, defined as a lack of high amplitude oscillations in the longterm moving average, varied from approximately 200 seconds to 600 seconds. In some instances there was no significant decrease in the high amplitude oscillations. In those cases, the stability time was taken as long as possible to allow a significant number of waves (greater then 100) for phase averaging.

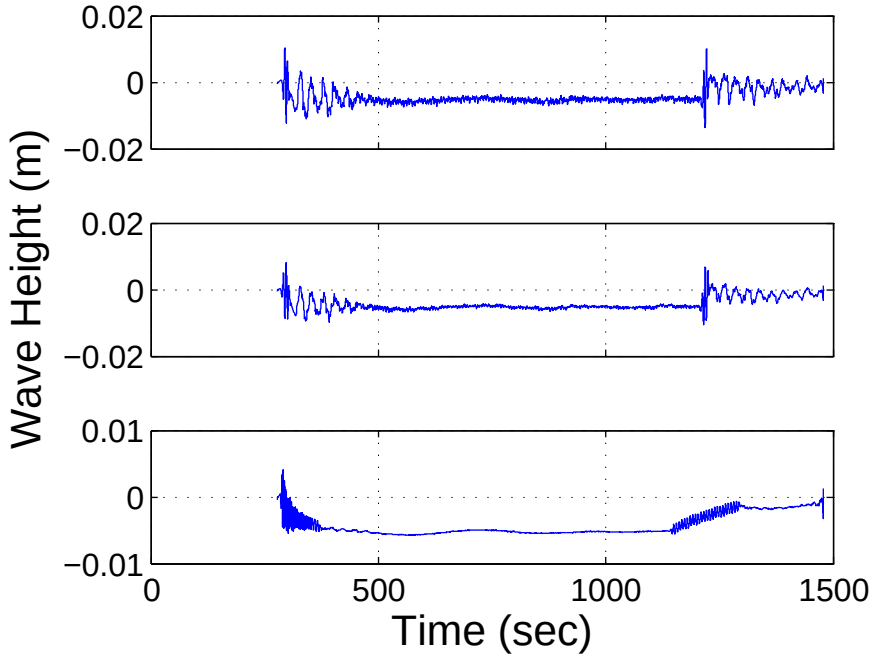

(a)

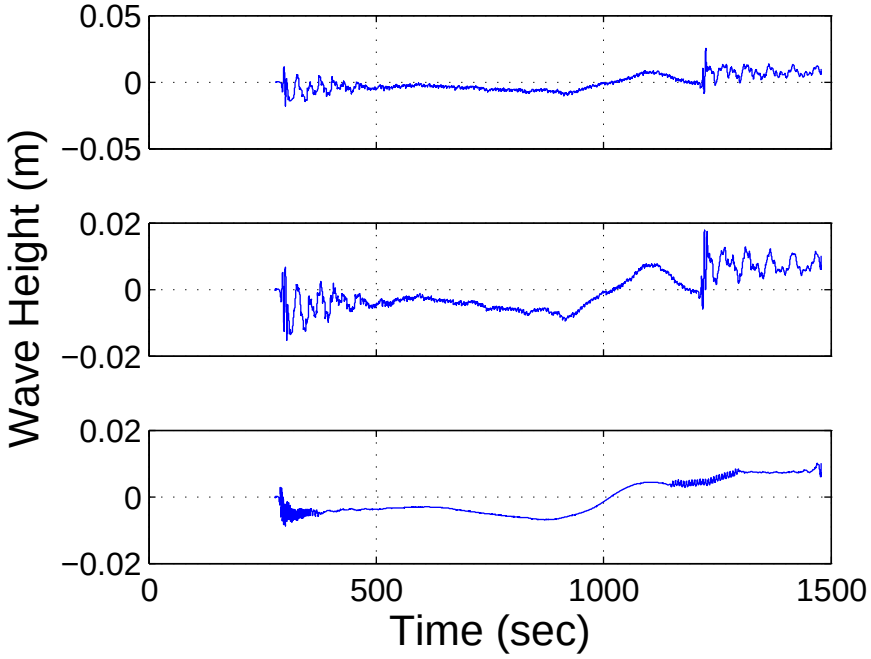

(b)

Figure 3.4: Run 6, (a) Wave Gage 3, $x = 53$ m and (b) Wave Gage 6, $x = 62$ m, smoothed over 1, 2 and 25 wave periods (top to bottom). Stability in this case was achieved after approximately 500 seconds.

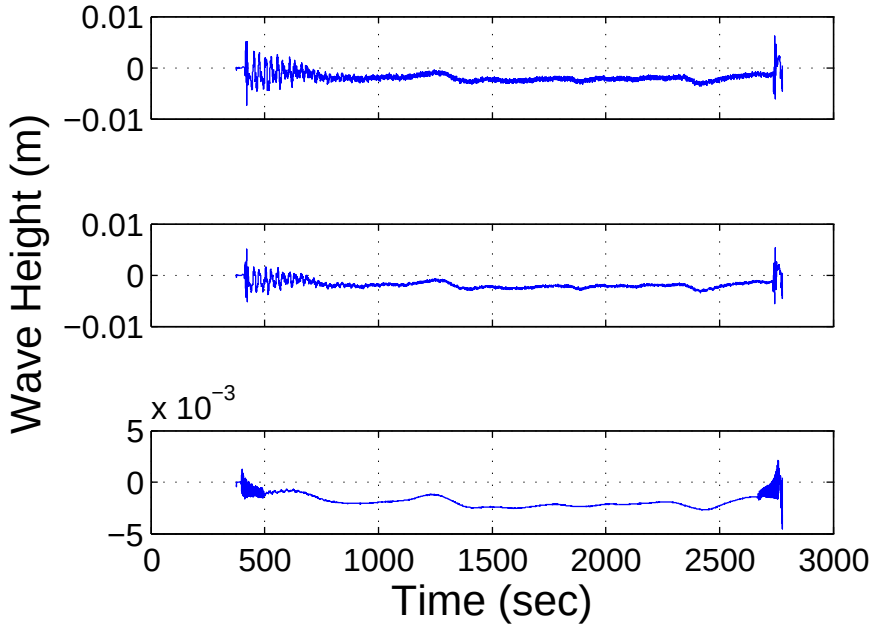

(a)

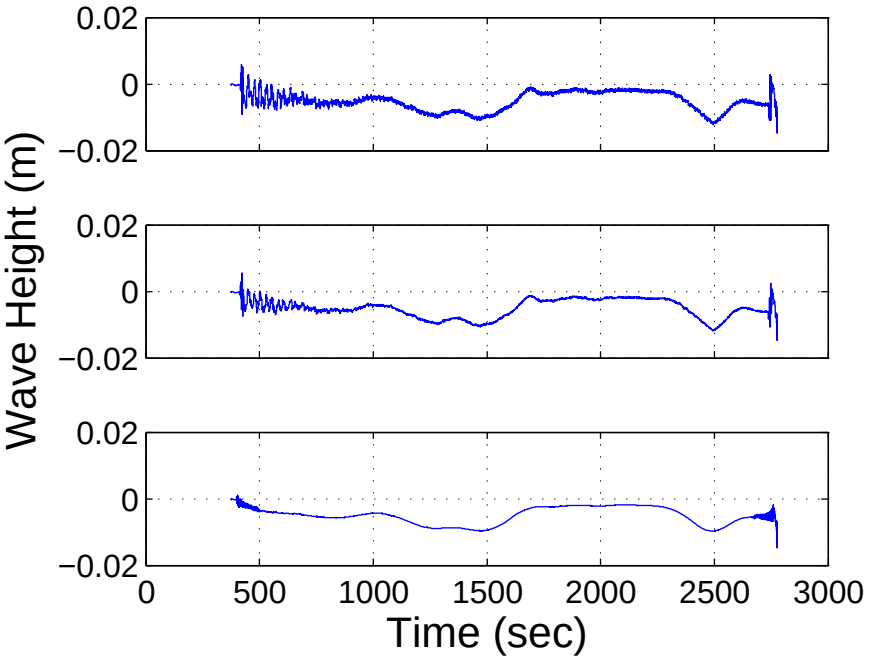

(b)

Figure 3.5: Run 16, (a) Wave Gage 3, $x = 53$ m and (b) Wave Gage 6, $x = 62$ m, smoothed over 1, 2 and 25 wave periods (top to bottom). Stability in this case was achieved after approximately 500 seconds.

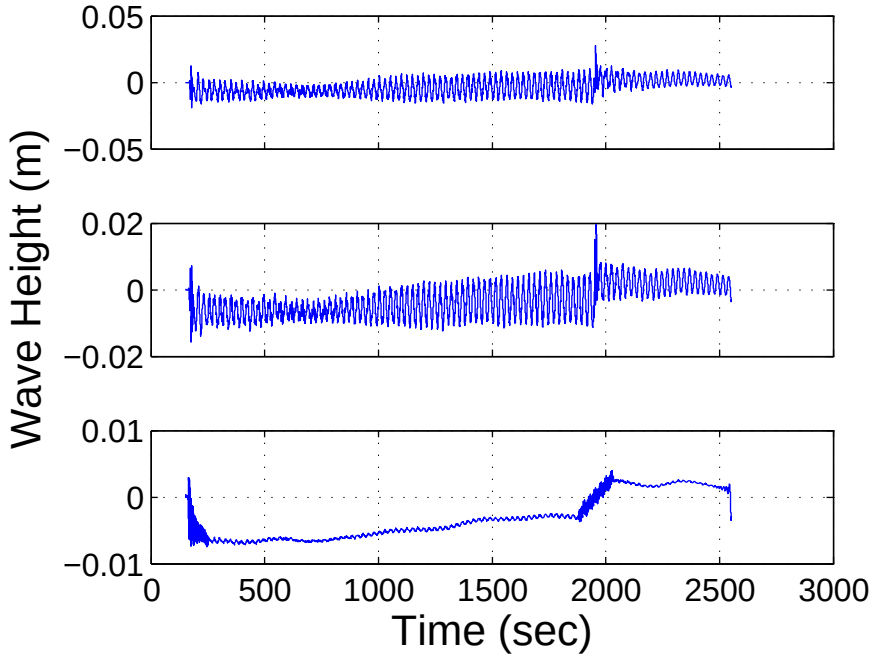

(a)

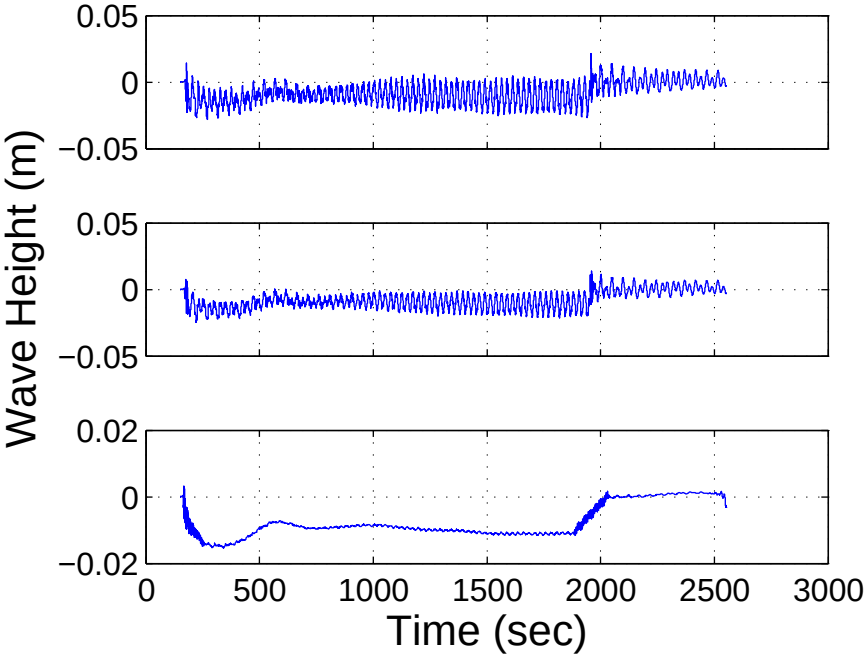

(b)

Figure 3.6: Run 21, (a) Wave Gage 3, $x = 53$ m and (b) Wave Gage 6, $x = 62$ m, smoothed over 1, 2 and 25 wave periods (top to bottom). Stability in this case was achieved after approximately 600 seconds.

3.5.2 Surf Zone

Instruments located in the surf zone include the cart ADVs, the frame ADVs and wave gages 8-12. Moving averages for the wave gages were calculated using equation 3.1 and show similar time scales before high amplitude variations are damped out as the offshore locations.

3.6 Wave Repeatability and Phase Averaged Quantities

Once the tank's stability time had been determined, an offset for calculating phase averages and other quantities was determined for each run. This offset was calculated by rounding down from the observed stability time to the nearest integral multiple of the wave period relative to the time when waves started. Phase averages are calculated by excluding data prior to the stability time, and then locating the first zero upcrossing after this time in the record of free surface and cross shore velocity. The number of waves included in a phase average varied due to the length of a run, but always exceeded 100 waves.

3.6.1 Offshore Phase Averages

Phase averaged free surface profiles for the offshore wave gages and the Q45U are shown in Figures 3.10 - 3.12 for each of the three runs. In Figure 3.10, we can see the wave shoaling further offshore then in Figure 3.11 due to the larger wave height of $H = 20$ cm vs. $H = 12$ cm (Run 6 vs. Run 16). In all three cases, wave repeatability is very good, with narrow confidence intervals at all points in the phase throughout the tank, with the width of the confidence interval averaging ± 3 mm across all gages for all runs.

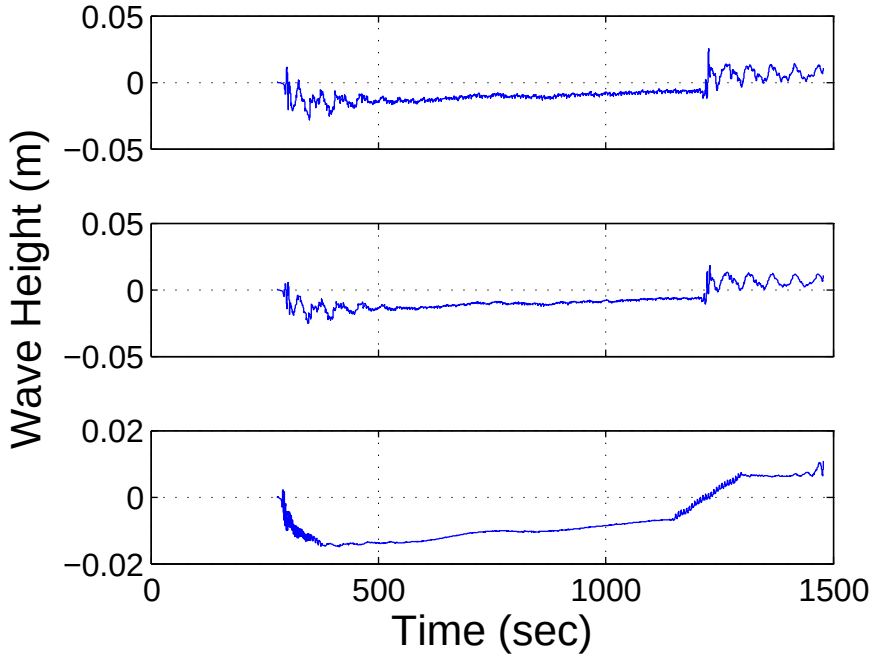

(a)

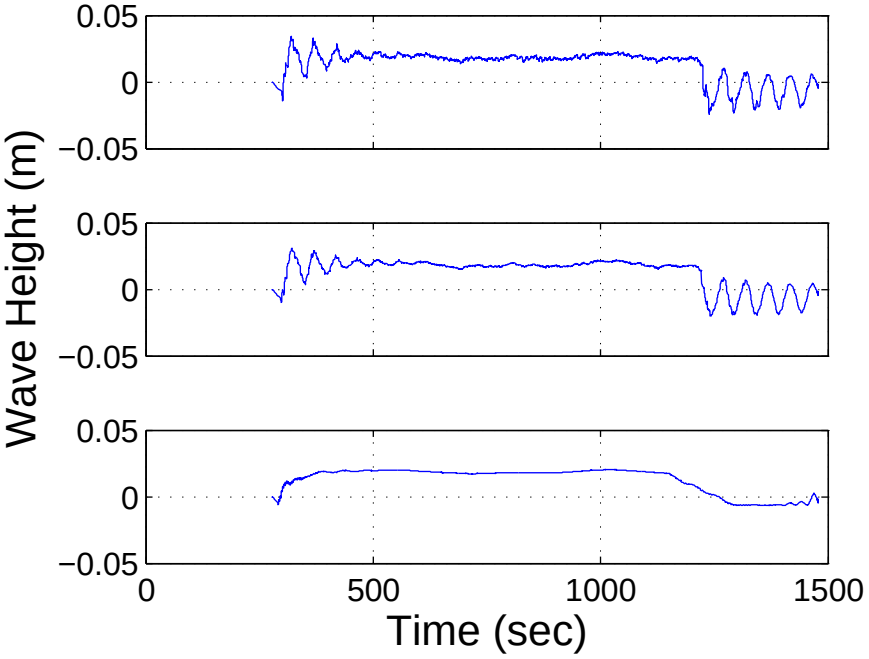

(b)

Figure 3.7: Run 6, (a)Wave Gage 8, $x = 53$ m and (b) Wave Gage 12, $x = 74.9$ m, smoothed over 1, 2 and 25 wave periods (top to bottom panels). Stability in this case was achieved after approximately 200 seconds.

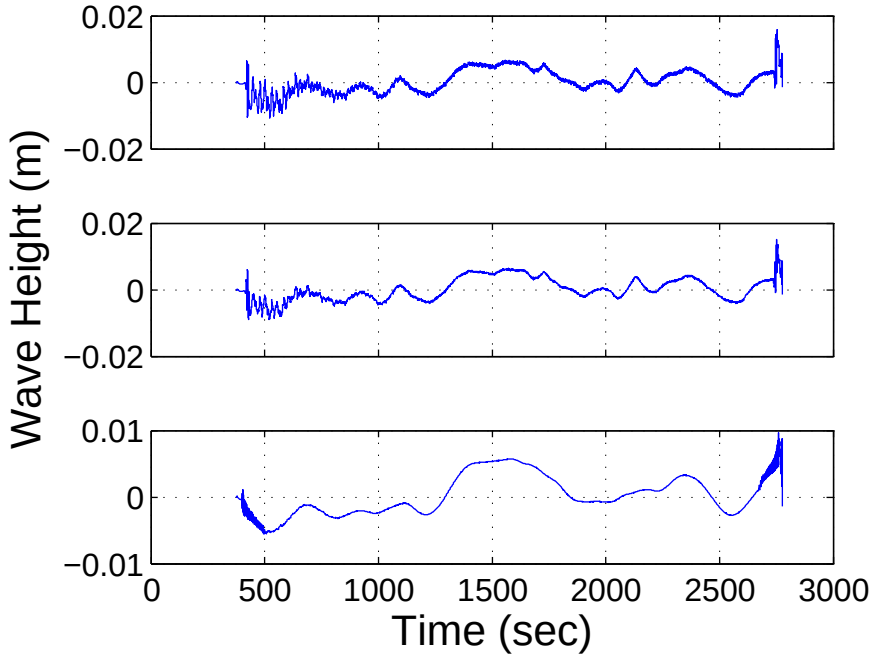

(a)

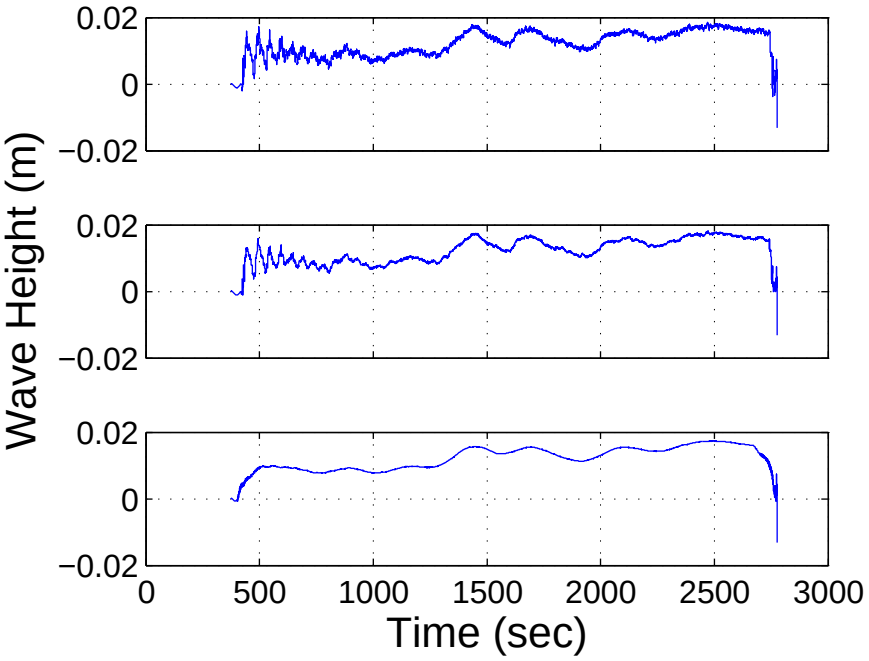

(b)

Figure 3.8: Run 16, (a)Wave Gage 8, $x = 53$ m and (b) Wave Gage 12, $x = 74.9$ m, smoothed over 1, 2 and 25 wave periods (top to bottom panels). Stability in this case was achieved after approximately 500 seconds.

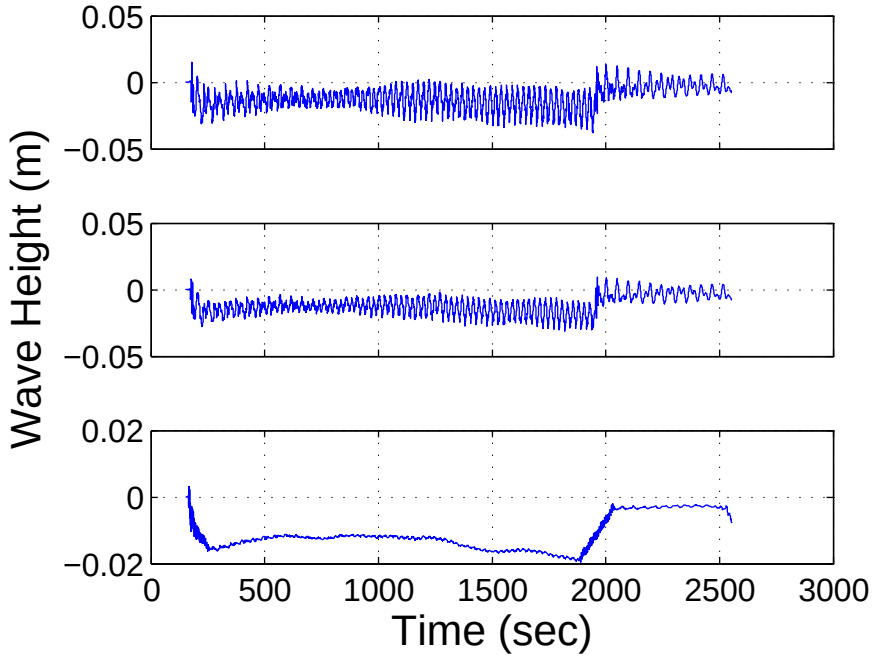

(a)

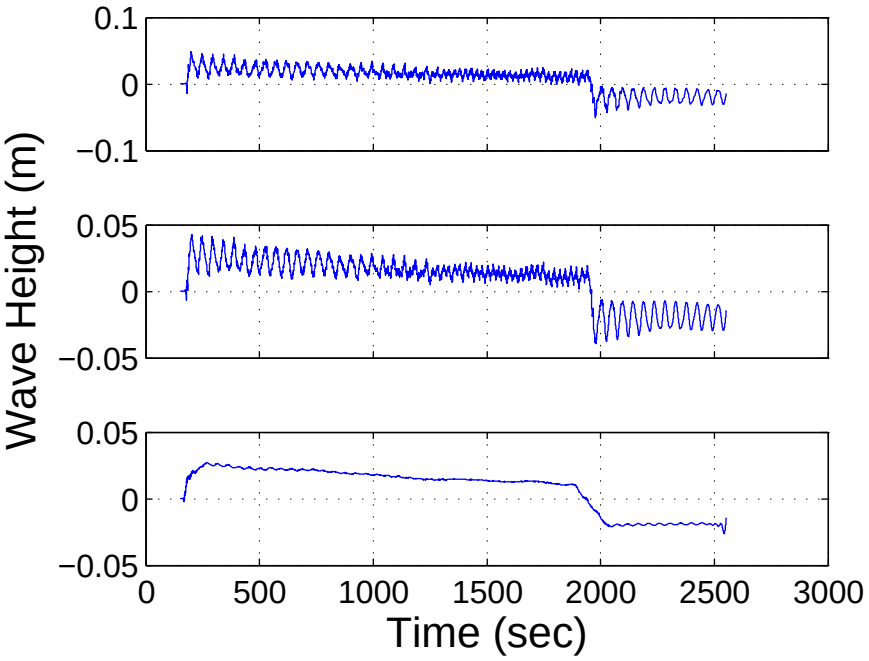

(b)

Figure 3.9: Run 21, (a)Wave Gage 8, $x = 53$ m and (b) Wave Gage 12, $x = 74.9$ m, smoothed over 1, 2 and 25 wave periods (top to bottom panels). Stability in this case was achieved after approximately 600 seconds.

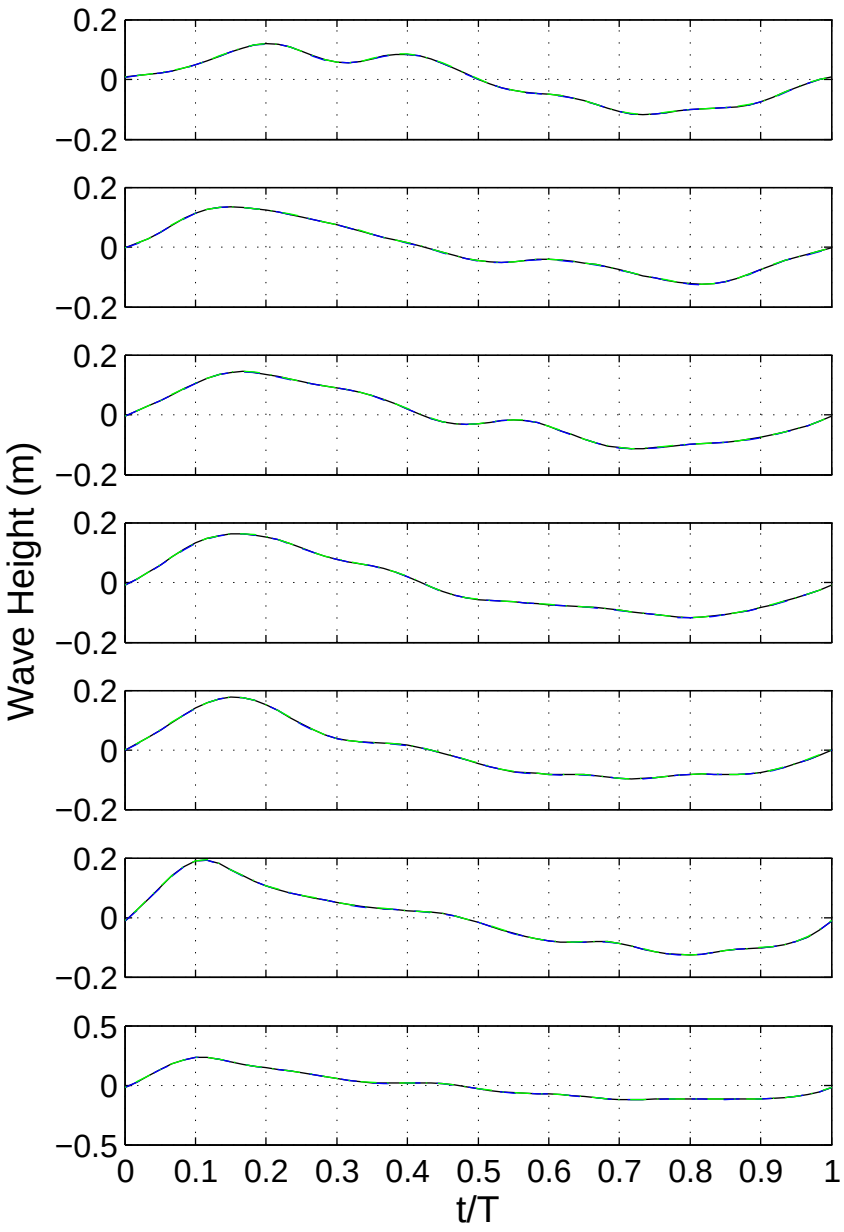

Figure 3.10: Run 6 offshore free surface phase averaged profiles at $x = 20$, 49.2, 51, 52.9, 56.6, 60.2, and 61.9 m respectively (top to bottom). Confidence intervals are shown as $--$ (upper) and $-\cdot-$ (lower).

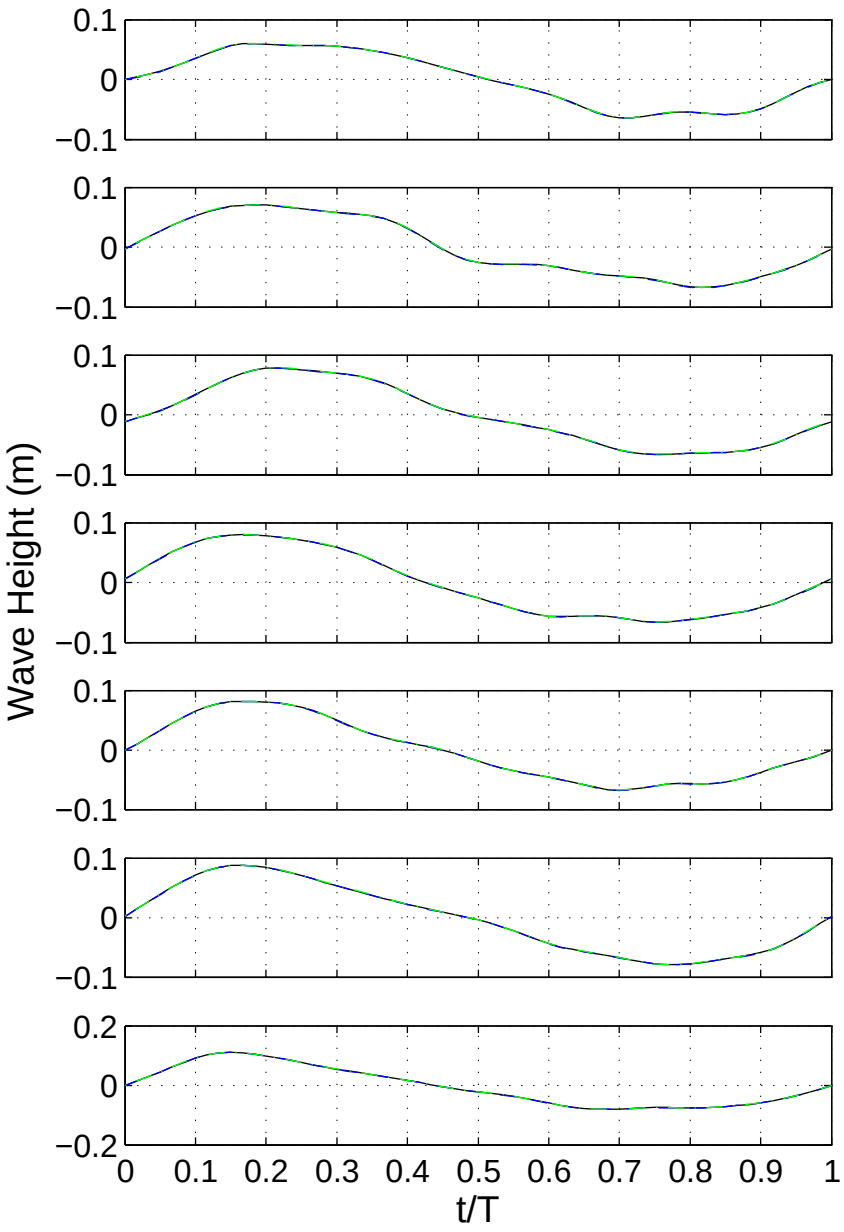

Figure 3.11: Run 16 offshore free surface phase averaged profiles at $x = 20$, 49.2, 51, 52.9, 56.6, 60.2, and 61.9 m respectively (top to bottom). Confidence intervals are shown as $--$ (upper) and $-\cdot-$ (lower).

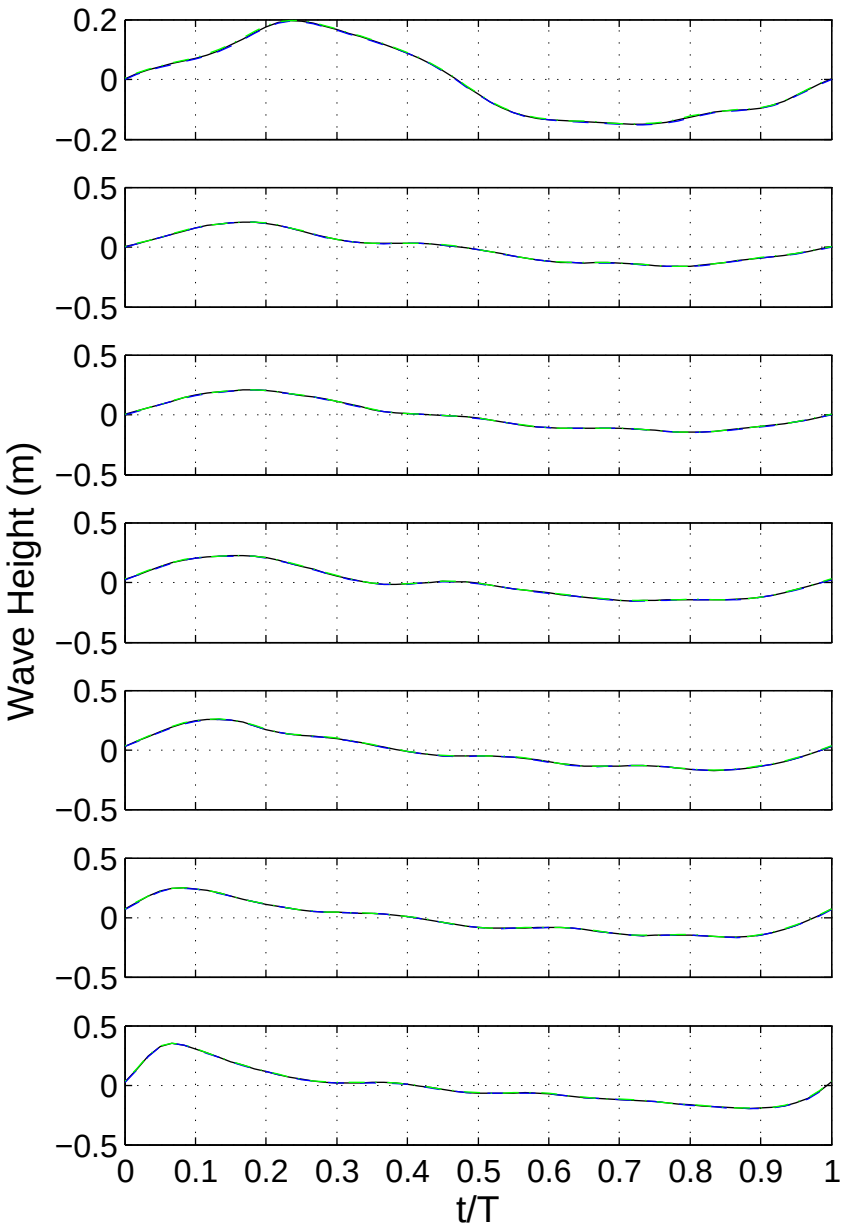

Figure 3.12: Run 21 offshore free surface phase averaged profiles at $x = 20$, 49.2, 51, 52.9, 56.6, 60.2, and 61.9 m respectively (top to bottom). Confidence intervals are shown as $--$ (upper) and $-\cdot-$ (lower).

3.6.2 Surf Zone Phase Averages

Phase averaged results for the surf zone wave gages are presented in Figures 3.13 - 3.15, again with confidence intervals calculated via the bootstrap (mean width $\pm 3mm$ on all gages). As the wave steepens, it begins to take on the more asymmetric shape of a sawtooth wave. The very narrow confidence intervals and smooth shape of the phase averaged free surface indicate a very repeatable wave.

3.6.3 RMS Deviation from the Mean

The RMS deviations from the phase dependent mean are presented in Figures 3.16 - 3.18. The RMS deviation is generally very small except near the start and end of the phase. This is where the wave zero upcrossing occurs, and the higher values are due to variations in the arrival time of the zero crossing.

3.6.4 Free Surface Phase Averages

A single plot of all free surface measurements is presented in Figures 3.19 - 3.21. In these plots slight variations in the wave peak position can be seen, especially as the wave begins to shoal. The free surface profile is fairly uniform in the surf zone once breaking has occurred. There is some variation in the location of the middle (down) zero crossing, but it is fairly consistent across all gages. This variation is most likely due to the shoaling process, wave reflections, and variations in the actual phase of the wave (compression and lengthening).

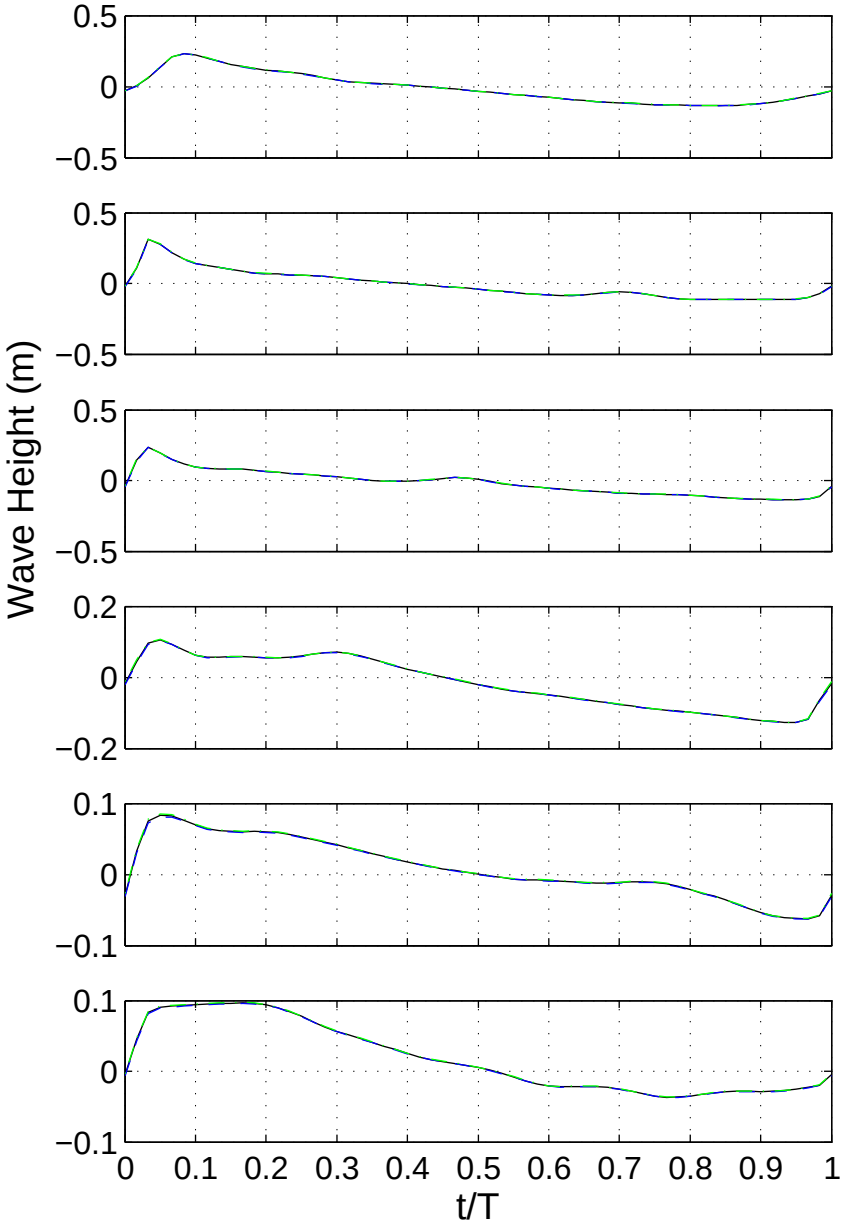

Figure 3.13: Run 6 surf zone free surface phase averaged profiles at x = 63.3, 65, 66.5, 67.4, 71.2, 74.9 m respectively (top to bottom). Confidence intervals are shown as $--$ (upper) and $-\cdot-$ (lower).

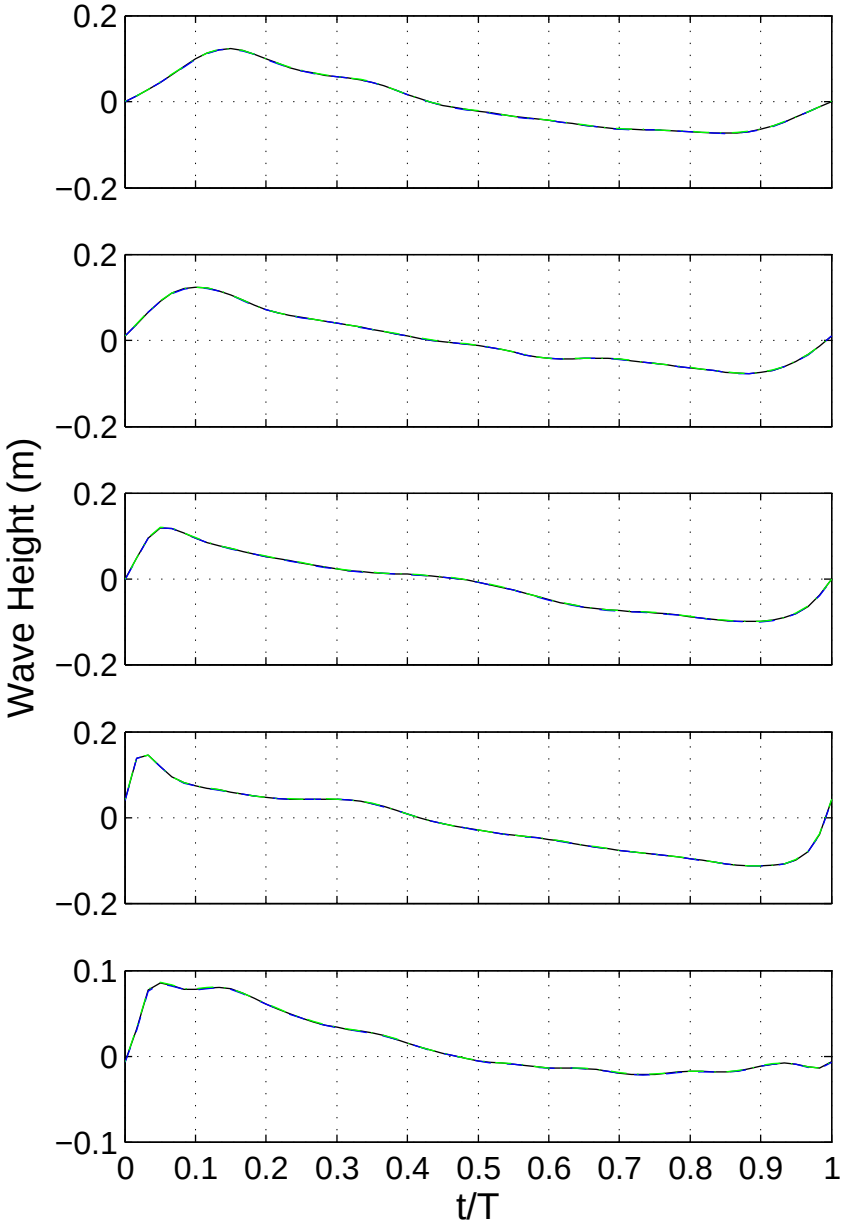

Figure 3.14: Run 16 surf zone free surface phase averaged profiles at $x = 63.3$, 66.5, 67.4, and 74.9 m respectively (top to bottom). Confidence intervals are shown as $--$ (upper) and $-\cdot-$ (lower).

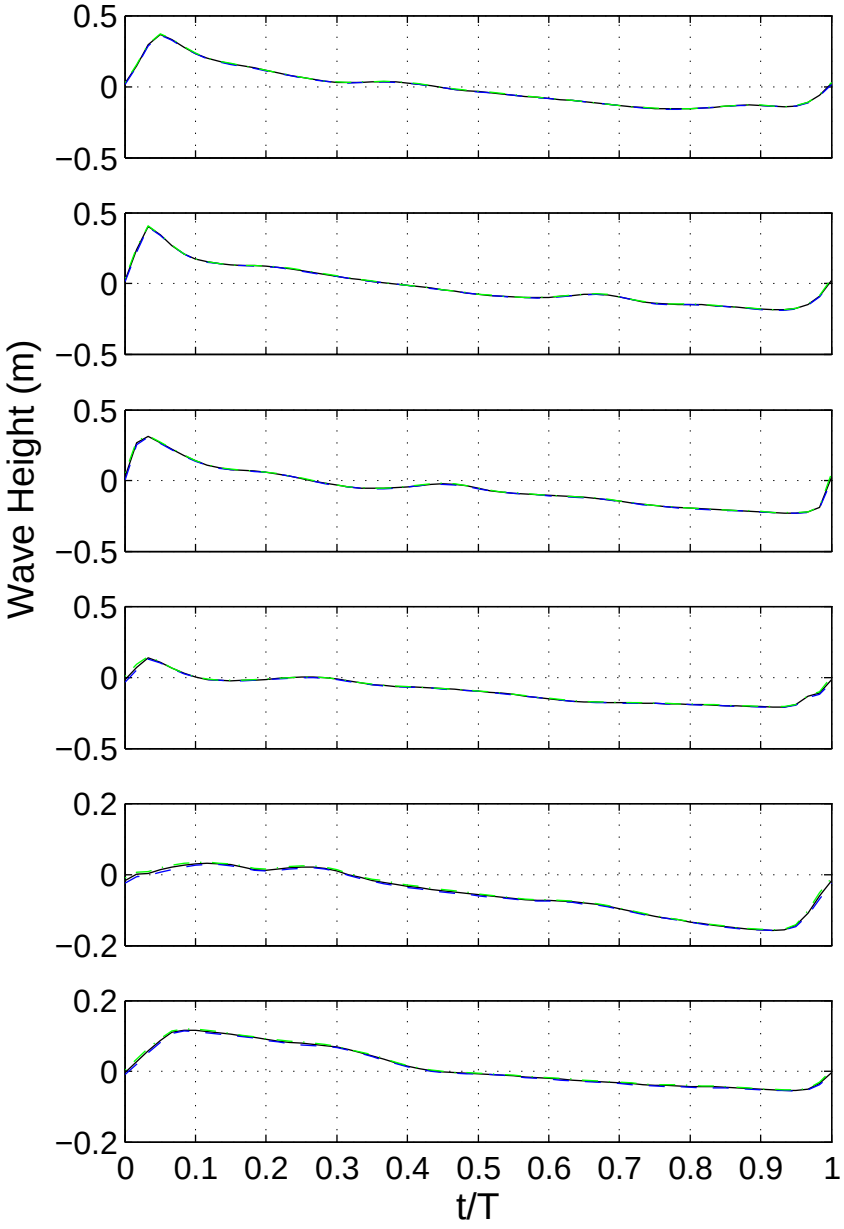

Figure 3.15: Run 21 surf zone free surface phase averaged profiles at $x =$ 65, 66.5, 67.4, 71.2, and 74.9 m respectively (top to bottom). Confidence intervals are shown as $--$ (upper) and $-\cdot-$ (lower).

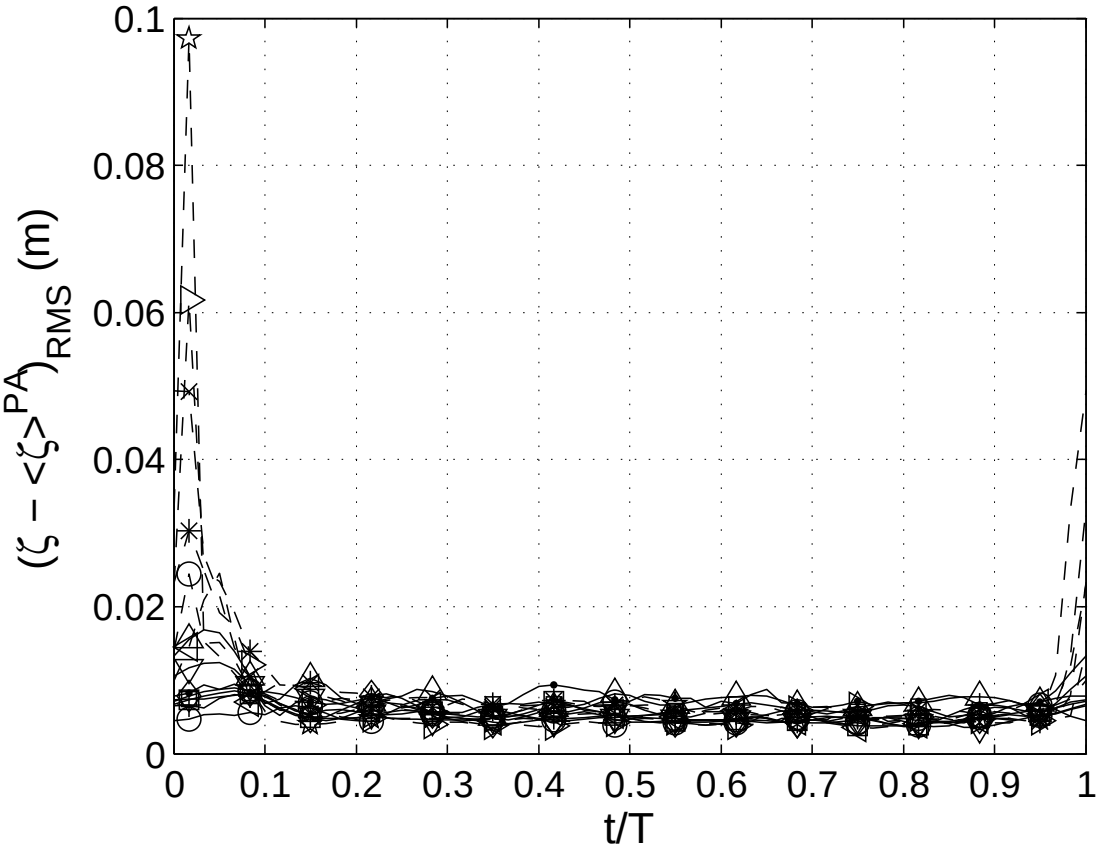

Figure 3.16: Run 6 RMS deviation from the phase averaged free surface profile. Wave gages $1 - 13$ are represented by $\cdot$, $\circ$, $+$, $\square$, $\diamond$, $\bigtriangledown$, $\bigtriangleup$, $\lhd$, $\rhd$, $\star$, x, $*$, $\circ$, and the Q45U by $\square$. Gages with a maximum RMS value greater than 0.02 are designated by a dashed line.

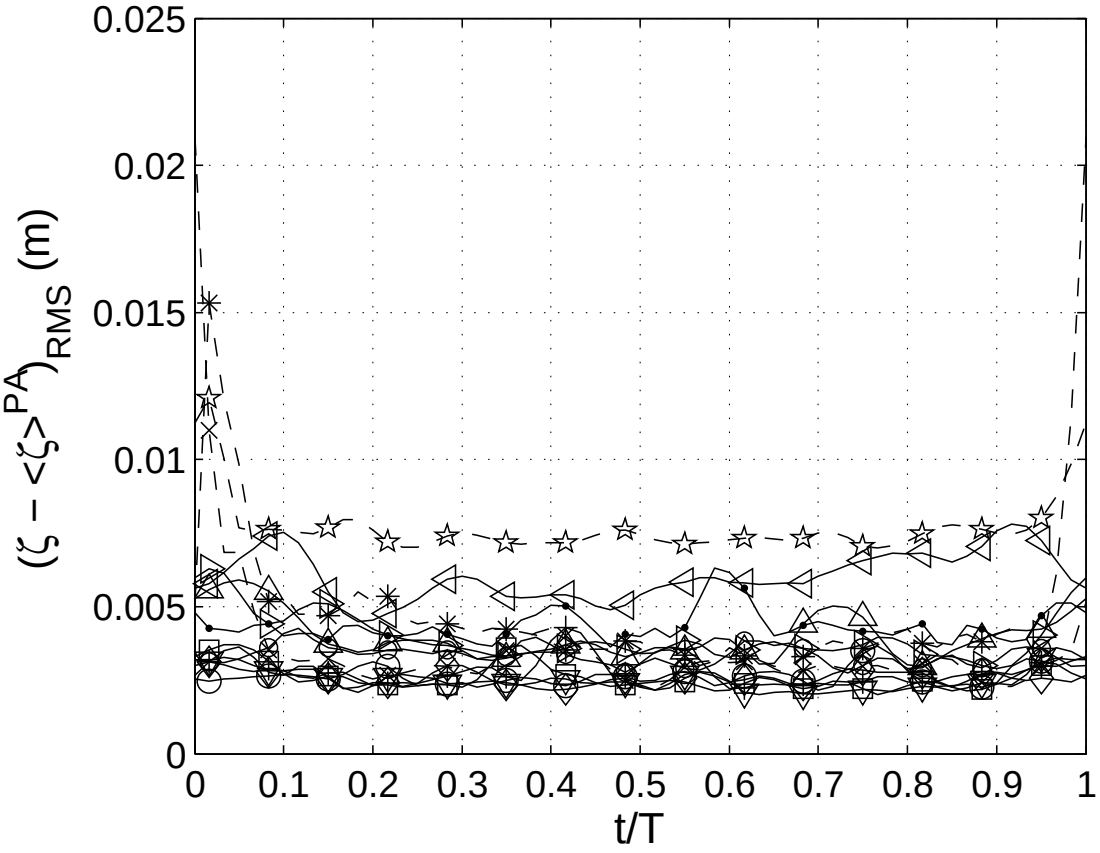

Figure 3.17: Run 16 RMS deviation from the phase averaged free surface profile. Wave gages $1 - 13$ are represented by $\cdot$, $\circ$, $+$, $\square$, $\diamond$, $\bigtriangledown$, $\bigtriangleup$, $\lhd$, $\rhd$, $\star$, x, $*$, $\circ$, and the Q45U by $\square$. Gages with a maximum RMS value greater than 0.01 are designated by a dashed line.

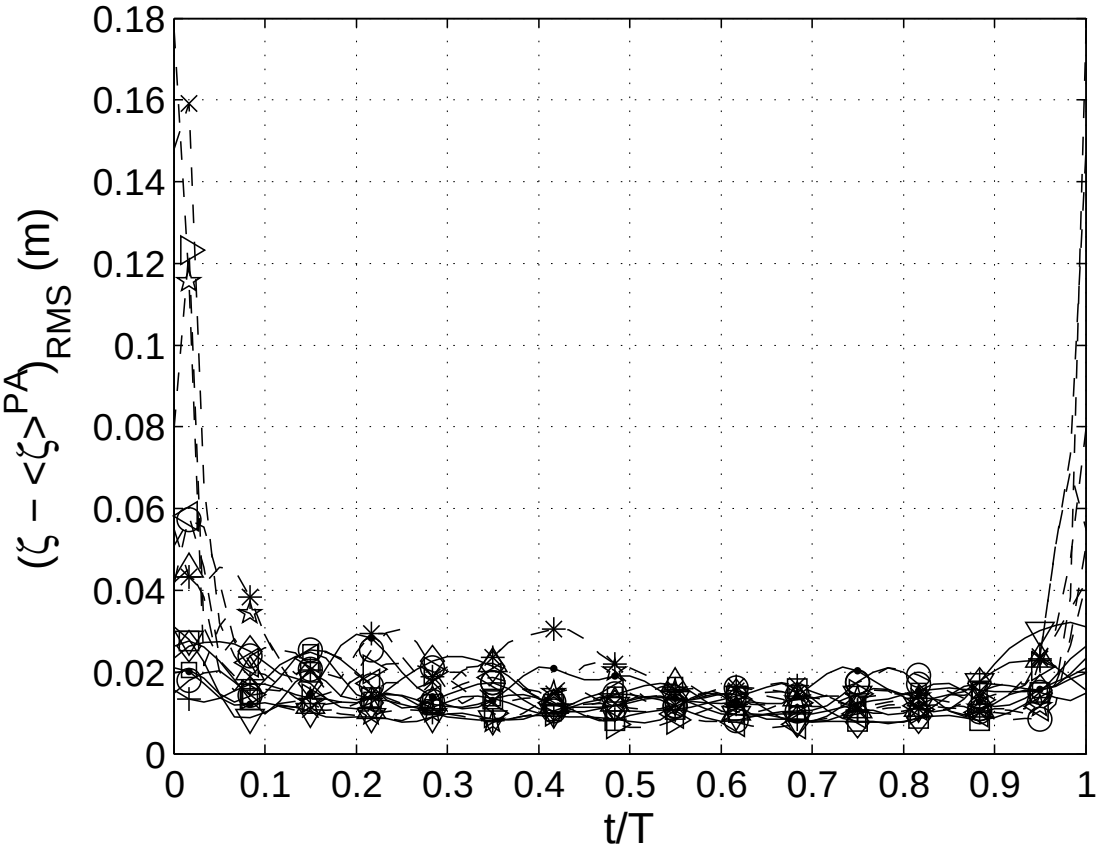

Figure 3.18: Run 21 RMS deviation from the phase averaged free surface profile. Wave gages $1 - 13$ are represented by $\cdot$, $\circ$, $+$, $\square$, $\diamond$, $\bigtriangledown$, $\bigtriangleup$, $\lhd$, $\rhd$, $\star$, x, $*$, $\circ$, and the Q45U by $\square$. Gages with a maximum RMS value greater than 0.04 are designated by a dashed line.

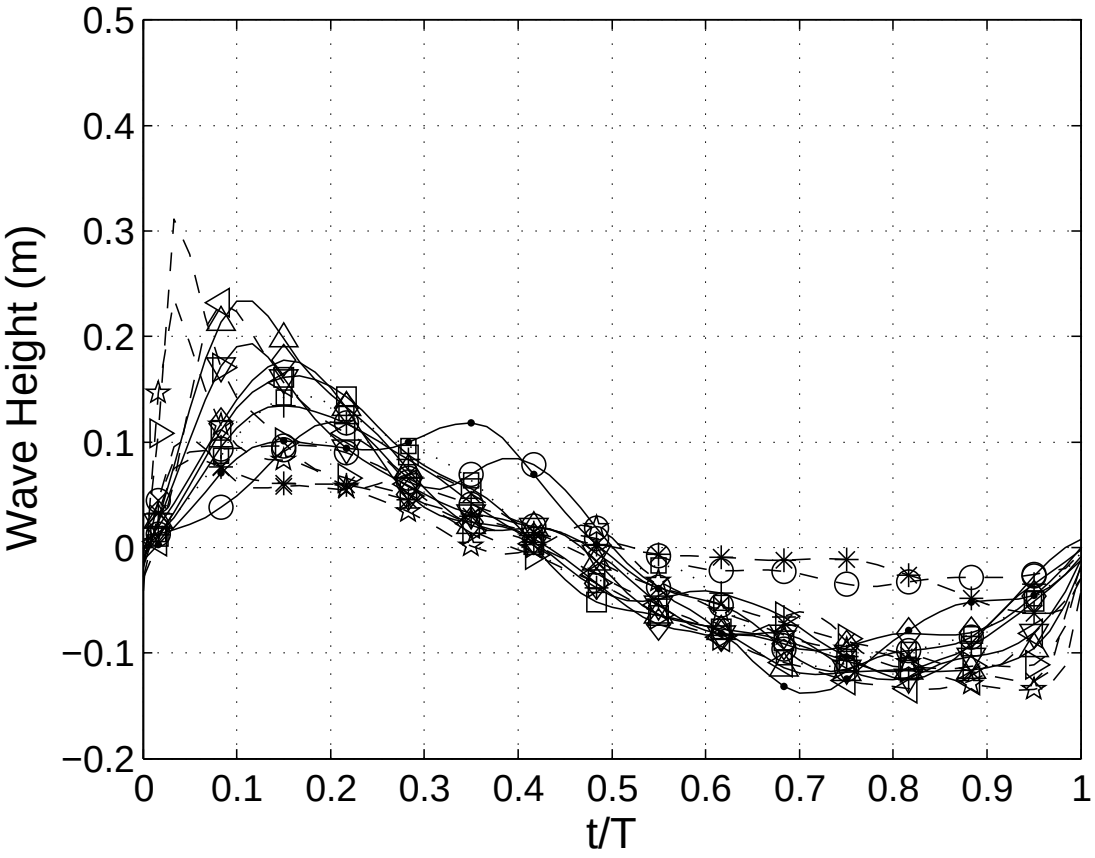

Figure 3.19: Run 6, Phase averaged free surface profiles at all locations. Wave gages $1 - 13$ are represented by $\cdot$, $\circ$, $+$, $\square$, $\diamond$, $\bigtriangledown$, $\bigtriangleup$, $\lhd$, $\rhd$, $\star$, x, $*$, $\circ$, and the Q45U by $\square$. Gages with a maximum RMS value greater than 0.2 are designated by a dashed line.

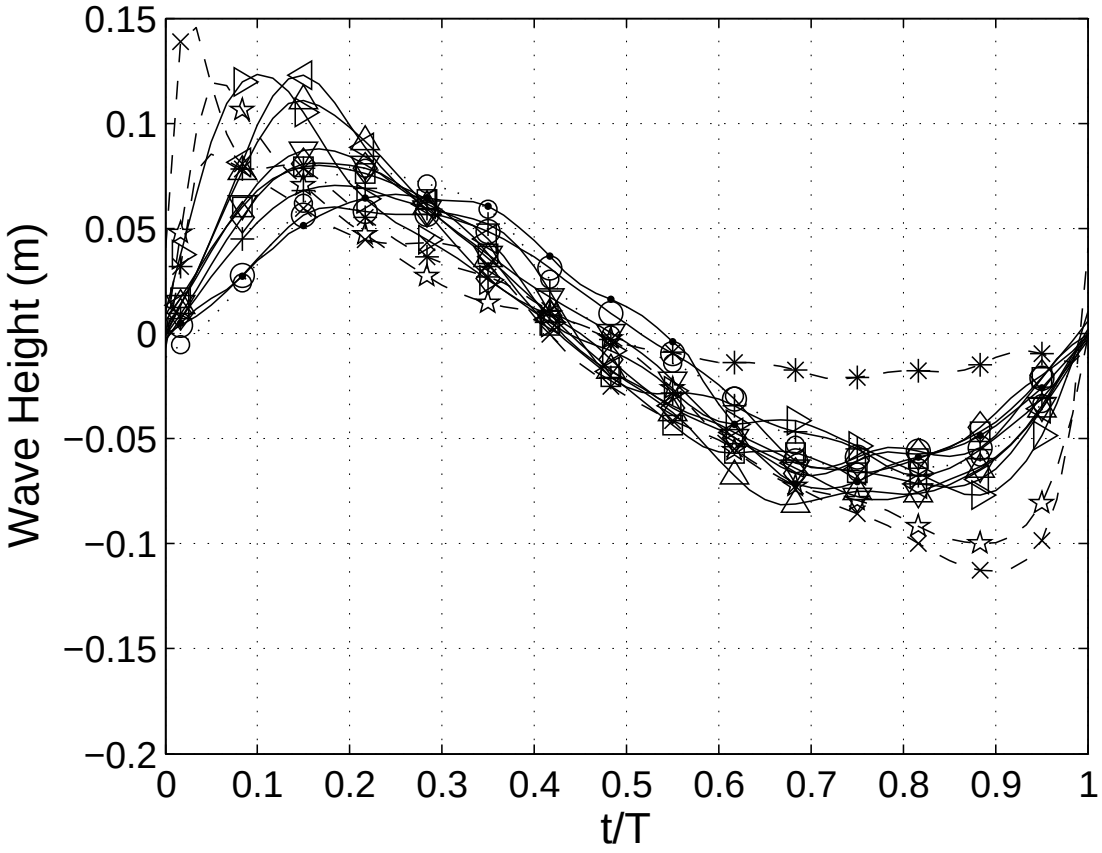

Figure 3.20: Run 16, Phase averaged free surface profiles at all locations. Wave gages $1-13$ are represented by $\cdot$, $\circ$, $+$, $\square$, $\diamond$, $\bigtriangledown$, $\bigtriangleup$, $\lhd$, $\rhd$, $\star$, x, $*$, $\circ$, and the Q45U by $\square$. Gages with a maximum RMS value greater than 0.01 are designated by a dashed line.

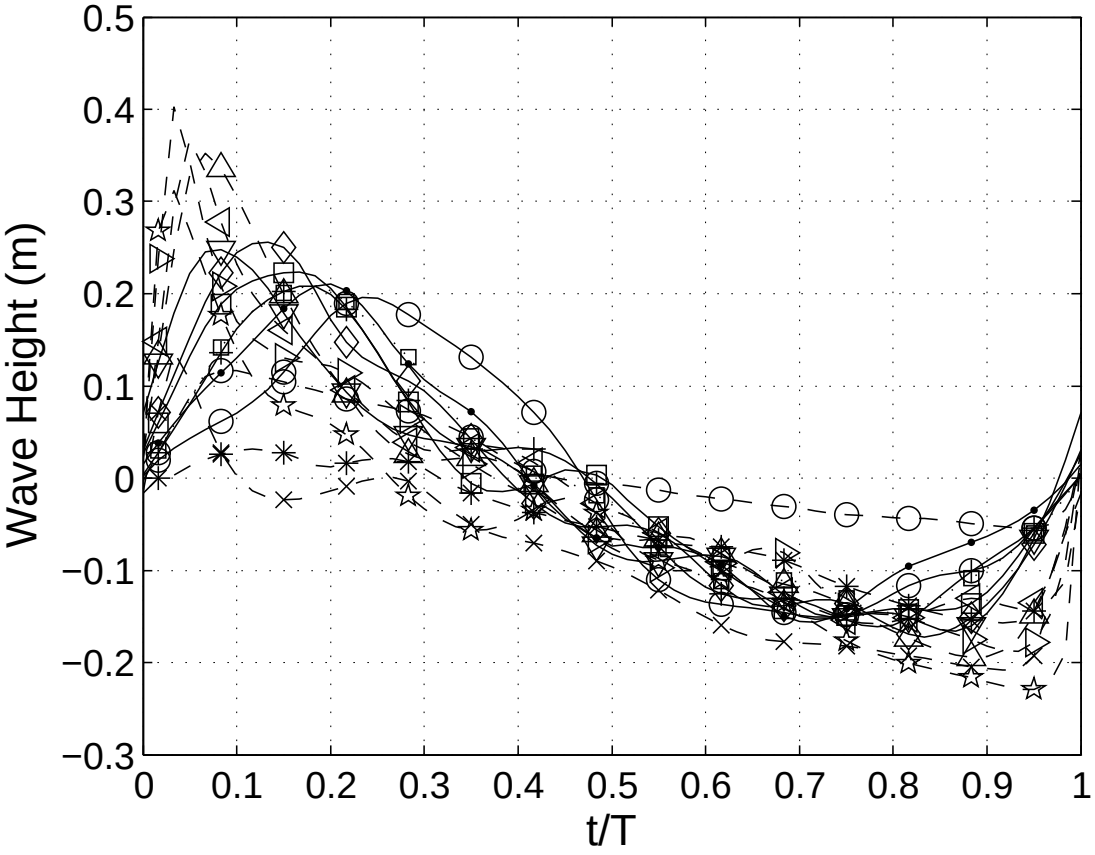

Figure 3.21: Run 21, Phase averaged free surface profiles at all locations. Wave gages $1-13$ are represented by $\cdot$, $\circ$, $+$, $\square$, $\diamond$, $\bigtriangledown$, $\bigtriangleup$, $\lhd$, $\rhd$, $\star$, x, $*$, $\circ$, and the Q45U by $\square$. Gages with a maximum RMS value greater than 0.04 are designated by a dashed line.

3.7 Mean Water Level and Setup

Given the instantaneous free surface profiles, we can compute the time averaged mean free surface profile $\overline{\zeta}(x) = h + \overline{\eta}$, where h is the local still water depth, and $\overline{\eta}$ is the time averaged mean free surface displacement. Using phase averaged quantities, the wave envelope is also plotted, with the crest chosen as the maximum phase averaged value at a given location and the trough the associated minimum value. Results are presented in Figures 3.22 - 3.24. The shoaling and approximate breaking locations are consistent with visual observations. In Run 21, Figure 3.24, there also appears to be secondary breaking occurring past $x = 75$ m as the wave shoals again.

The wave gage data is used to estimate the mean free surface in the surf zone via empirical formulations found in Mei (1989). This allows comparison with prior work in the surf and swash and a check on the consistency of our experiments with empirical knowledge. In general, our results agree well in form with the known empirical formulations. There are obvious discrepancies between the data and empirical formulations, with the predicted MWL generally lower then the recorded value. These differences are easily attributed to large uncertainty in the breaking wave height and to a lesser extent the still water level. While closer agreement between the data and calculated values would be nice, the important thing to note here is that the LWF behaves as we empirically think it should.

An important parameter in the empirical estimates of the mean free surface and in describing the surf zone is the ratio of breaking wave height, H_b, to still water depth at the break point, h_b, here symbolized by

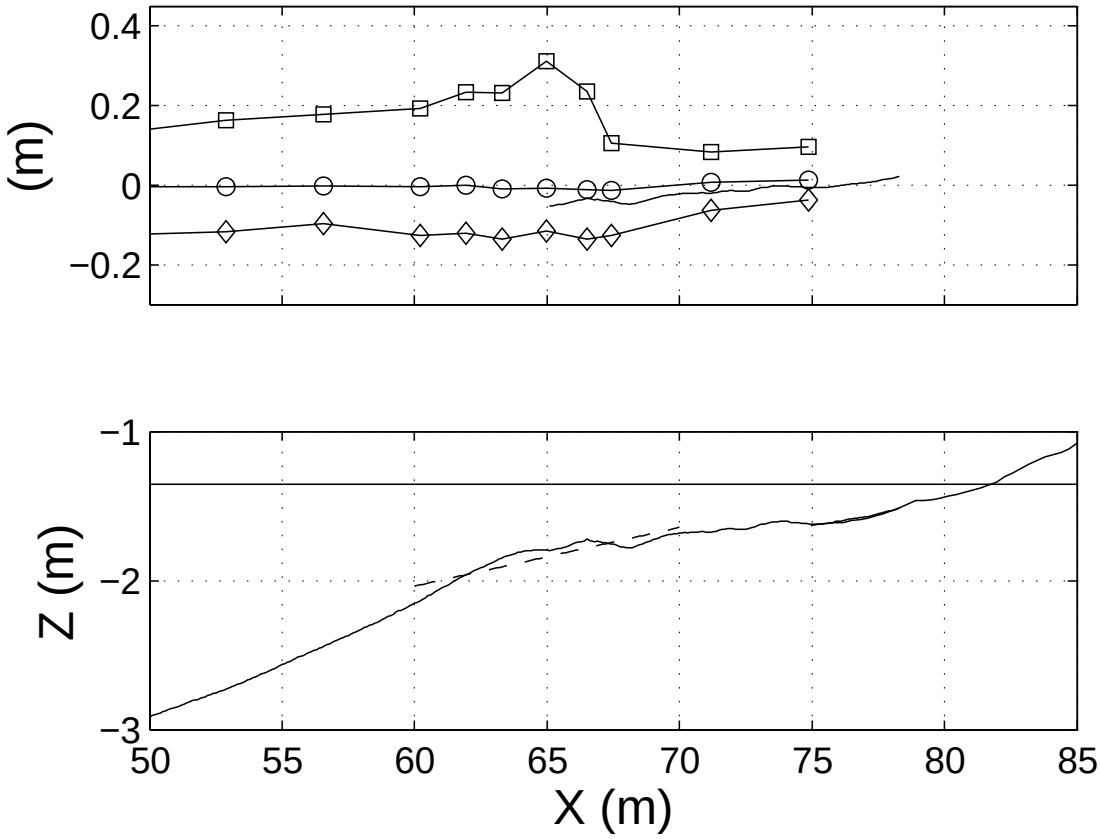

Figure 3.22: Run 6, Top plot, mean water level (solid line, no marker theory, solid line with ∘ from data). The wave envelope is also plotted (solid lines with □ and ◇). The bottom plot shows the before run bathymetry with the dashed line representing the region over which the slope was calculated to estimate wave breaking quantities.

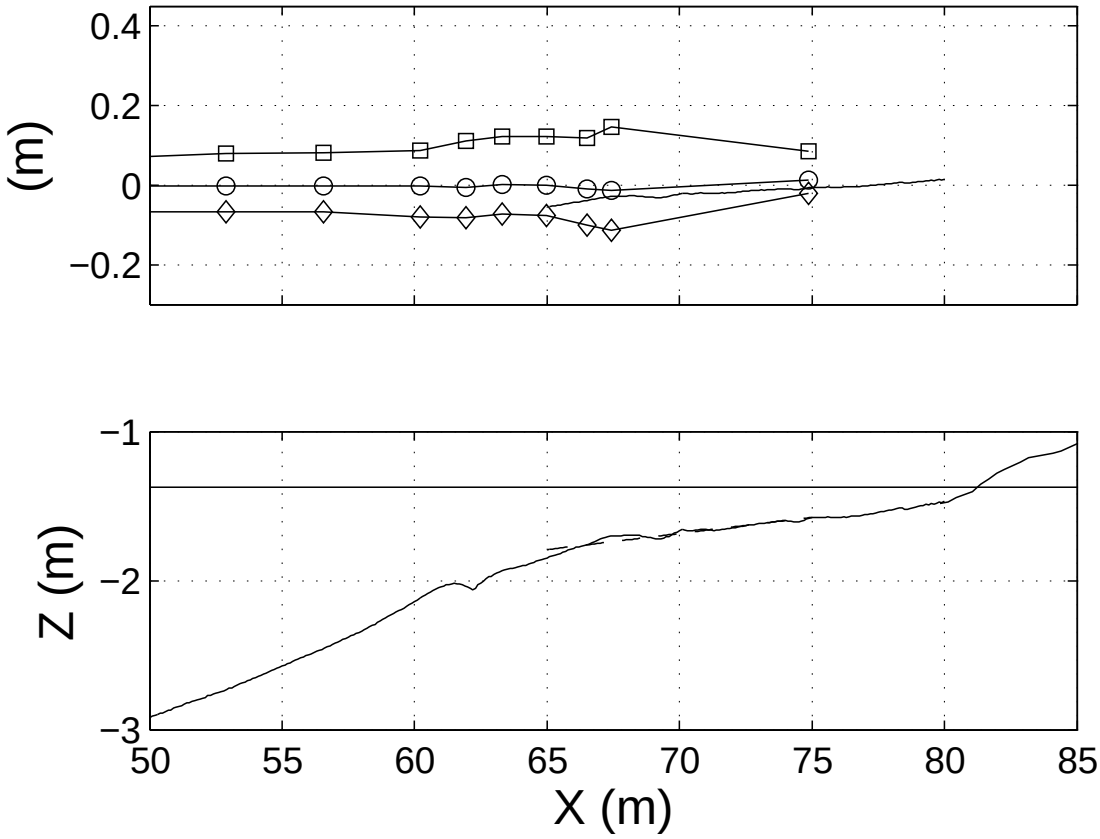

Figure 3.23: Run 16, Top plot, mean water level (solid line, no marker theory, solid line with ∘ from data). The wave envelope is also plotted (solid lines with □ and ◇). The bottom plot shows the before run bathymetry with the dashed line representing the region over which the slope was calculated to estimate wave breaking quantities.

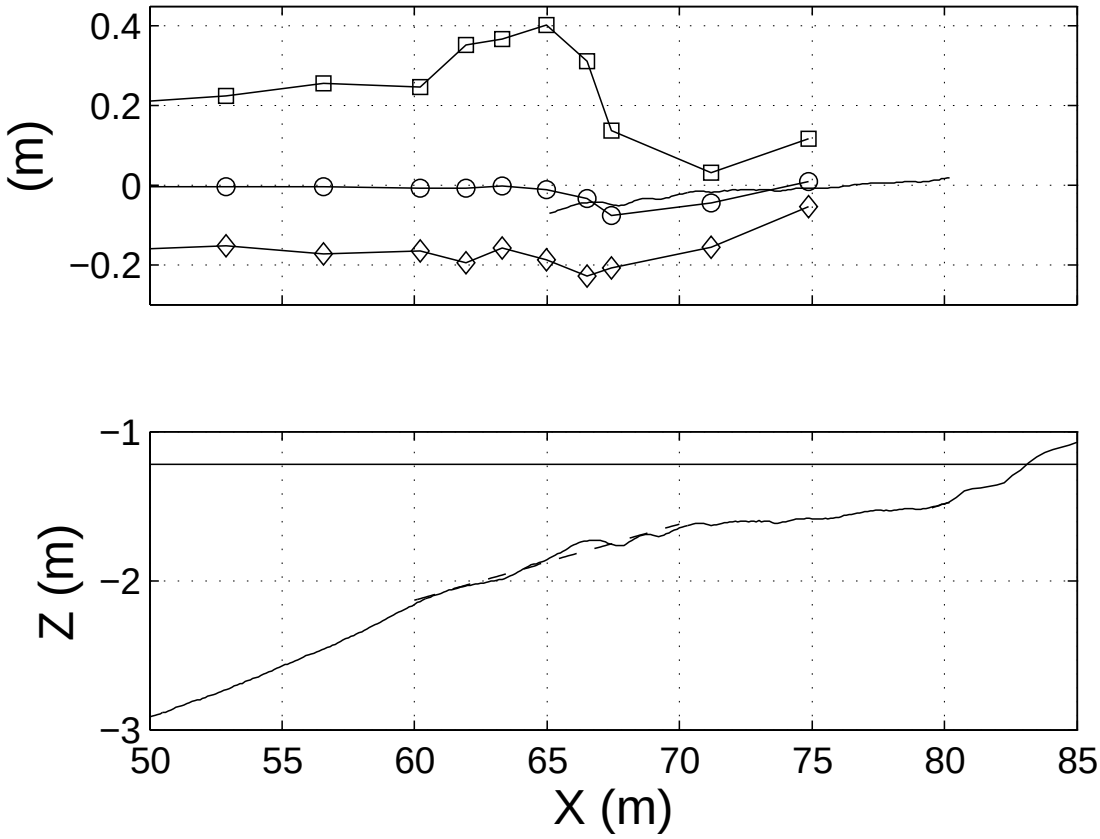

Figure 3.24: Run 21, Top plot, mean water level (solid line, no marker theory, solid line with ∘ from data). The wave envelope is also plotted (solid lines with □ and ◇). The bottom plot shows the before run bathymetry with the dashed line representing the region over which the slope was calculated to estimate wave breaking quantities.

$$\gamma_b = \frac{H_b}{h_b} \tag{3.11}$$

This ratio has been found experimentally to vary from 0.7 to 1.2 (Battjes, 1974) by numerous researchers. Our values (Table 3.3) are generally on the low end for the plunging wave condition, meaning we are dealing with a weakly plunging wave, coupled with uncertainty in the breaking location which may bias these estimates low since the breaking wave height H_b will be underestimated. This occurs for instance in Run 16, where for a wave with a similar value of ξ, Ting and Kirby (1994) found the ratio $\gamma = 0.8$, consistent with the results Battjes (1974) presented for all experiments.

The following empirical formulation (equations 3.12 - 3.14) is presented in full in Mei (1989). In the following section, a subscript b refers to a value at breaking. Using conservation of energy from offshore to the break point, we can estimate the water depth at the break point as

$$h_b = \frac{g}{\omega^2}\left(\frac{\omega^2 A_o}{\gamma_b g}\right)^{\frac{4}{5}} (2|\cos\alpha_o|)^{-\frac{1}{2}} \tag{3.12}$$

Where $\omega = 2\pi f$, A_o is the offshore wave amplitude, g is gravity, and α_o is the incident wave angle, in this case zero.

With an estimate of h_b it is simple to use the definition of γ_b to estimate the breaking wave height, H_b. Using $\gamma_b = .85$, the mean value given by Battjes (1974), H_b is then calculated and from the definiton of γ. The final value we need to estimate to predict the mean free surface in the surf zone is the value of the mean free surface at the breaking point. It can be empirically estimated as

$$\overline{\zeta}_b = -\frac{H_b^2}{16 h_b} \tag{3.13}$$

With the above estimates for H_b, h_b, and $\overline{\zeta}_b$, the mean free surface in the surf zone can be calculated using the following equation

$$\overline{\zeta}(x) = \overline{\zeta}_b + \frac{\frac{3}{8}\gamma^2}{1+\frac{3}{8}\gamma^2}(h_b - h(x)) \tag{3.14}$$

This is shown as a solid line with no marker in Figures 3.22 - 3.24. This empirical estimate of the mean water level generally agrees well with our data, although it is consistently lower than the recorded water levels. As these are only empirical relations and several assumptions are made in estimating the MWL, the small discrepancies are not a major concern.

3.8 Pressure Measurement in the Swash Zone

For Runs 17 - 25 a pressure sensor array was installed in the beach to examine pore water pressure in the swash zone. The pressure signals are zeroed against the mean value from 60 seconds after waves started to 60 seconds before waves ended. The start of phase zero crossing is identified by subtracting the temporal mean of all points in the phase average (i.e. all points in the time interval from the run's stability time to the number of periods considered for the phase average, typically 100, or approximately 10 minutes of data) and then finding the first zero crossing after the stability time of this re-centered signal. Phase averaging is carried out on the zeroed, but not re-centered, signal.

Removing the mean is the simplest way to re-center the signal to identify the zero crossing, but several sensors show linear or higher order trends (Figure 3.28) which will affect the location of the zero crossing and the phase averaged values. Identification of this trend will depend on selecting an appropriate time scale over which to average or smooth the data in order to fit a polynomial and detrend the

signal. This has not been done in the present analysis because the cause of these trends and the lack of consistency between sensors can not be presently explained.

Horizontal profiles at various points in the phase for Run 21 are shown in Figure 3.25. Wave propagation is from left to right on the plots, and each sensor has undergone the zeroing and phase averaging process above. The bathymetry above the pressure sensors and the pressure sensor locations are shown in Figure 3.26. The arrival of the bore front is not indicated by a sharp pressure gradient approaching shore, but by a surging motion of the free surface up the slope, confirmed by visual observation of the swash. About halfway through the phase, a standing wave develops in the middle of the array which gradually moves offshore with the flow reversal. Once the flow reverses, pressure becomes negative as the beach becomes a seepage face and water drains from the sediment pores. Video records taken of the swash zone with a digital video camera may also provide some clues as to the interpretation of the pressure data.

Phase averaged time series for select sensors are shown in Figure 3.27. Note the more dynamic environment offshore and the much smaller variation in pressure at the furthest onshore locations. As the flow progresses up the slope, it loses energy primarily to dissipation and friction with the bed. This loss of energy is manifested in smaller changes in the free surface elevation at the more onshore pressure sensors. There are slight variations in the shape of the wave with x position due to the downrush of water during the sheet flow regime and the standing waves which develop. Visual observation of the swash revealed along shore reflections and bathymetric effects which also complicate the flow. The sharper changes in the profile which involve only one sensor are more likely caused by poor sensor response however.

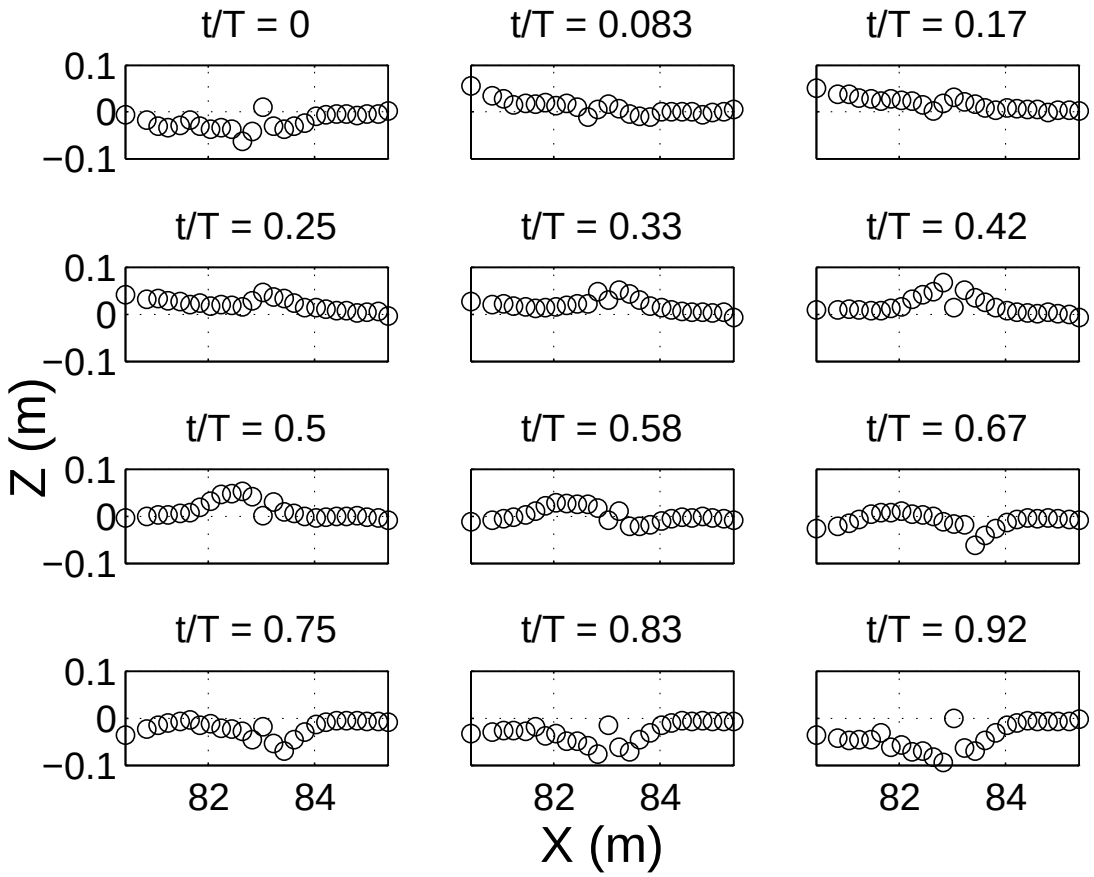

Figure 3.25: Run 21horizontal profiles at various points in the phase. Notice the surging motion indicating the arrival of the bore front and the standing wave which develops during the down rush phase.

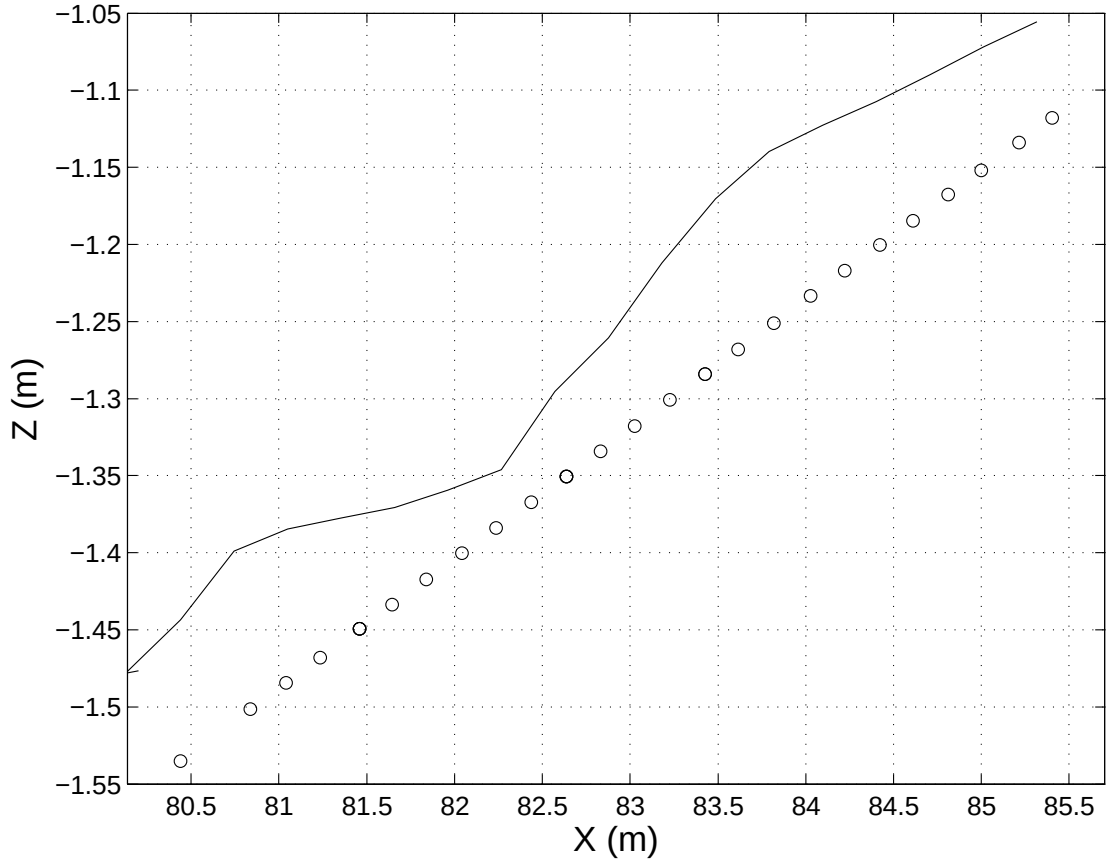

Figure 3.26: Run 21 pressure sensor locations and bathymetry at start of the run. The array slope was determined by fitting a line to the still water, non-zeroed sensor values. Positions were calculated relative to the most offshore sensor location which was surveyed during installation.

While the most onshore gages show little variation, they always exhibit an increase in pressure with the arrival of the first waves (Figure 3.28) that remains relatively constant throughout the run. Note how some sensors have obvious linear trends (the higher order trends occur in sensors not shown on the plots) while others have nearly constant values during the run. One unusual feature of the lowpass filtered data is the sudden drop in pressure at $t = 500$ s on the gage at $x = 83.4$ m. The sensor performs well after this drop although it has a stronger downward slope than the other plotted sensors. From Figure 3.28, it is apparent the soil drains between runs when the tank is quiescent and becomes resaturated quickly within the first few waves indicating a medium to high porosity.

3.9 Offshore Phase Averaged and Mean Velocity Profile

Phase averaged velocity profiles and contours from the ADCP are presented in Figures 3.29 - 3.34. The profiles also contain 95% confidence intervals calculated via the bootstrap. While the confidence intervals tend to widen near the surface,this is due more to beam divergence, and very near the surface, return echo interference, rather then higher uncertainty in the wave velocity field. The free surface band of contaminated data has been removed from each ADCP record.

Comparisons to linear wave theory (not shown) are very good over the middle portion of the water column. The boundary layer structure near the bottom of the profile is not the bottom wave induced boundary layer (which should only be a few centimeters thick). It is more likely due to the wave induced velocity field growing weaker far below the surface. While not plotted, comparisons between the ADCP and Nortek Vector velocity records are extremely good as well.

The offshore velocity shows little turbulence, except near the surface which is

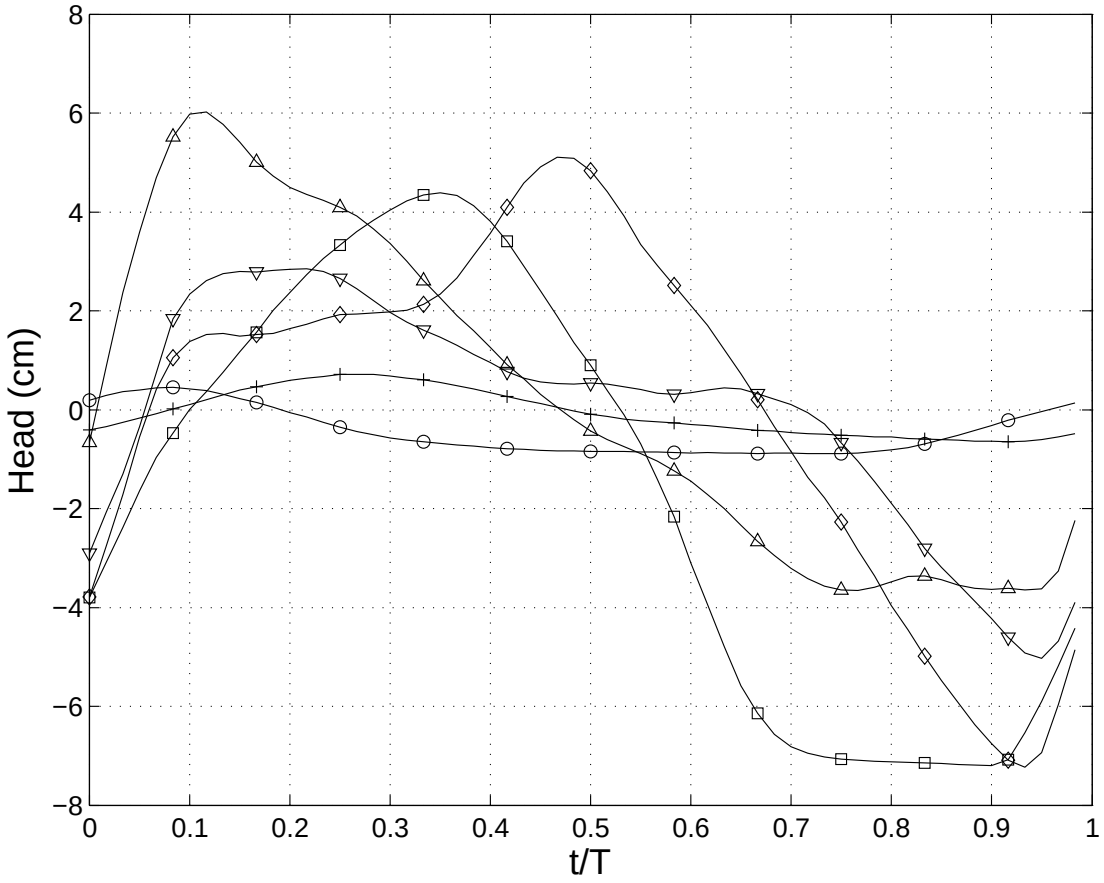

Figure 3.27: Run 21 phase averaged data at x = 80.4 ($\triangle$), 81.5 (+), 82.4 ($\bigtriangledown$), 83.4 ($\diamond$), 84.4 ($\square$), and 85.4 ($\circ$) m.

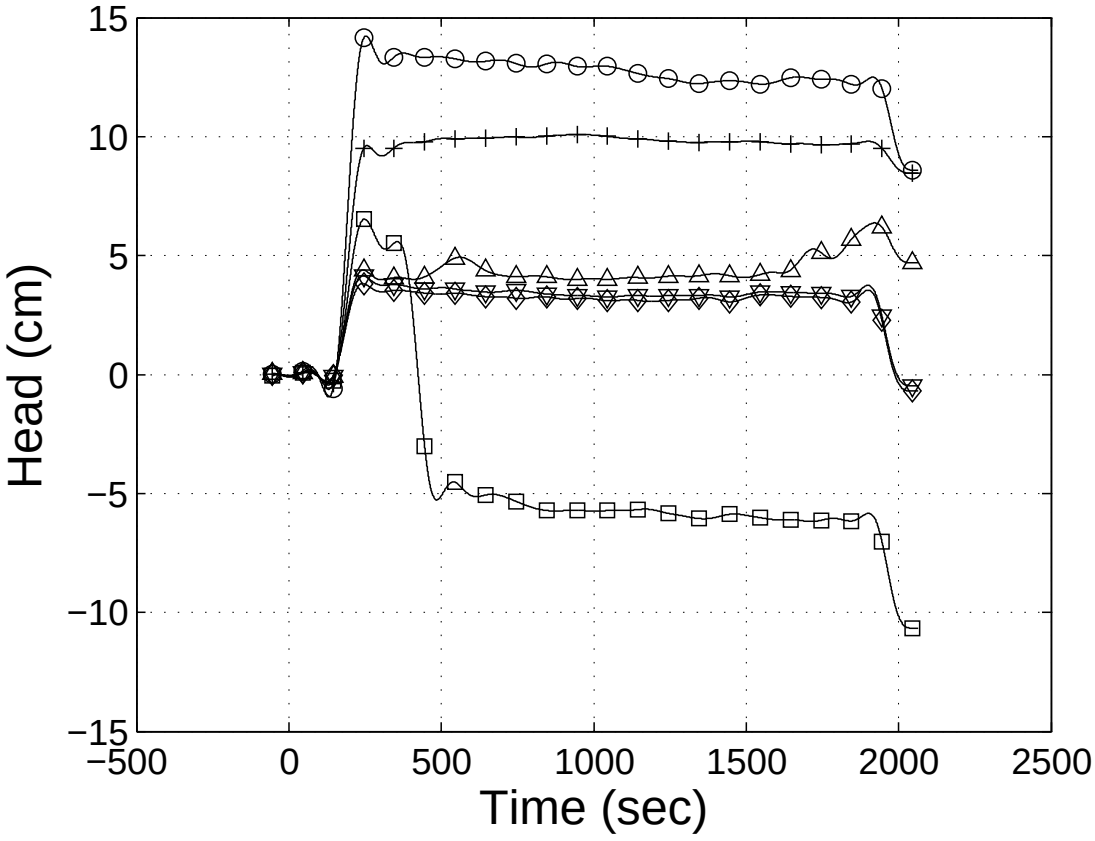

Figure 3.28: Run 21 Lowpass filtered data at $x = 80.4$ ($\triangle$), 81.5 ($+$), 82.4 ($\bigtriangledown$), 83.4 ($\diamond$), 84.4 ($\square$), and 85.4 ($\circ$) m. See text for a discussion of the drop in pressure at $t = 500$ s on the gage at $x = 83.4$ m.

difficult to measure with the ADCP. A turbulent decomposition based on phase mean velocities is possible, but provides little additional information and is not carried out. As wave height increases (particularly for larger random wave cases run by other groups), there is a strong likelihood of near bed turbulence and offshore transport which can be picked up in the backscatter signal reported by the ADCP.

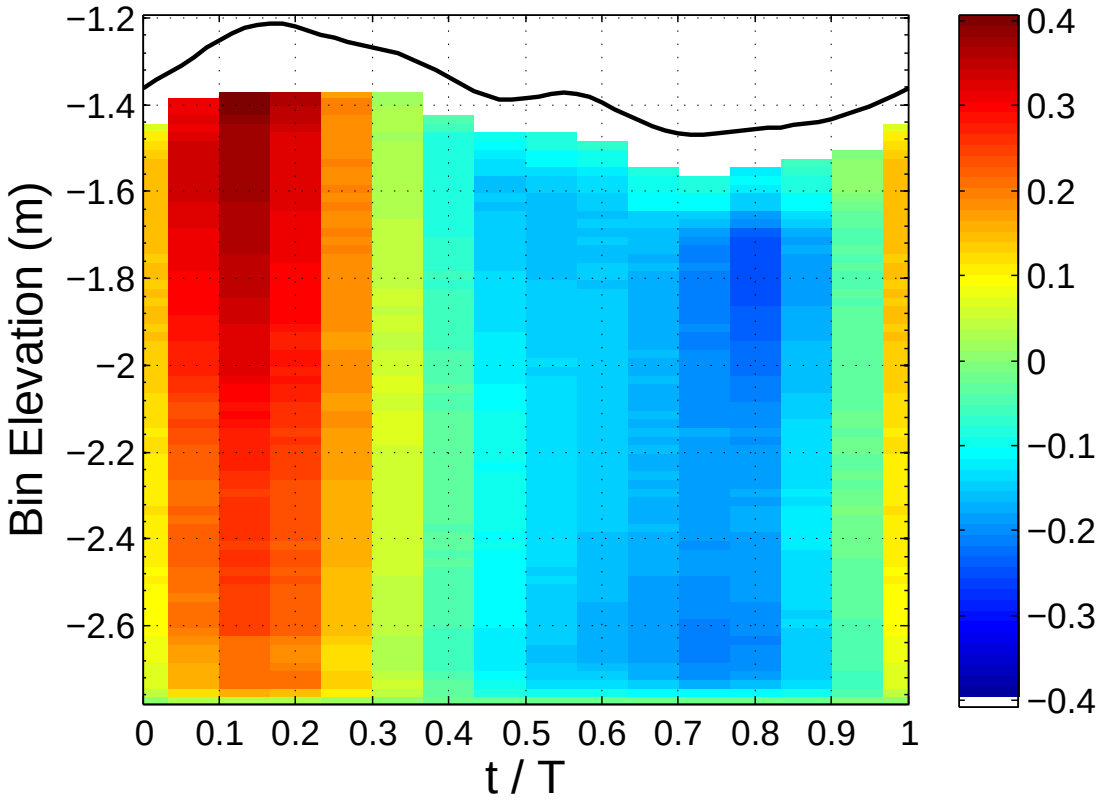

Figure 3.29: Run 6, Phase averaged velocity contour at the offshore location. The phase averaged free surface obtained from the Q45U is plotted as a solid line.

By taking the ensemble average of the phase profiles at the offshore boundary, the magnitude of the mean flow can be determined. The mean velocity profile for

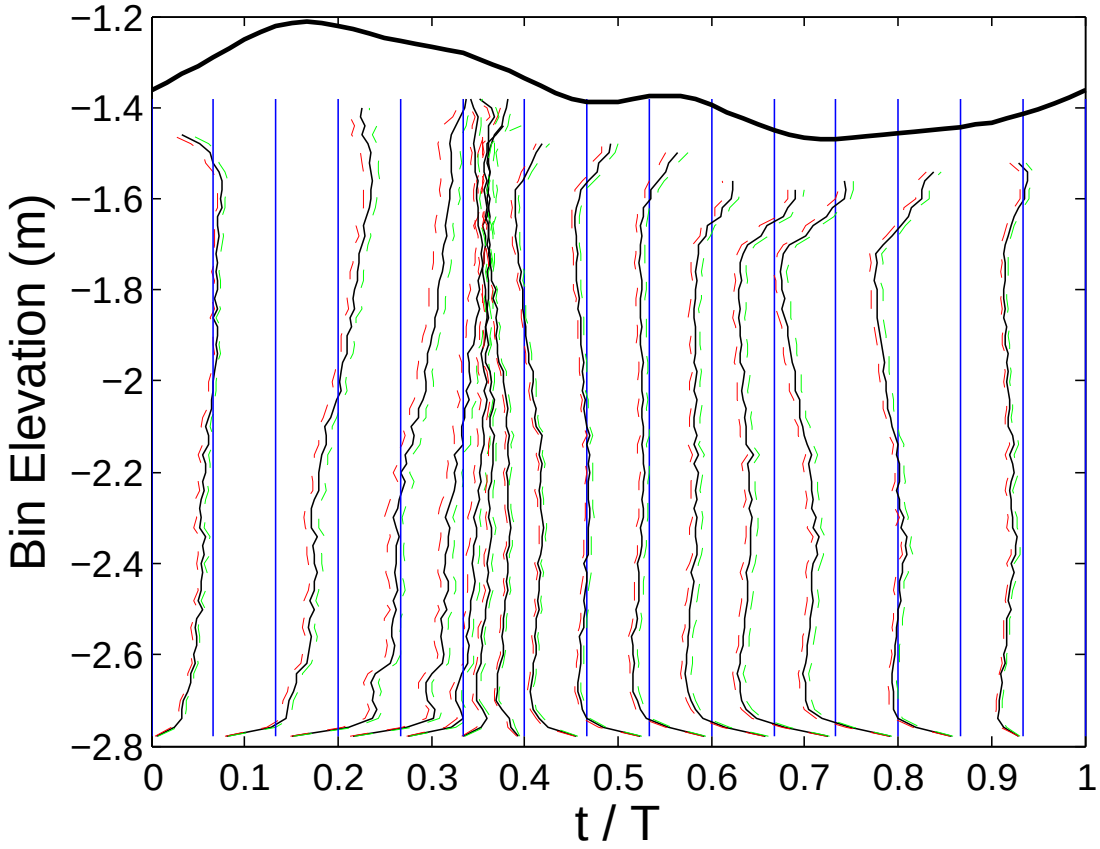

Figure 3.30: Run 6, Phase averaged velocity profile at the offshore location. The phase averaged free surface obtained from the Q45U is plotted as a solid line.

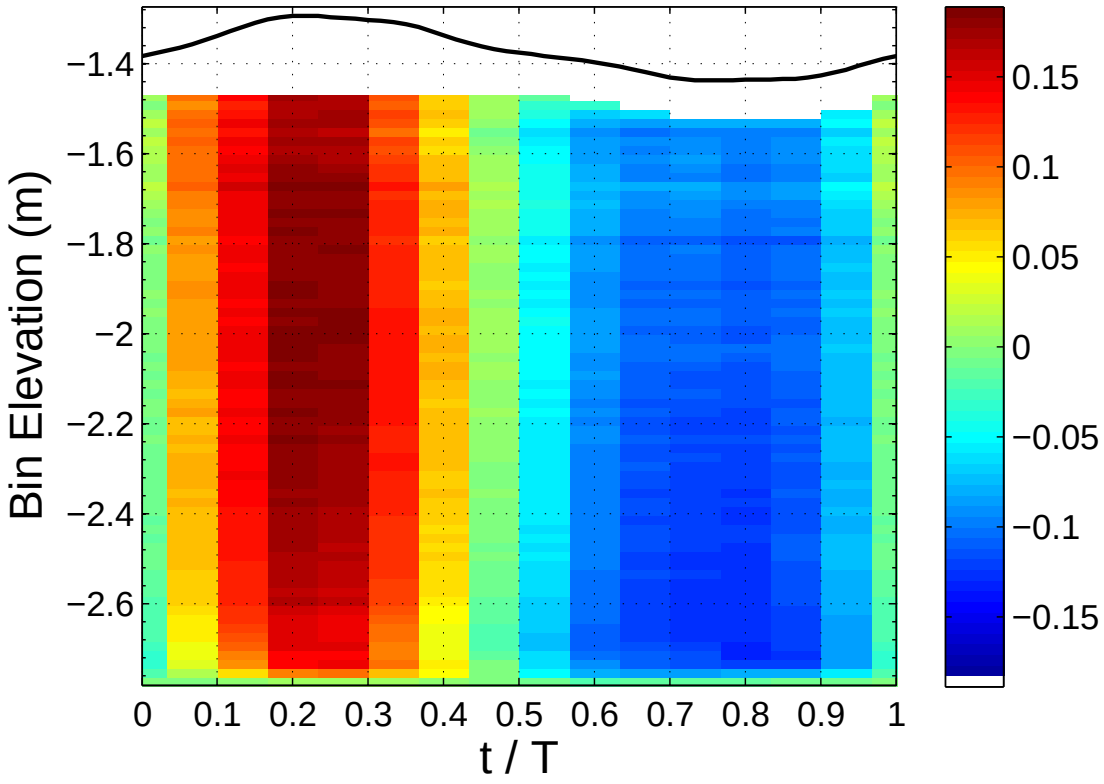

Figure 3.31: Run 16, Phase averaged velocity contour at the offshore location. The phase averaged free surface obtained from the Q45U is plotted as a solid line.

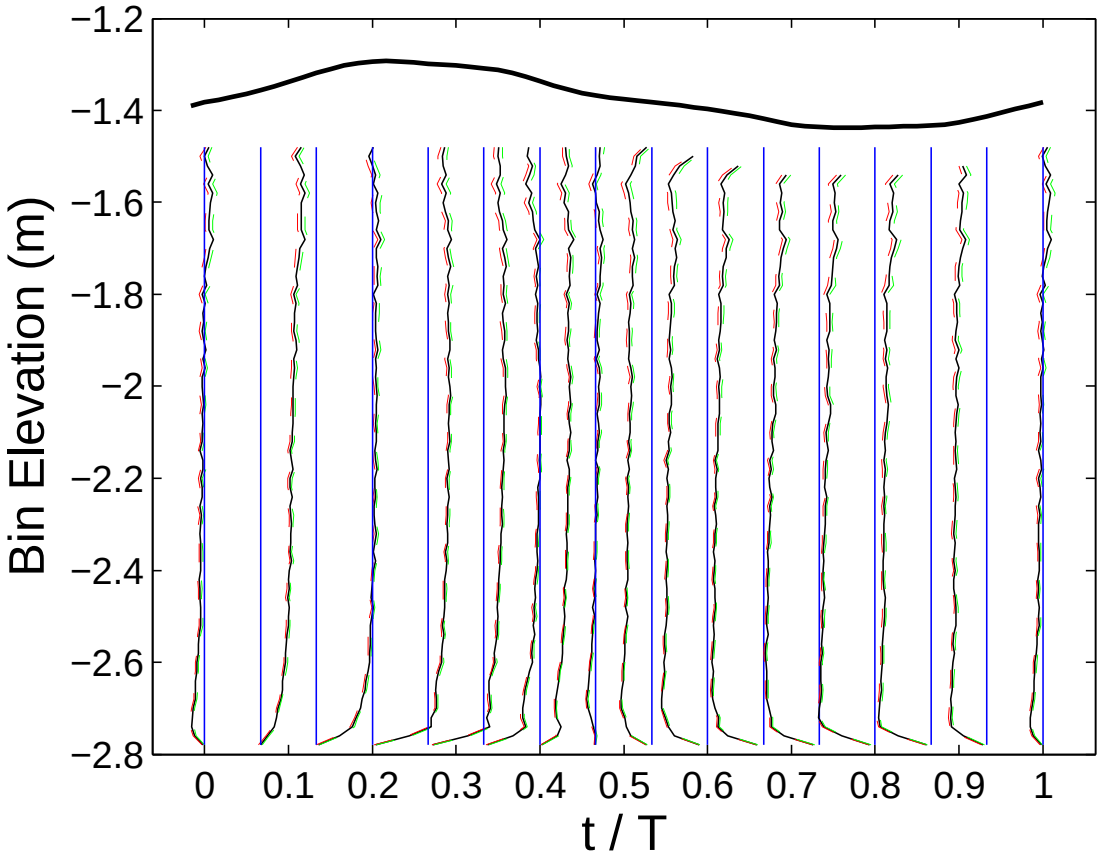

Figure 3.32: Run 16, Phase averaged velocity profile at the offshore location. The phase averaged free surface obtained from the Q45U is plotted as a solid line.

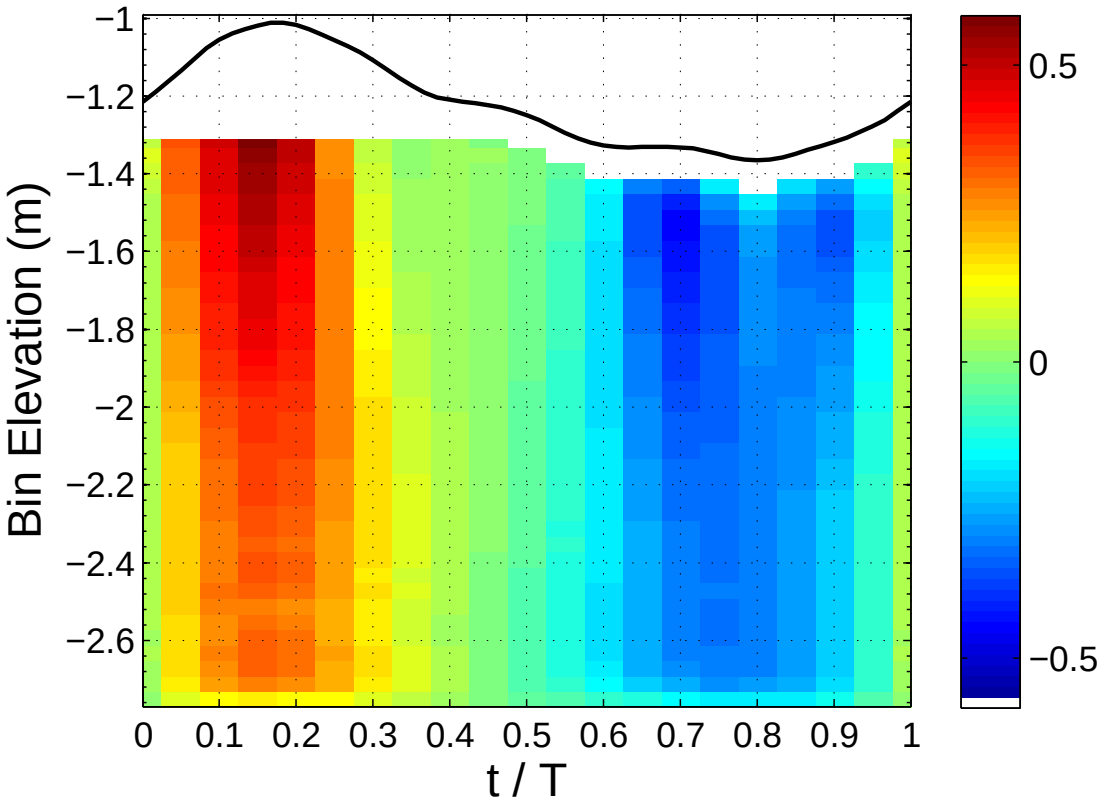

Figure 3.33: Run 21, Phase averaged velocity contour at the offshore location. The phase averaged free surface obtained from the Q45U is plotted as a solid line.

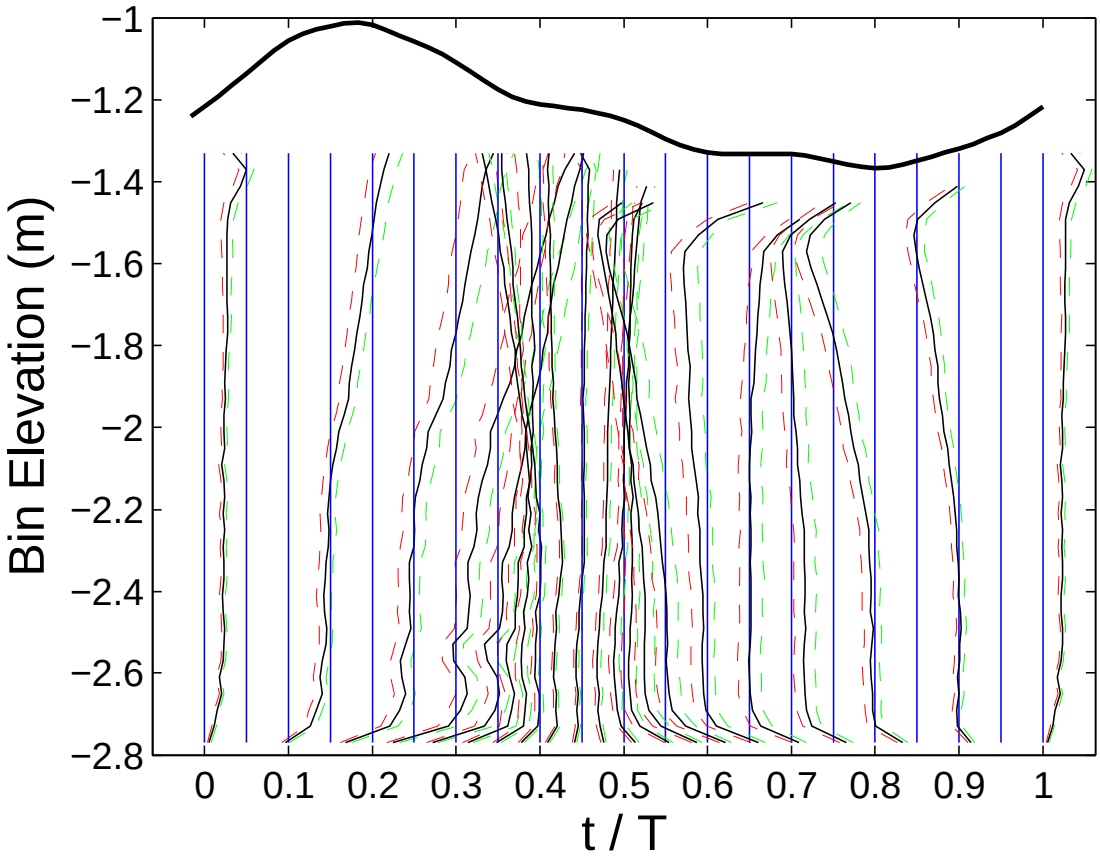

Figure 3.34: Run 21, Phase averaged velocity profile at the offshore location. The phase averaged free surface obtained from the Q45U is plotted as a solid line.

each run is presented in Figures 3.35 - 3.37 along with the integral of this profile. Each of the profiles shows a net offshore mass transport near the bed and near the surface a strong onshore flow as a result of conservation of mass. Runs 6 and 16 show a bulge near the bed of negative velocity, while the remainder of the profile is positive. In contrast, Run 21 is always negative, except near the surface, and actually exhibits much lower offshore transport then the two lower wave height cases.

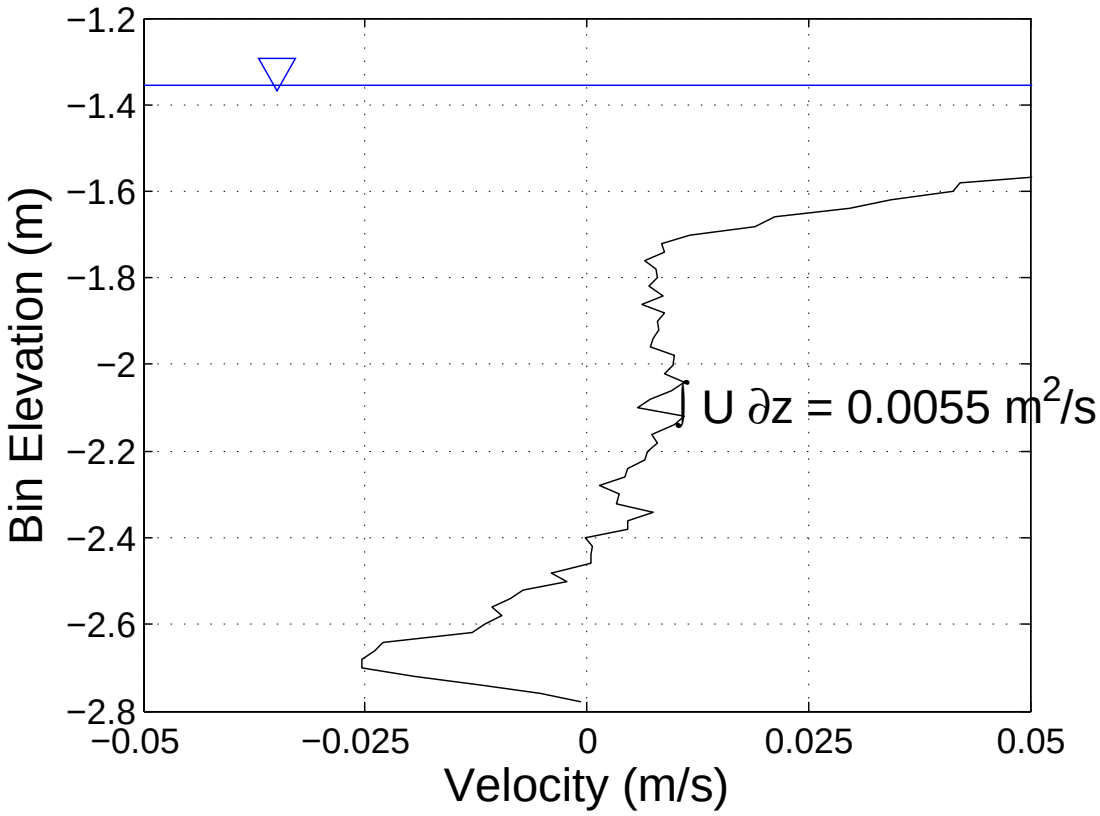

Figure 3.35: Run 6 mean velocity profile. Note the offshore flow in the bottom half meter of the profile and the onshore drift near the surface. There is bias near the surface due to surface return echo interference.

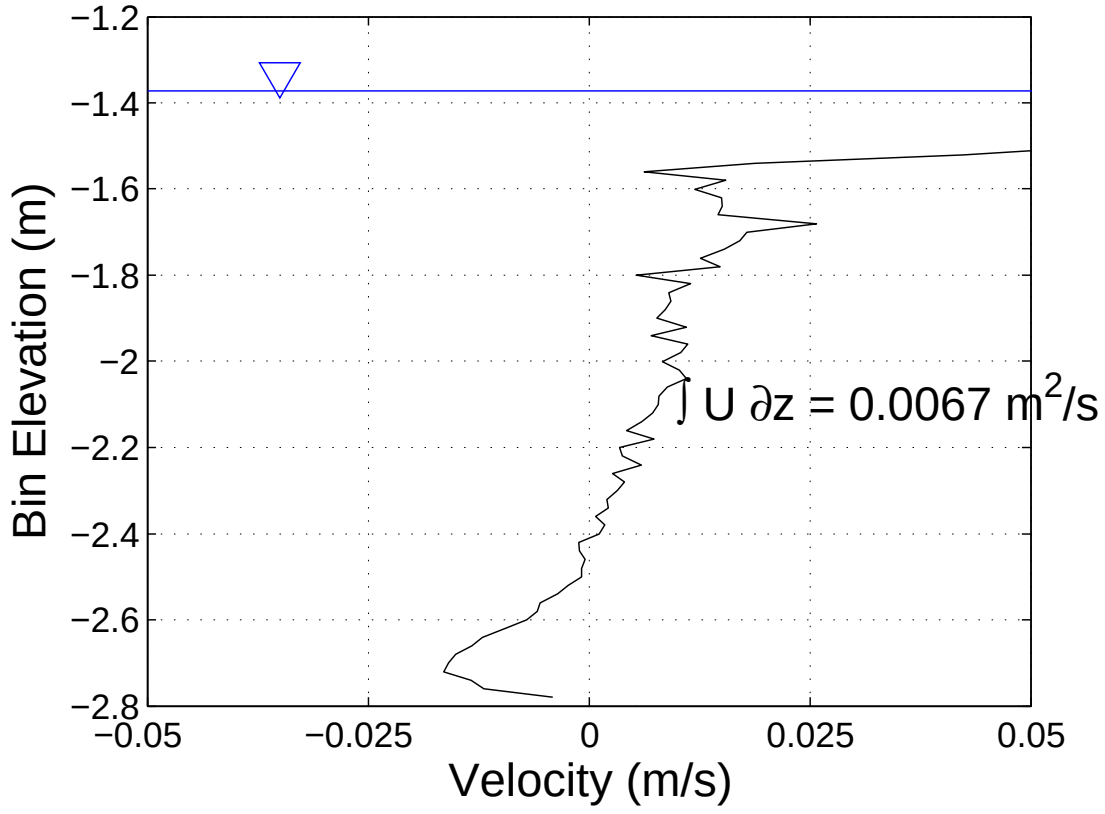

Figure 3.36: Run 16 mean velocity profile.

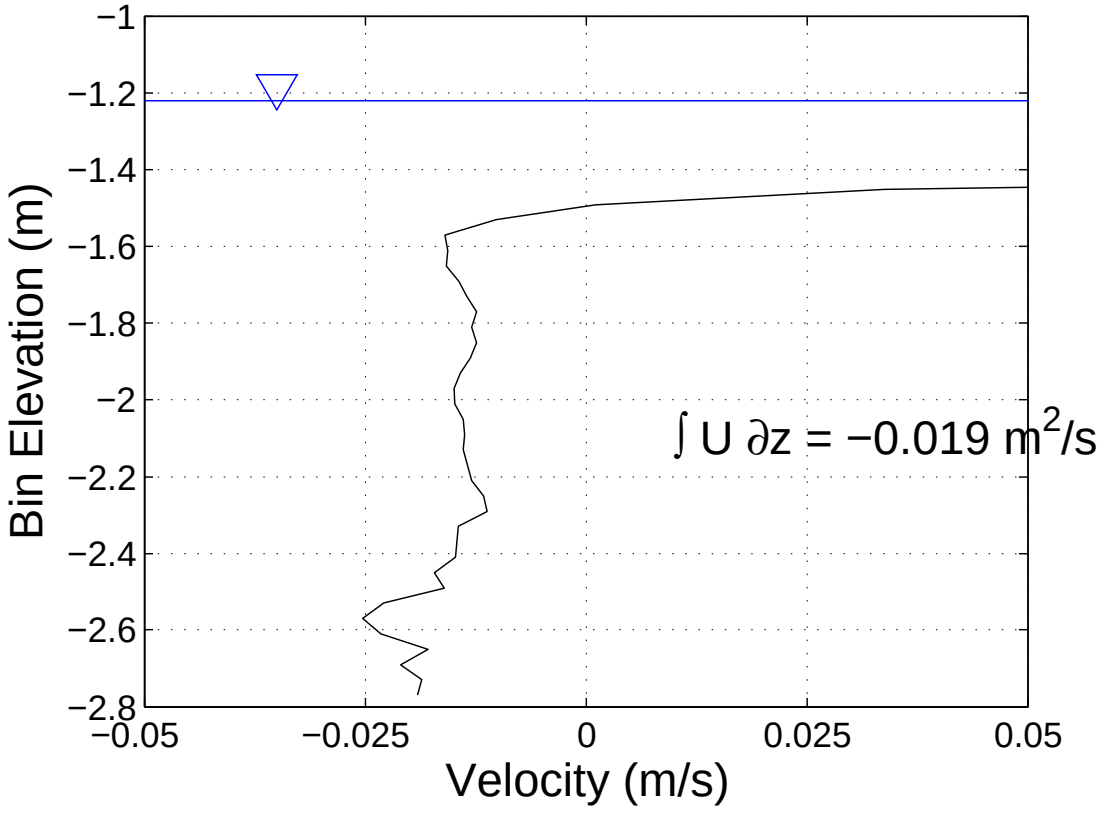

Figure 3.37: Run 21 mean velocity profile.

Chapter 4

Turbulence Characteristics

Many recent studies have detailed the turbulence characteristics in the inner surf zone for plunging and spilling breakers. The most recent and relevant to these experiments is the work done by Ting and Kirby (Ting and Kirby, 1996) (Ting and Kirby, 1995) (Ting and Kirby, 1994). Using a Laser Doppler Velocimeter, they made detailed measurements of mean and turbulent velocities under plunging and spilling waves over a fixed slope bed. Principal among their findings were the dependence of the turbulent dynamics on primarily the deep water wave condition and the beach slope, or put another way, on the breaking condition linked to the beach slope and deep water wave conditions via the surf similarity parameter ξ. Spilling waves were dominated by turbulence lasting several wave periods, while plunging waves saw a strong phase dependence in the turbulence. In plunging waves, turbulence is generated primarily by the passage of a turbulent bore associated with the wave crest generating grid turbulence, with turbulence dying off quickly to near zero levels before flow reversal. These are the conditions we expect to find in CROSSTEX surf zone where plunging waves have been produced.

4.1 Definitions

In 1895 Osborne Reynolds proposed the following decomposition of a velocity field $u(x, y, z, t)$ to simplify the analysis of turbulence analytically.

$$u(x, y, z, t) =< u(x, y, z, t) > +u'(x, y, z, t) \tag{4.1}$$

Where $< u(x, y, z, t) >$ represents the mean flow and $u'(x, y, z, t)$ represents a

fluctuation about the mean. The mean flow is easily measured in most cases since it constitutes a simple time average of the flow. The time dependence included in the above definition is often removed from the definition as the flow of interest is varying only slowly with time, i.e. the process being observed is stationary. In the case of a periodic flow this assumption will not hold unless the time scale over which the mean flow is calculated is sufficiently long to encompass many wave periods.

When dealing with a periodic or oscillatory flow as we are, the mean flow can be broken down further into a temporal mean and a periodic component.

$$< u(x,y,z,t) >= \overline{u(x,y,z,t)} + \tilde{u}(x,y,z,t) \tag{4.2}$$

Where $\overline{u(x,y,z,t)}$ is the portion of the mean flow that is constant and does not vary with time (the stationary portion of the flow) and $\tilde{u}(x,y,z,t)$ is the wave induced velocity. This second is essentially the phase average assuming weak time average flow (generally a valid assumption given order of magnitude analysis) and will generally be the only term used to compute the Reynolds decomposition.

Since the mean flow $\overline{u(x,y,z,t)}$ is induced by the wave field, creating a return flow near the bed (undertow) and an onshore transport near the surface, using phase averaging techniques it is possible to compute the quantity $< u(x,y,z,t) >$ from a time series, and estimate the turbulent fluctuations as

$$u' = u - < u >^{PA} \tag{4.3}$$

Where $< u >^{PA}$ is the phase averaged velocity as defined in equation 3.5. There are several problems with defining turbulence in this manner which can cause unwanted errors in turbulence analysis. As seen in Figure 4.1, the phase

average, even though computed over 60 phase bins in this case, still suffers from variations in the arrival of the wave crest (the gradual slope of the phase average versus the sharp rise of the instantaneous velocity). This biases the turbulent fluctuations high at this point in the phase, even though a comparison of the rest of the phase shows good agreement between the two signals in terms of shape. This technique has been used successfully in many prior studies (Ting and Kirby, 1994) (Cowen et al., 2003) and provides good results despite the bias at the bore front. A better method has recently been developed which provides an easier means to remove wave energy, however.

4.1.1 Shaw and Trowbridge Differencing Technique

Trowbridge (1998) proposed an alternative method to estimate the turbulent fluctuations by differencing the measurements between a pair of sensors. The critical assumption involved in his method was the wave motions at the two sensors were perfectly correlated, but the turbulence was entirely uncorrelated. This strict requirement limits his method to pairs of vertical sensors separated by a distance larger than the length scale of the largest eddies but smaller then the wavelength of the waves.

A modification of Trowbridge's method was developed by Shaw and Trowbridge (2001) involving a relaxed assumption of only coherence between the wave induced velocity at the two locations while the turbulence is again uncorrelated. This relaxed assumption is made possible by using a linear filter to predict the wave induced signal (i.e. non-turbulent, low-frequency motion) at one location from the signal at the second. Prediction of one signal from the other is done via linear filtering, with filter weights determined via least squares solution of a transversal

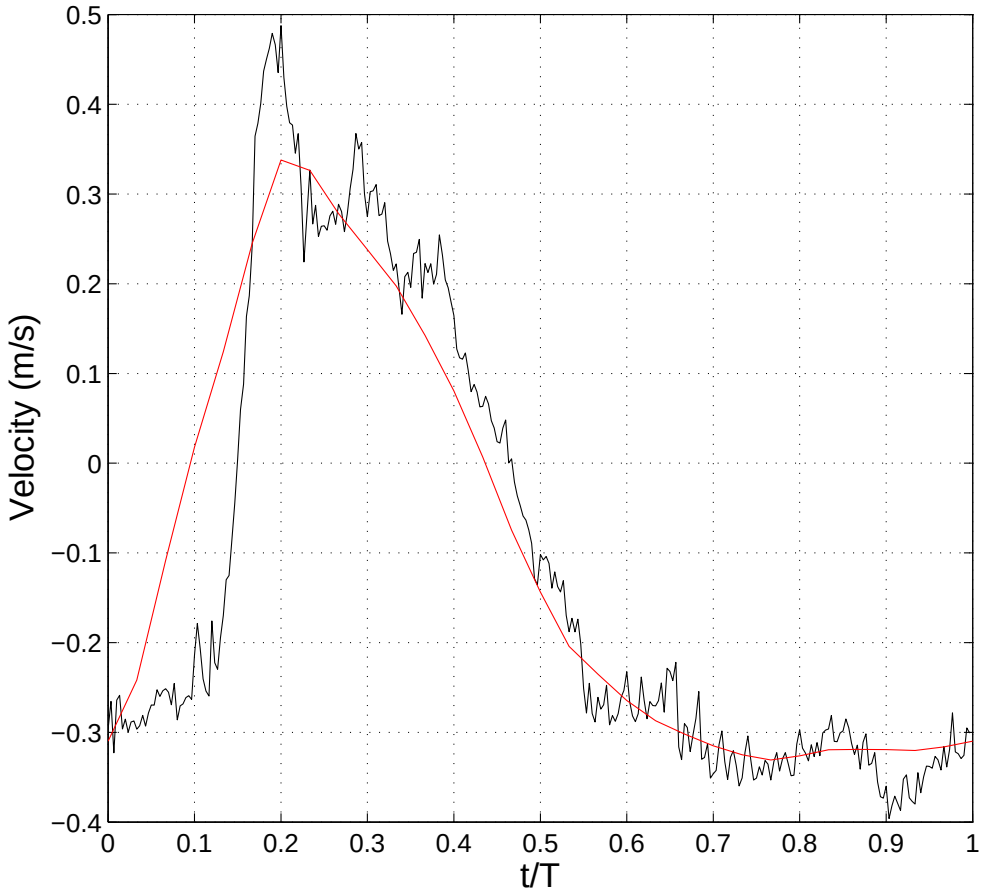

Figure 4.1: Example of ADV instantaneous velocity and phase averaged velocity for defining the turbulent fluctuation $u\prime$.

filter. Full details of the method and filter calculation are available in Shaw and Trowbridge (2001).

This method makes it possible to use two sensors separated by a horizontal or vertical distance (or both) to directly estimate the instantaneous wave induced velocities and then determine the turbulent velocities by differencing. The main requirements are similar to before, the separation distance be larger than the length scale of the largest turbulent eddies but shorter then the wave length of the waves. Using Shaw's method, we can now define the turbulent velocity component as

$$u' = u - \hat{u} \tag{4.4}$$

Where $\hat{u}$ is the filtered velocity signal containing both the time average mean flow and the instantaneous wave induced velocity. An example of $\hat{u}$ is shown in Figure 4.2.

For the LWF, Scott et al. (2004) showed Trowbridge (1998) differencing method produces results comparable to the phase decomposition method throughout the water column. Because of the ease of implementing the Shaw and Trowbridge (2001) modification to this method and the reduction in bias at the bore front, turbulent fluctuations will be calculated by differencing the instantaneous and filtered velocities rather than a phase decomposition. A comparison of spectra before and after the filtering and differencing process is presented in Figure 4.3. The reduction of wave energy at the driving frequency and the higher harmonics can be clearly seen.

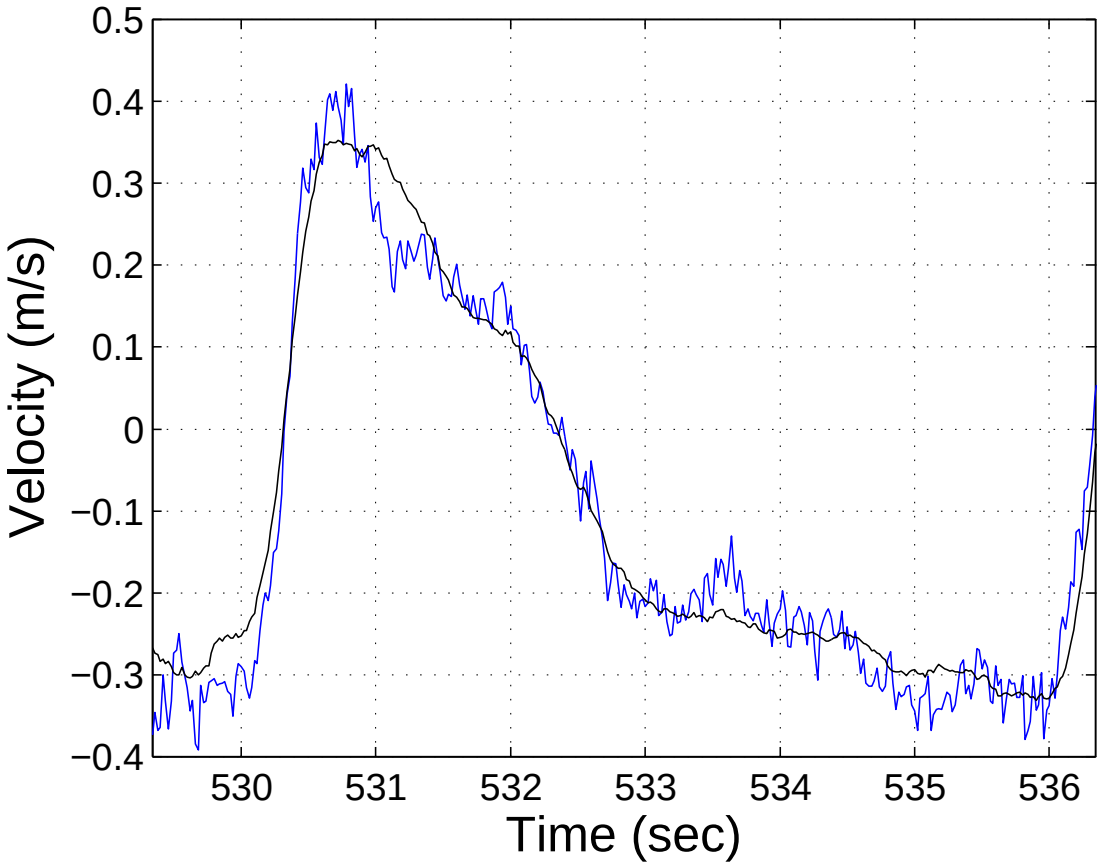

Figure 4.2: Example instantaneous and filtered velocities computed using the linear filtration method detailed in Shaw and Trowbridge (2001).

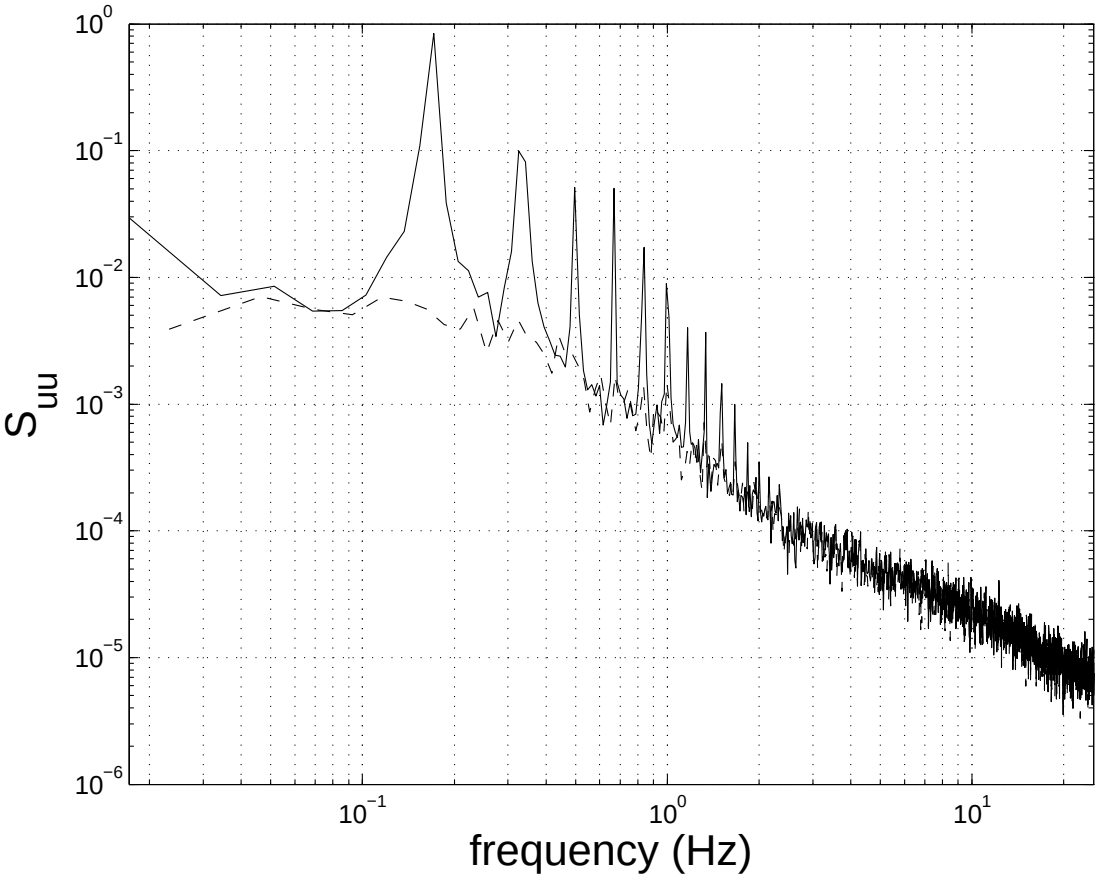

Figure 4.3: Example of the reduction in wave energy accomplished using the Shaw and Trowbridge (2001) filtering technique. The solid line is the original record after cleaning, but without any decomposition. The dashed line is the same record after being differenced using the Shaw and Trowbridge (2001) technique. The driving frequency of the waves has been almost completely removed, and only the higher harmonics retain any appreciable energy.

4.2 Turbulent Quantities

Ting and Kirby's work in the mid-1990's on turbulence underneath spilling and plunging waves is still considered the standard reference on the subject. Their motivation for studying the detailed workings of turbulence and attempting to apply turbulence theory to their measurements was the need to understand the spatial and temporal distribution of Turbulent Kinetic Energy (TKE or k) and how it might affect sediment transport and sediment transport modeling. TKE is defined by Pope (2000) as

$$k = \frac{1}{2} < u_i' u_i' > \tag{4.5}$$

Turbulent kinetic energy represents the mean kinetic energy per unit mass in the fluctuating velocity field. Turbulent intensities are the quantity $u'u'$ in Eq. 4.5 and are a measure of the energy contained in each turbulent component. Tennekes and Lumley (1972) provided a form of the turbulent energy balance, often called the k-equation, which represents the balance between advection, diffusion and dissipation of turbulent energy, modified here to examine k in a phase averaged (<>) sense.

$$\frac{\partial k}{\partial t} + \frac{\partial < u_j > k}{\partial x_j} = -\frac{\partial}{\partial x_j}\left(\frac{1}{\rho} < u_j' p' > + < u_j' k' >\right) - < u_i' u_j' > S_{ij} - 2\nu < s_{ij} s_{ij} > \tag{4.6}$$

The first two terms of 4.6 represent the time rate of change and spatial variation in the advection of k. The third term (first on the RHS) represents the spatial variation of dynamic pressure and the turbulent transport of k, while the fourth and fifth terms represent turbulent production and dissipation respectively.

With the ADVs deployed in the surf zone, we can estimate the advection, production, and also $\frac{\partial k}{\partial t}$ terms. Rough values of dissipation can also be estimated, but given prior studies inability to accurately measure this quantity with higher precision instruments in more forgiving conditions, only a brief examination of dissipation will be considered. The pressure term requires measurement of the dynamic pressure and is not considered presently.

Another quantity often calculated in turbulence studies are Reynolds stresses. Reynolds stresses are a result of the Reynolds decomposition process (eqn. 4.1) being applied to the terms in the Navier-Stokes equations, which are then averaged. The resulting set of equations, referred to as the Reynolds Averaged Navier-Stokes equations, describe the mean properties of the flow, but also contain 6 new terms containing products of turbulent fluctuations. These terms, referred to as Reynolds stresses, are written in tensor notation as

$$R_{ij} = \rho\overline{u_i' u_j'} \tag{4.7}$$

Of primary interest to the current flow is the Reynolds stress corresponding to $i = 1, j = 3(\overline{u'w'})$. The exact interpretation of a Reynolds stress as a physical quantity is still open to debate, but can be regarded for our purposes as the the turbulent transport of horizontal momentum ($\rho u'$) by vertical fluctuations (w'). The first term represents some quantity (in this case when multiplied by ρ, momentum) being advected by the second term.

The specific Reynolds stress we are interested in ($u'w'$) can be regarded as a surrogate for the bed shear stress and responsible for resuspending sediment into the water column which is then advected away from the bed by the vertical velocity fluctuations and transported shoreward by the mean flow.

4.3 Turbulence in the Outer Surf Zone

The 8 ADVs deployed on the cart generally provide 5 usable estimates of turbulent fluctuations. Some ADVs are rendered useless for turbulence estimates because of long temporal dropouts caused by low correlations or the ADV head coming out of the water. Filtered velocities were calculated from sensor pairs deployed in the same along shore location and separated vertically. When a vertical pair was unavailable, a horizontal pair comprising two separate along shore locations was used. The successful removal of wave energy can be judged by the spectra presented for each location, where the driving wave frequency is marked by a vertical bar. Phase averaged cross shore (u), along shore (v), and vertical (w) velocities and turbulent fluctuations, k, and return signal strength for each run are presented in the following sections. Plots are ordered from the lowest sensor to the highest.

Defining the position of the ADV above the bed is extremely difficult and the distance to the bed quoted for each ADV was measured prior to any waves being run. Problems with some distance measurements, taken automatically by the ADV prior to data collection, because of low signal quality meant some distances were estimated from measured sensor spacing and a trusted distance measurement. Because the bed is mobile, the distances obtained can not be regarded as anything other then an approximate value only applicable to the earliest waves. Figure 4.4 shows the bathymetry directly below the cart ADVs at the start of Run 6 (similar plots are presented for each run in later sections). There is a very strong variation in bed elevation in the along shore direction, with the net change O(10 cm). Assuming this along shore variation extends several meters in the cross shore direction, from one side of the tank to the other we can calculate a ratio of breaking wave height to water depth for each side as discussed in §3.7. Looking offshore,

the left hand side (higher bed elevation) yields $\gamma_L \approx 0.5$ with wave height $H = 10$ cm. On the right hand side (lower bed elevation), $\gamma_R \approx 0.3$. both values are low for a plunging breaker compared to what Ting and Kirby (1994) found ($\gamma = 0.8$ in the surf zone). The left hand side yields a value of γ comparable to their value for a spilling breaker. Given the striking contrasts they found between the turbulence structure in spilling and plunging waves and their prediction of a gradual transition between the two regimes, it is difficult to say exactly what form the turbulence at the cart should take or even if results will be consistent across the tank.

While at the offshore station there was little difference between the two sides of the tank, once the wave has broken, the tank no longer behaves as an ideal two dimensional system. bathymetry, along shore velocities and wave reflection off of the tank walls all create a very complex system where cross shore transport of sediment is contaminated with along shore transport.

4.3.1 Run 6

For ADV00 located at the lowest elevation on the center wing, phase averaged velocity, turbulent intensity, k, and return signal strength averaged across all four receive beams is presented in Figure 4.5. The phase averaged cross shore velocity (U) shows higher magnitudes than at higher elevations, while the negative phase averaged velocities are unusual this close to the bed (0.007 m) and either indicate velocity biasing due to sediment fall velocities or more likely, the local bathymetry permits a negative vertical velocity due to along shore change. Once the bore front has passed, the along shore velocity (V) becomes strongly positive (flow from right to left in Figure 4.4) which could account for the along shore bathymetry variations. Any sediment resuspended during the passing of the borefront would

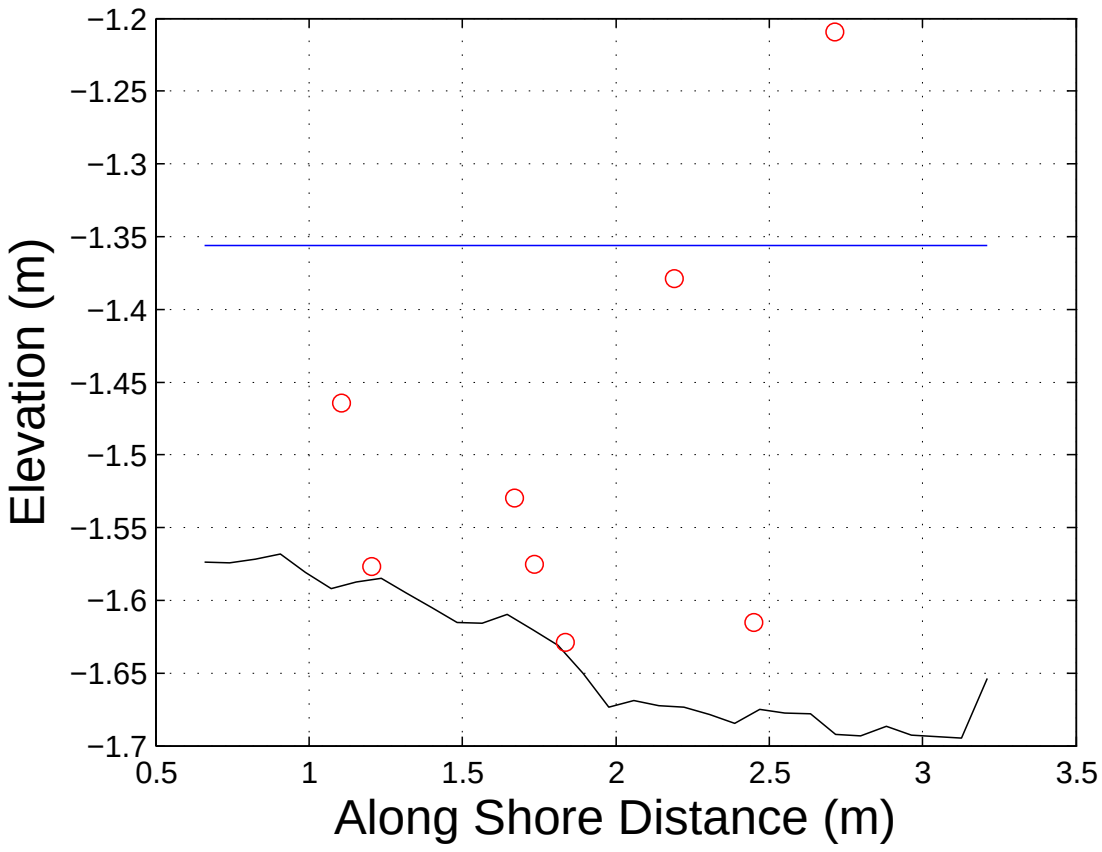

Figure 4.4: Run 6 bathymetry below the cart ADVs at the start of the run looking offshore (same orientation as Figure 2.4). The solid flat line represents the SWL. ADVs are marked with ∘, and the distances shown are nominally those taken by the ADV at the start of data collection.

be advected onshore and to the left when looking offshore.

Examining the various turbulent quantities at this elevation, the lag between the peak cross shore velocity and the peak in associated turbulence intensity and k is slightly surprising. There is some finite time needed for turbulence generated by the surface roller to mix down to the bed. Ting and Kirby (1995) estimate this time as the equivalent of the time it takes a scalar to mix across a river. After scaling and substitution for appropriate scales, their dimensionless vertical mixing time $\frac{t}{T}$ is

$$\frac{t}{T} = \frac{2(h/\lambda)}{(H/h)} = \frac{2(h/\lambda)}{\gamma} \tag{4.8}$$

Where H is the local wave height, h is the local water depth, and λ is the local wavelength. Substituting appropriate values for the various length scales near the cart at wave gage 11 (emphx = 71.2 m) into equation 4.8, $\frac{t}{T} = 0.18$. This is significantly longer then the value Ting and Kirby found for their plunging breaker, but close to the lag between the onshore velocity peak and the turbulent intensity peak.

It is possible at this wave height ($H = 20$ cm) we are dealing with a weakly plunging wave, placing the turbulence dynamics in the transition region between spilling and plunging . While turbulence is not confined to the surface as in a spilling breaker and there does seem to be some consistency in turbulence intensity throughout the water column, the obvious and consistent lag between arrival of the bore front and evidence of turbulence near the bed is not consistent with a true plunging breaker where mixing is expected to occur almost instantaneously.

ADV03 located on the left wing looking offshore (Figure 4.6) however does not show evidence of this lag or high turbulence levels. It is approximately the

same distance above the bed as ADV00 on the center wing, yet has a distinctly different velocity and turbulence signal. Given evidence of along shore transport of sediment towards ADV03, and it's initial position only millimeters above the bed, it is almost certain the sample volume of the ADV has extended into the bed and instead of measuring water velocity, we are measuring some combination of water and sediment velocity. While it is intriguing to think of the possibility of using the ADV to measure sediment velocity, it is impossible to say what combination of sediment and water is being measured, or where in the flow this measurment is being made, making interpretation extermemely difficult.

The earliest use of acoustic instruments in oceanography was as simple ranging instruments to find distance to a hard target like the bottom. Gradually, instrumentation improved and the ability to look at the return echo as an indicator of variations in density, water temperature and other quantities which affect the speed of sound has improved. Since the ADV (and ADCP, although it proves less useful in this role in the LWF) is essentially a simple echo sounder with higher level processing capabilities to extract velocity information, it is possible to use the return echo to infer something about the physical characteristics of the flow.

The last panel in Figures 4.5 - 4.10 is the phase averaged return signal amplitude. It is possible to calibrate this return echo to a known sediment concentration similar to the manner in which optical back scatter instruments are calibrated. With the co-located OBS sensors on the cart wings, a rough calibration could also be performed to estimate sediment concentration. Without calibration, though, insight into the time scale of sediment resuspension and turbulent transport can still be gained.

In general we see an increase in return signal amplitude with the passage of

the bore front. This can be due to two different mechanisms. As the wave breaks, it entrains air generating bubbles which are carried downwards by the plunging jet. These will be seen by the ADV as a stronger return echo signal because of the reflection caused by the air/water interface. Another possible reason for increased return signal strength is the presence of more scatterers in the water column (i.e. sediment being resuspended). It may be possible to estimate the size of the scatterers with some processing of the return signal, allowing a rough determination of what the dominant mechanism driving the increase in signal amplitude is.

For now, it is encouraging to see an increase in return signal strength corresponding to the increases in turbulent intensity. At the lowest sensor, ADV00, the increase precedes the increase in cross shore turbulent intensity, so it is very likely sediment is being resuspended off the bottom due to the increased cross shore velocity.

Figure 4.11 shows the cross shore velocity component U with all usable ADVs plotted on the same axes. A similar plot, Figure 4.12, exists for the vertical velocity. For this and all other runs examined the net temporal transport is offshore at all elevations.

4.3.2 Run 16

Owing to the smaller variation in bathymetry in the along shore direction (Figure 4.15), there seems to be less along shore transport during this run. There is still some net transport as the bathymetry changes by several centimeters underneath the cart ADVs over the course of the run (dashed line). Measurement locations are higher above the bed so velocities should be uncontaminated with potential

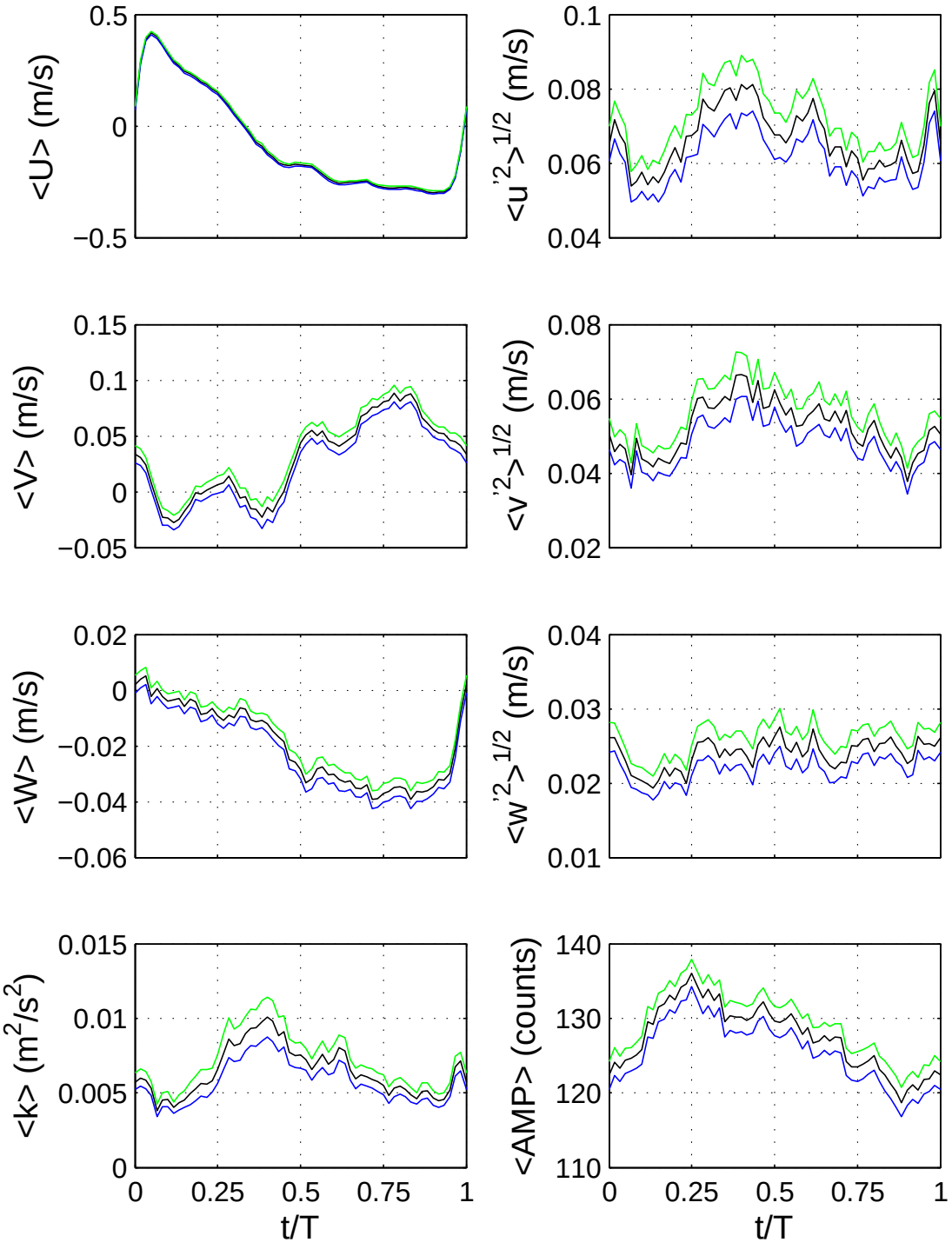

Figure 4.5: Run 6 Cart ADV00 phase averaged velocities, turbulent intensities, turbulent kinetic energy, and return signal amplitude at 0.007 m above the bed, center wing.

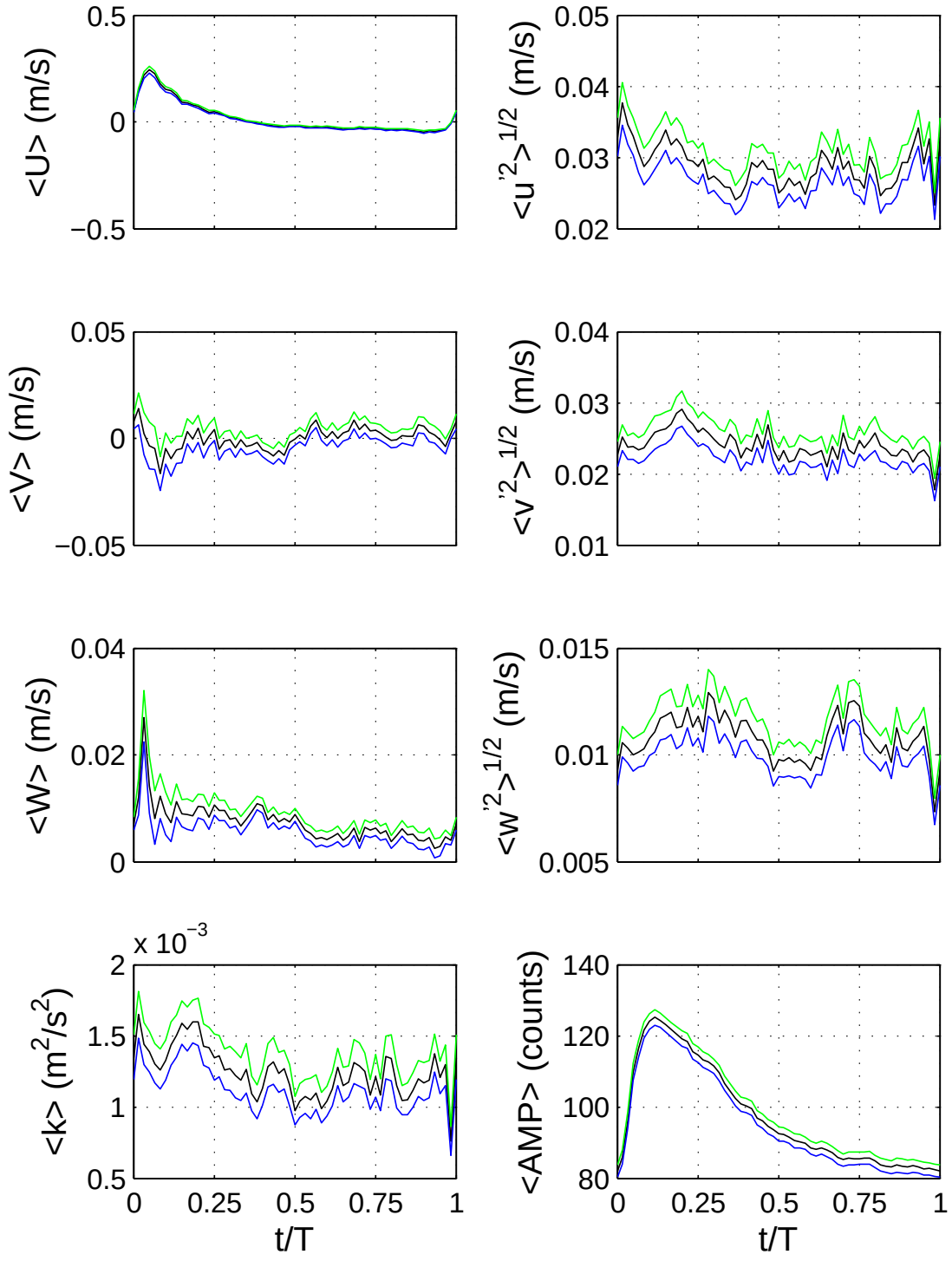

Figure 4.6: Run 6 Cart ADV03 phase averaged velocities, turbulent intensities, turbulent kinetic energy, and return signal amplitude at 0.009 m above the bed, left wing.

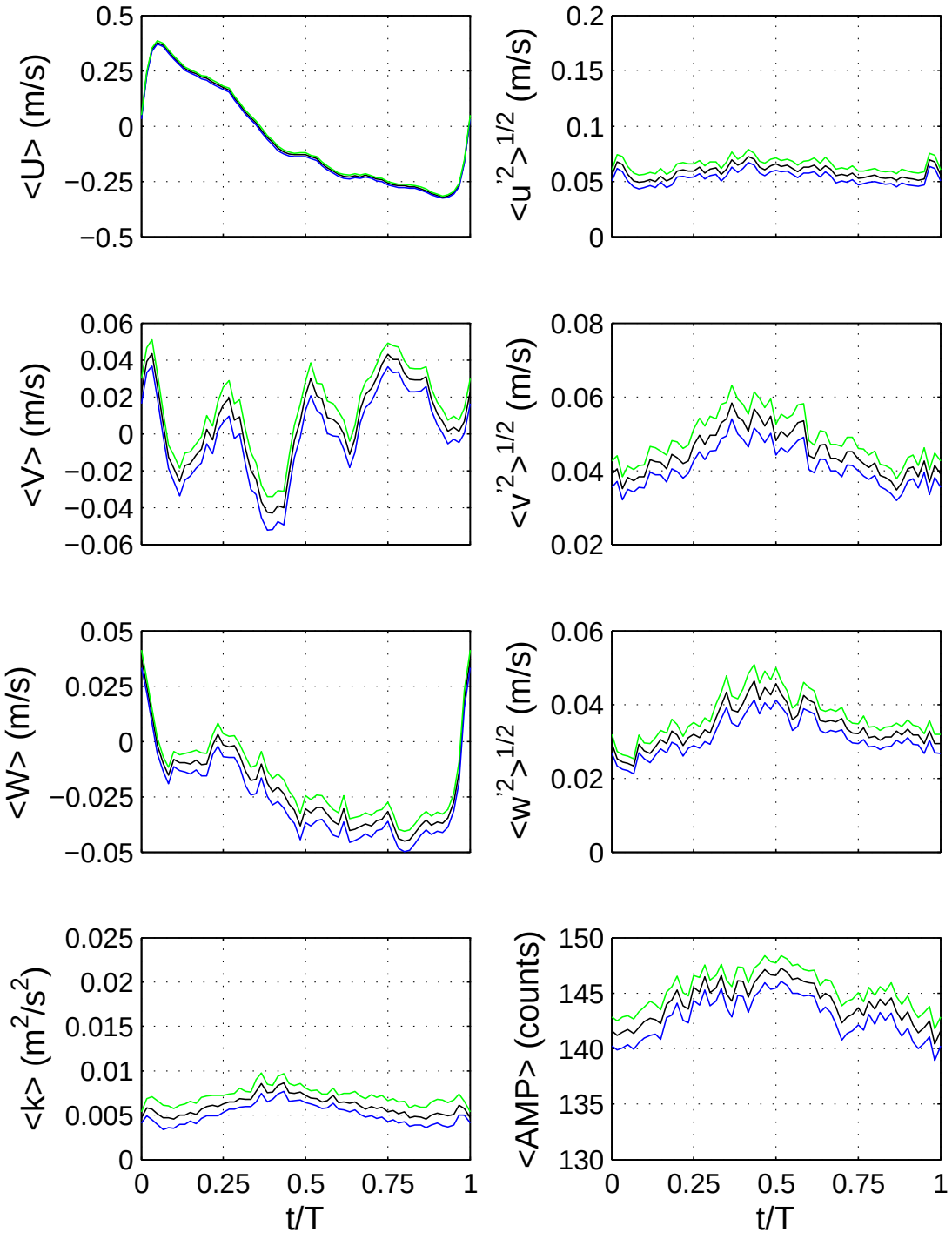

Figure 4.7: Run 6 Cart ADV07 phase averaged velocities, turbulent intensities, turbulent kinetic energy, and return signal amplitude at 0.046 m above the bed, center wing.

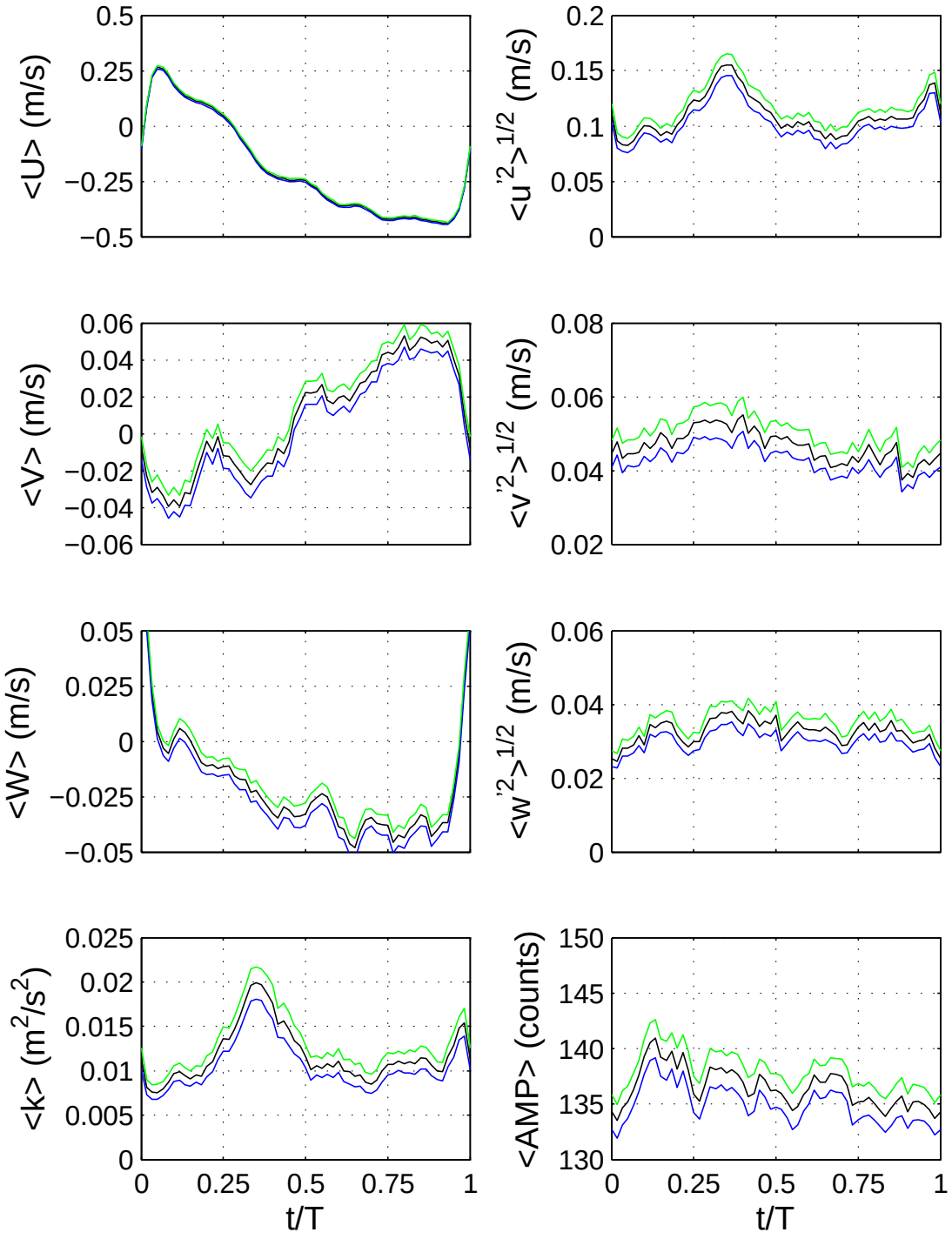

Figure 4.8: Run 6 Cart ADV01 phase averaged velocities, turbulent intensities, turbulent kinetic energy, and return signal amplitude at 0.062 m above the bed, right wing.

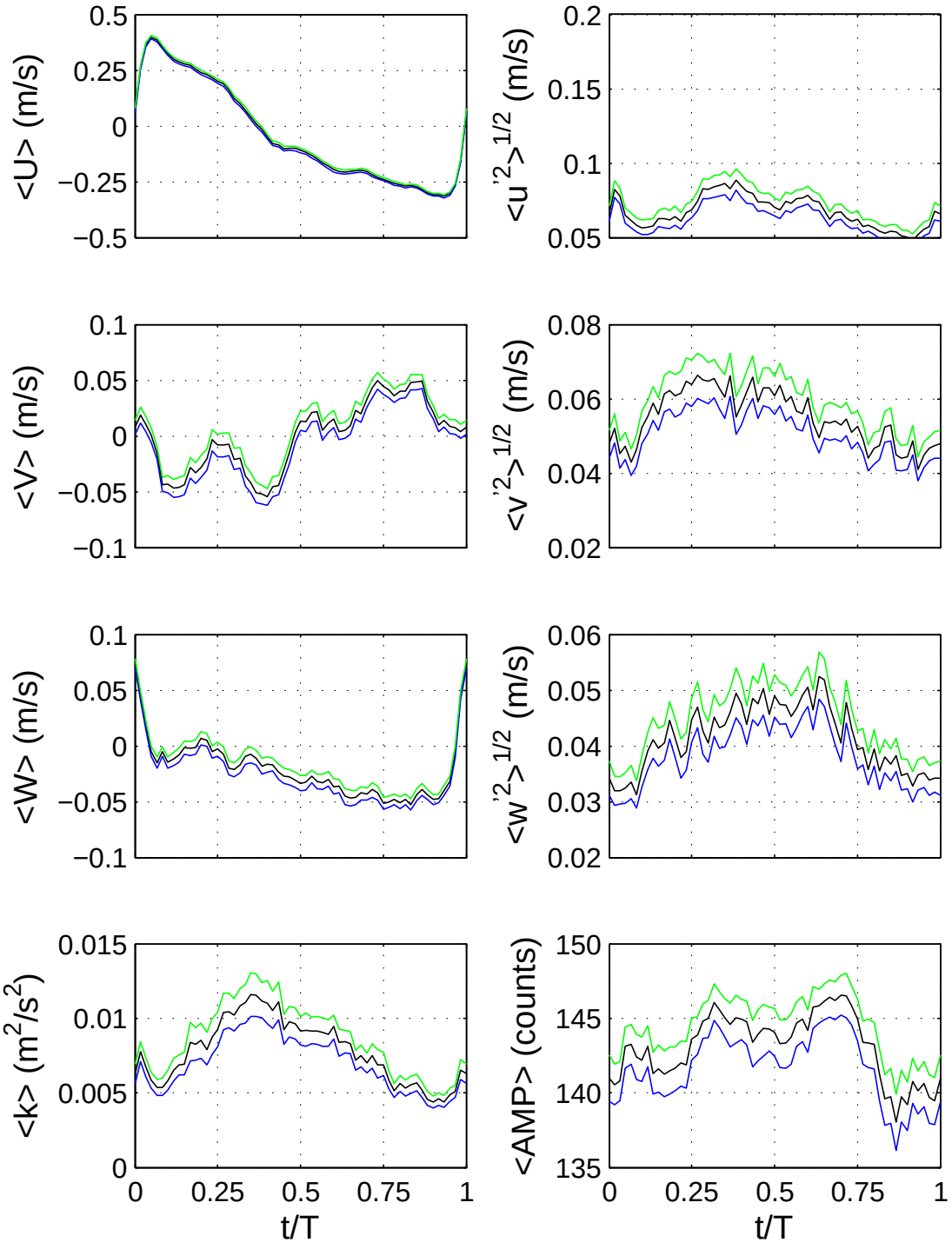

Figure 4.9: Run 6 Cart ADV02 phase averaged velocities, turbulent intensities, turbulent kinetic energy, and return signal amplitude at 0.08 m above the bed, center wing.

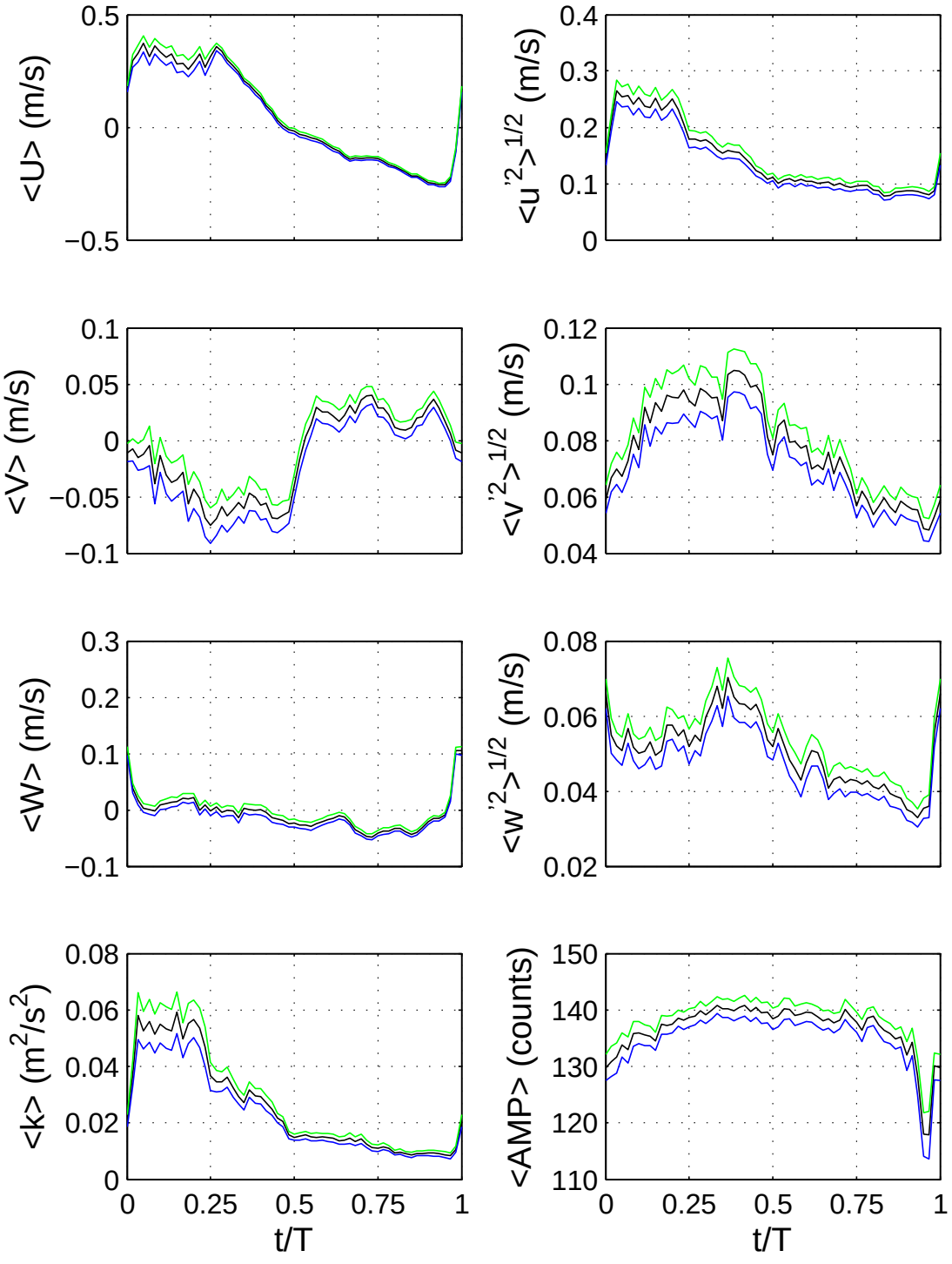

Figure 4.10: Run 6 Cart ADV05 phase averaged velocities, turbulent intensities, turbulent kinetic energy, and return signal amplitude at 0.125 m above the bed, left wing.

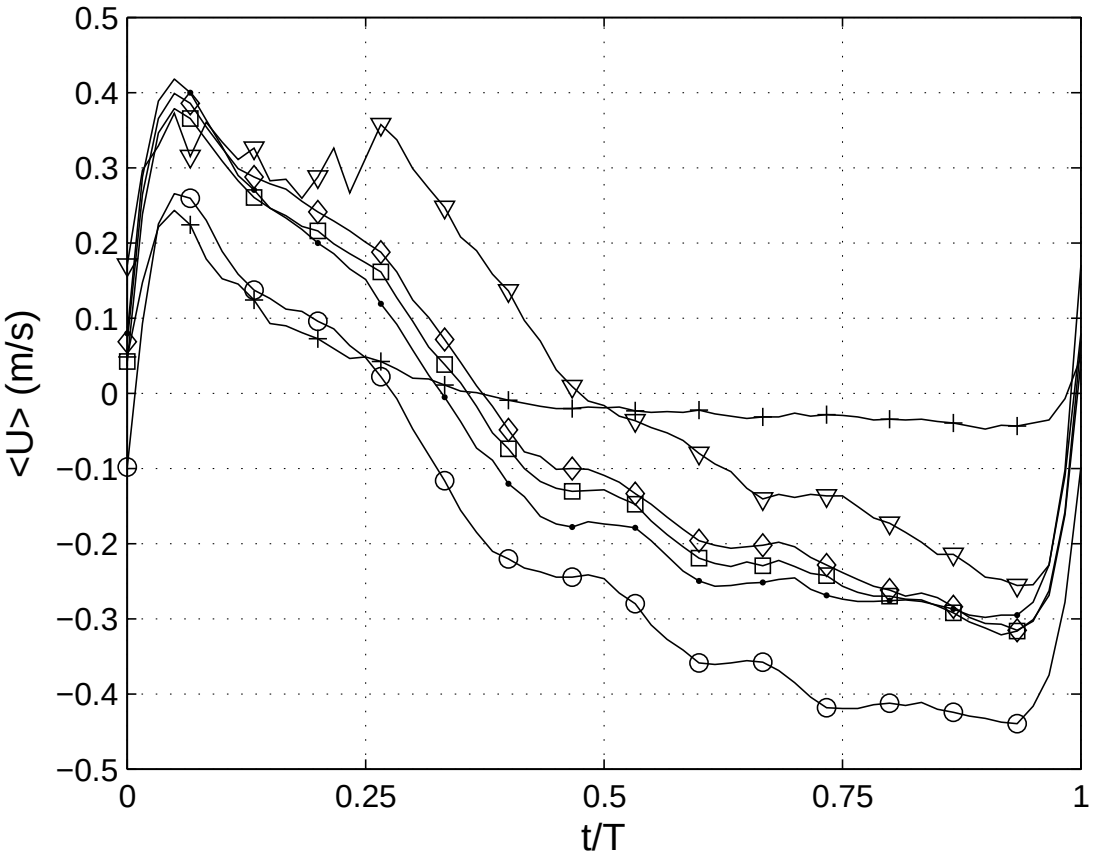

Figure 4.11: Run 6 Cart ADV phase averaged cross shore velocity U. ADV00 $-\bullet-$ at 0.007 m; ADV03 $-+-$ at 0.009 m; ADV07 $-\square-$ at 0.046 m; ADV01 $-\circ-$ at 0.062 m; ADV02 $-\diamond-$ 0.08 m; ADV05 $-\bigtriangledown-$ at 0.125 m.

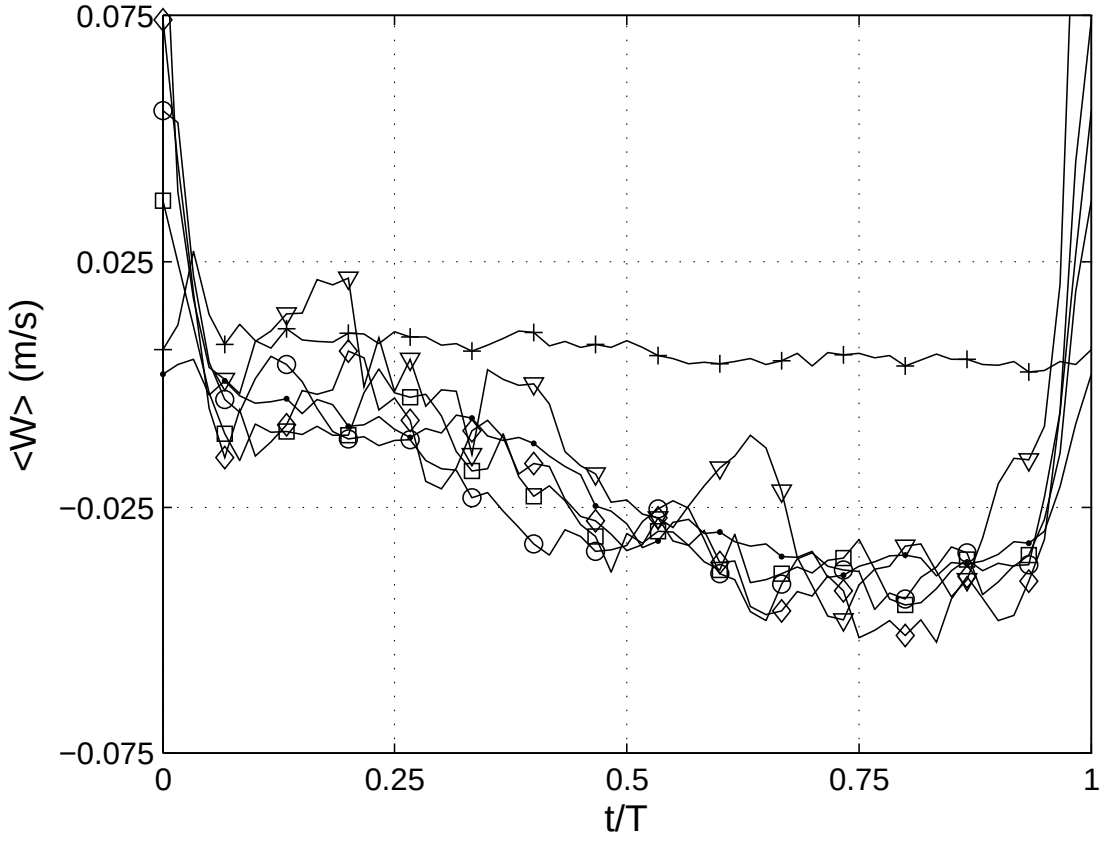

Figure 4.12: Run 6 Cart ADV phase averaged vertical velocity W. ADV00 $-\bullet-$ at 0.007 m; ADV03 $-+-$ at 0.009 m; ADV07 $-\square-$ at 0.046 m; ADV01 $-\circ-$ at 0.062 m; ADV02 $-\diamond-$ 0.08 m; ADV05 $-\bigtriangledown-$ at 0.125 m.

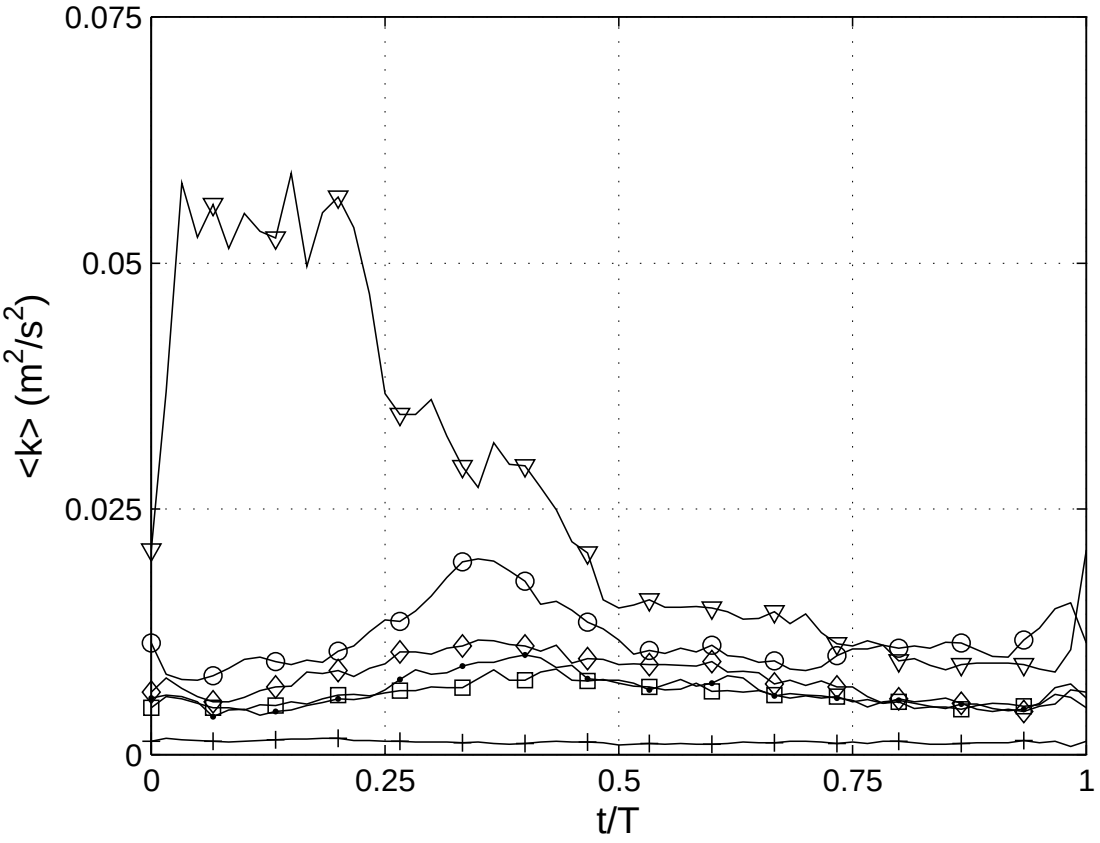

Figure 4.13: Run 6 Cart ADV phase averaged TKE (k). ADV00 $-\bullet-$ at 0.007 m; ADV03 $-+-$ at 0.009 m; ADV07 $-\square-$ at 0.046 m; ADV01 $-\circ-$ at 0.062 m; ADV02 $-\diamond-$ 0.08 m; ADV05 $-\bigtriangledown-$ at 0.125 m.

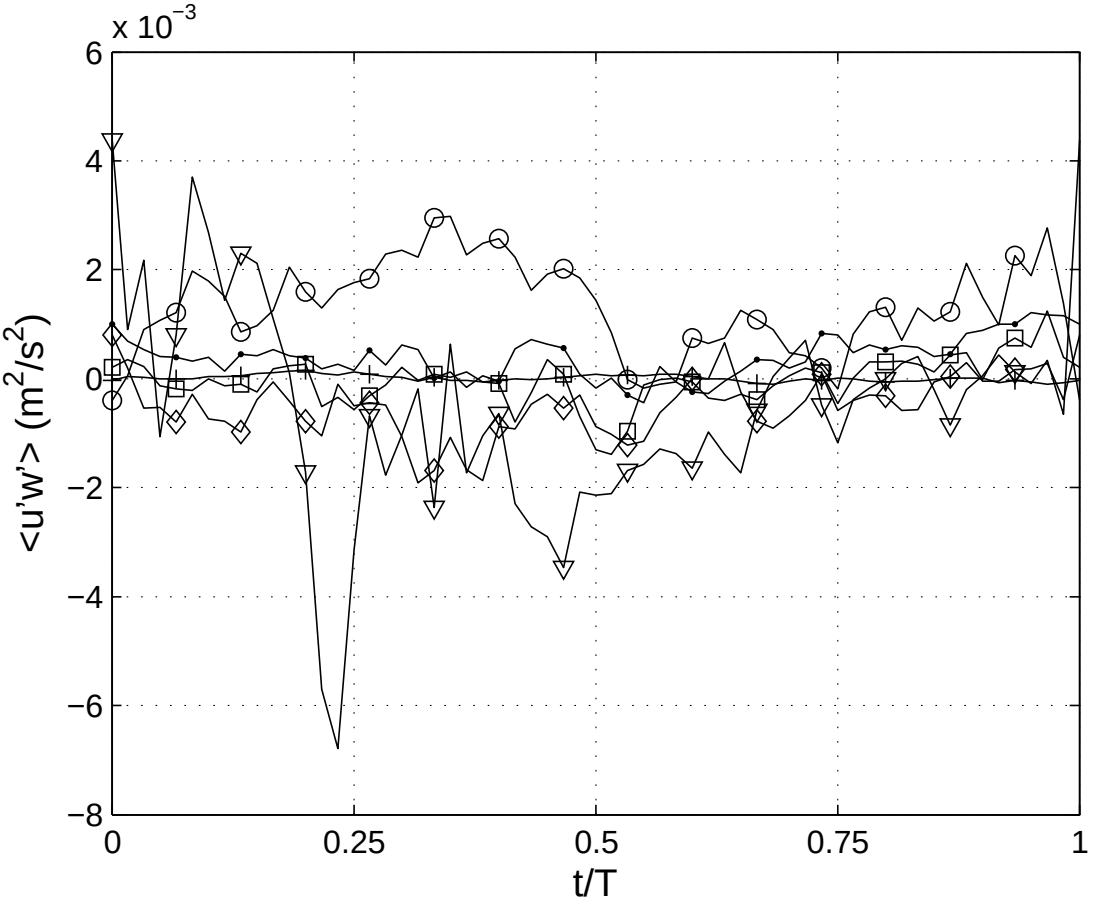

Figure 4.14: Run 6 Cart ADV phase averaged Reynold's stress $u'w'$. ADV00 $-\bullet-$ at 0.007 m; ADV03 $-+-$ at 0.009 m; ADV07 $-\square-$ at 0.046 m; ADV01 $-\circ-$ at 0.062 m; ADV02 $-\diamond-$ 0.08 m; ADV05 $-\bigtriangledown-$ at 0.125 m.

sediment velocity measurements.

In general, turbulence intensities show less variation throughout the water column than for Run 6, and also higher levels, with typical values above 0.1 m/s throughout the water column. This is more consistent with turbulence under a plunging breaker. Performing the same vertical mixing time calculation (eqn. 4.8), the dimensionless mixing time $\frac{t}{T} = 0.15$, the same order of magnitude as Run 6.

ADV05 (Figure 4.21) is out of the water during approximately 50% of the phase. The return signal drops to zero when it is out of the water, but quickly reaches a constant value under the wave crest/front. The very sharp fall off of the signal indicates the flow is not nearly as turbulent once the bore passes, and indeed the vertical turbulent intensity declines quickly just before the return signal drops to zero and the head comes out of the water.

There is still evidence of along shore transport from the bathymetry and v velocity records, although not as strong as in Run 6. A final interesting feature of the velocities are the double peaks in u at the bore front, most clear in Figures 4.19 and 4.20, but visible in most of the ADV records.

4.3.3 Run 21

Run 21 has the largest wave height of the runs considered and for all regular wave cases run during CROSSTEX. It's larger wave height may shift it more to the spilling side of the turbulence dynamics and also contribute to the strong off shore velocity observed at all elevations. There is some indication of spilling turbulence in the near constant turbulence intensities throughout the phase at all sensors, characteristic of spilling waves. A small peak still occurs just after the arrival

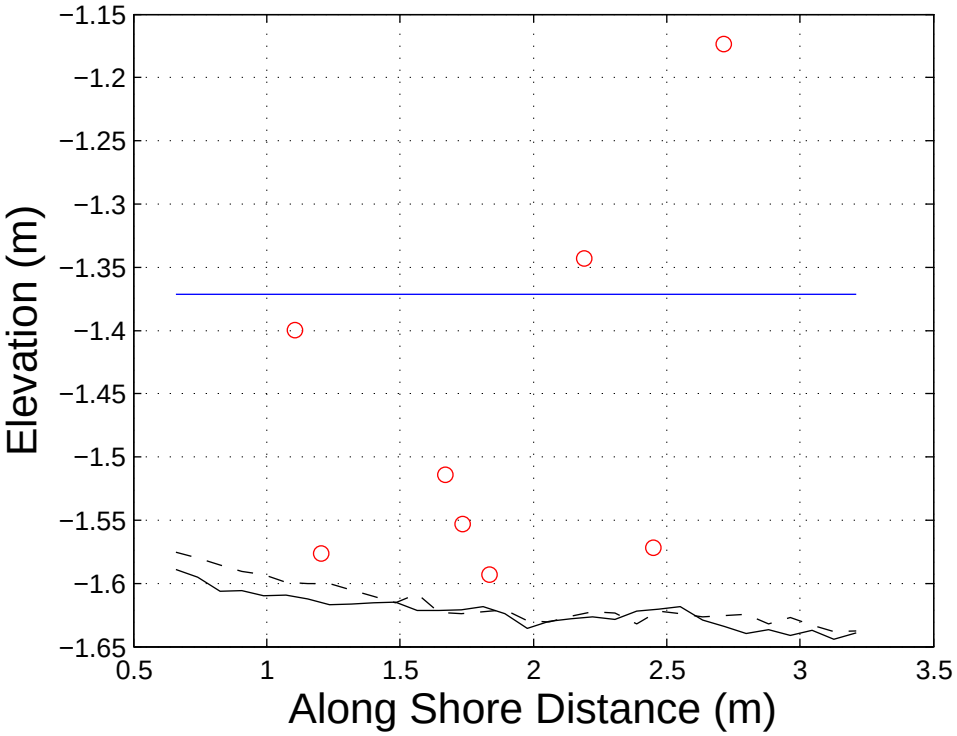

Figure 4.15: Run 16 bathymetry below the cart ADVs at the start (-) and end (- -) of the run looking offshore (same orientation as Figure 2.4). The solid flat line represents the SWL. ADVs are marked with ○.

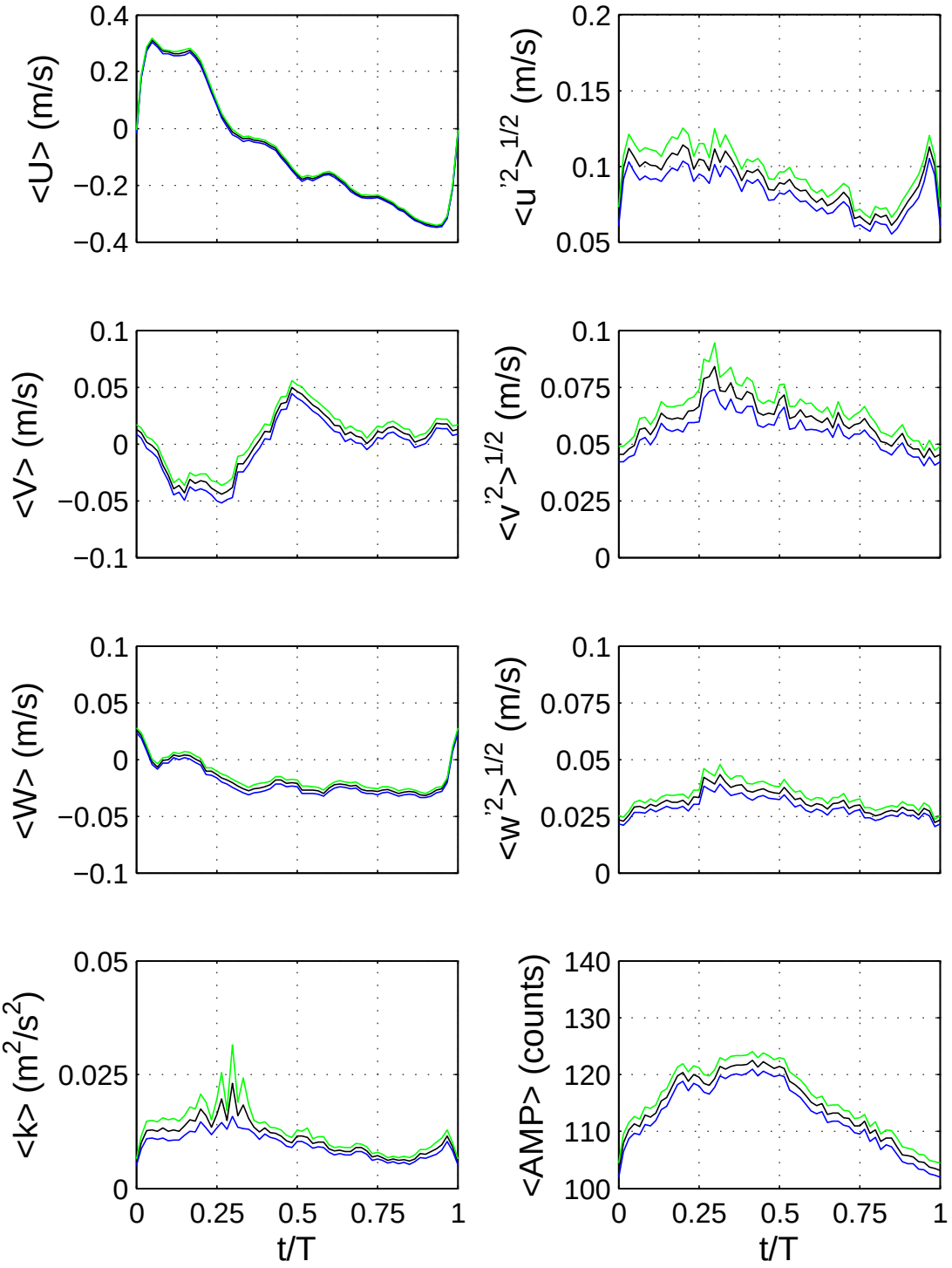

Figure 4.16: Run 16 Cart ADV00 phase averaged velocities, turbulent intensities, turbulent kinetic energy, and return signal amplitude at 0.027 m above the bed, center wing.

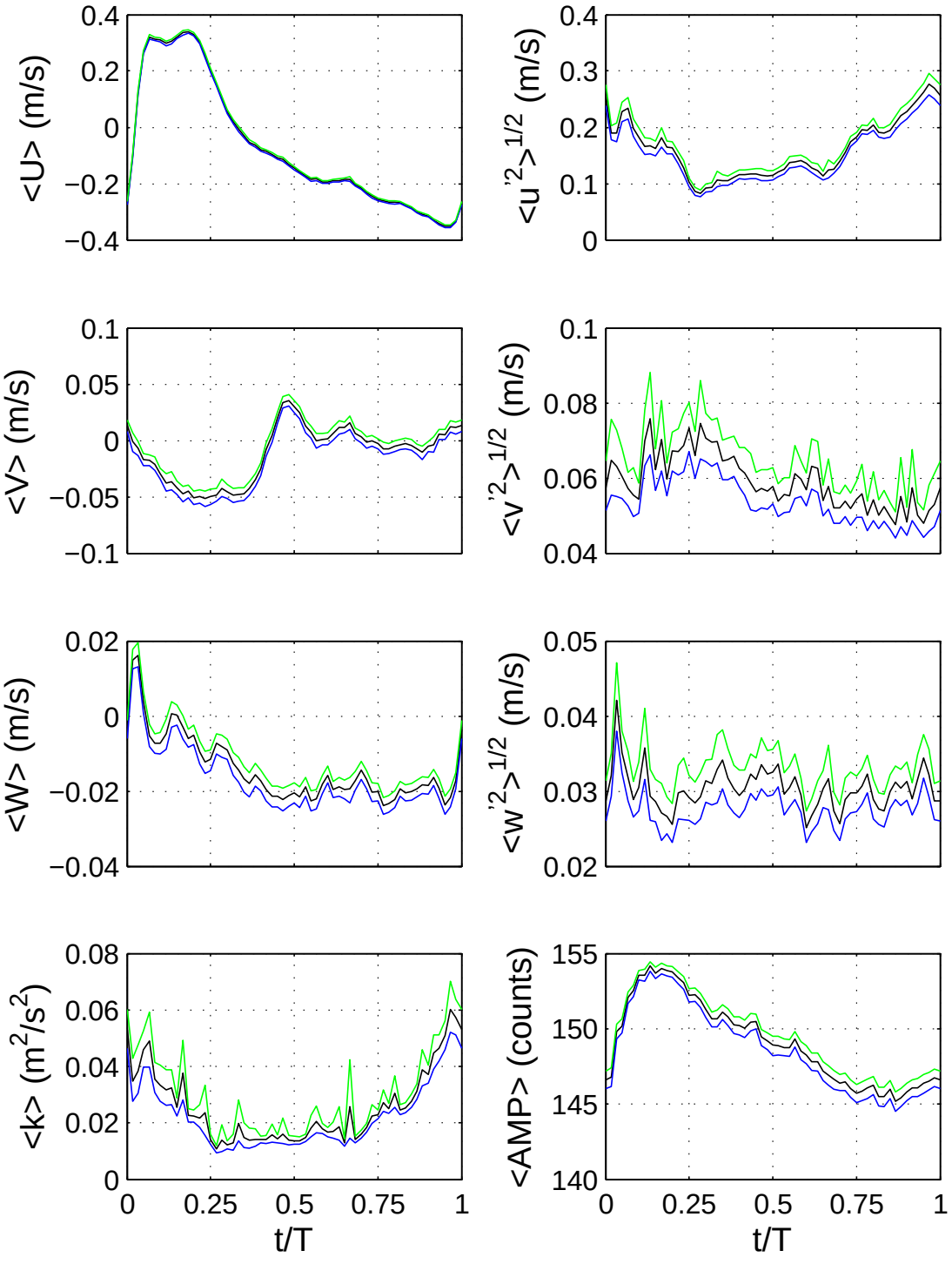

Figure 4.17: Run 16 Cart ADV03 phase averaged velocities, turbulent intensities, turbulent kinetic energy, and return signal amplitude at 0.0436 m above the bed, left wing.

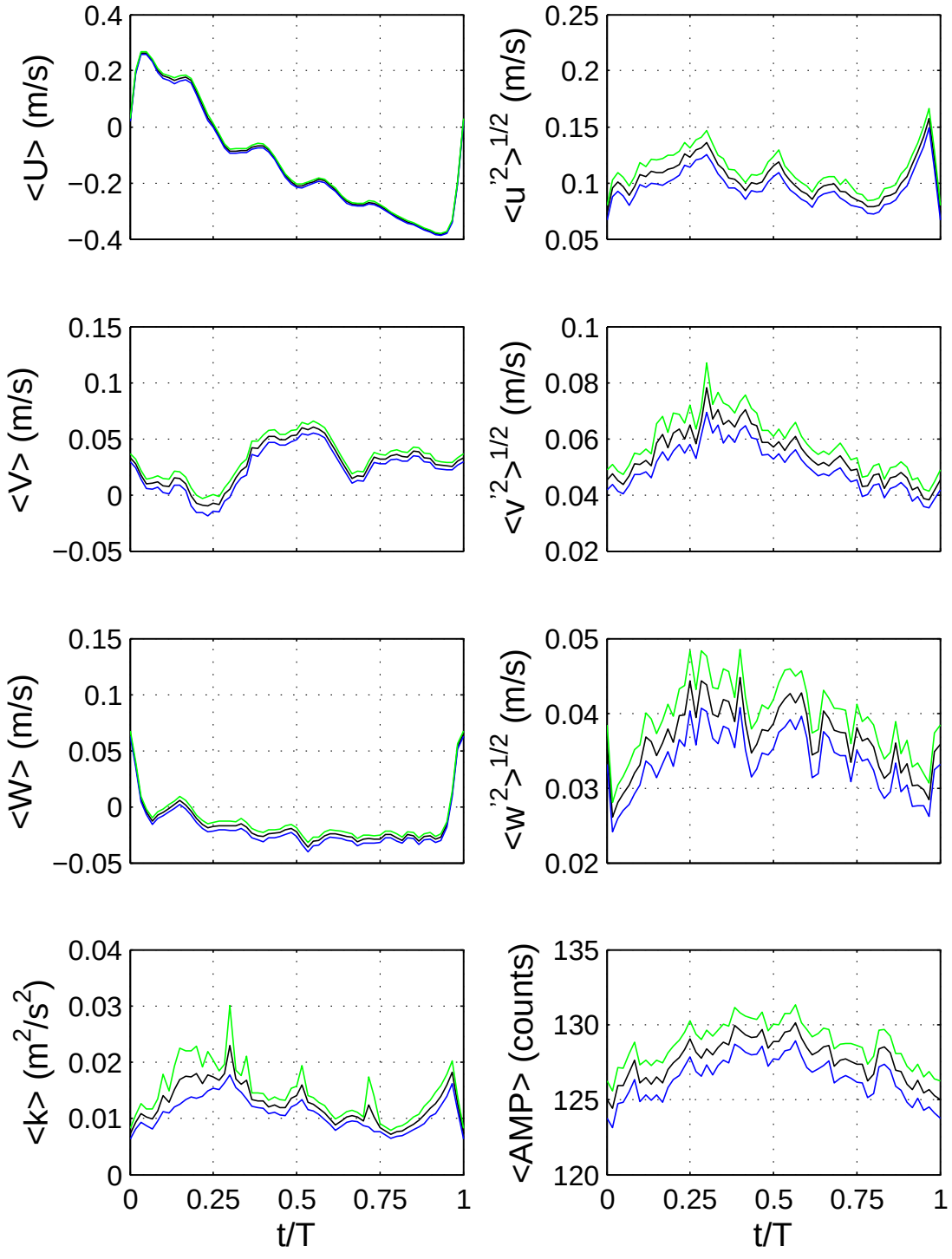

Figure 4.18: Run 16 Cart ADV01 phase averaged velocities, turbulent intensities, turbulent kinetic energy, and return signal amplitude at 0.049 m above the bed, right wing.

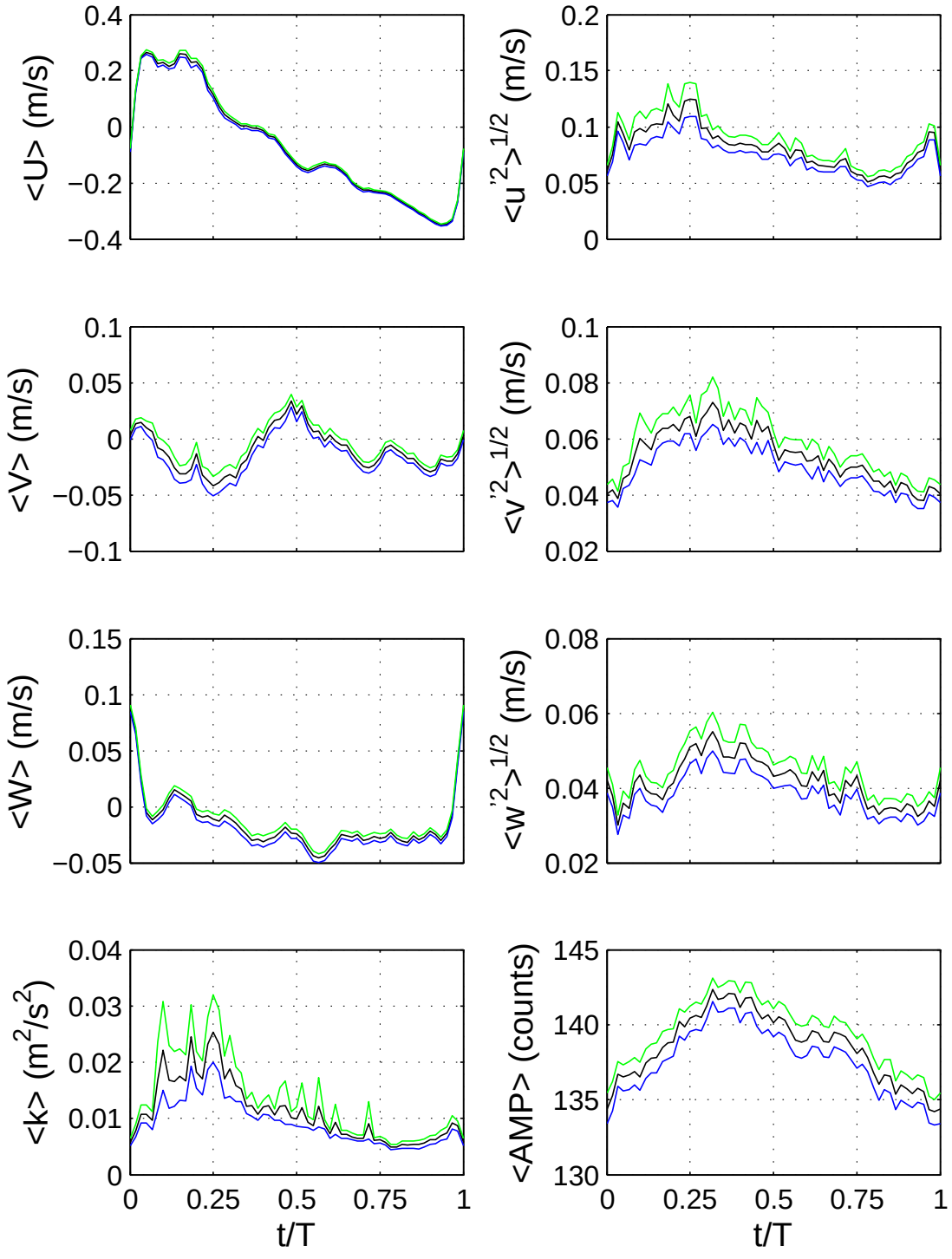

Figure 4.19: Run 16 Cart ADV07 phase averaged velocities, turbulent intensities, turbulent kinetic energy, and return signal amplitude at 0.0678 m above the bed, center wing.

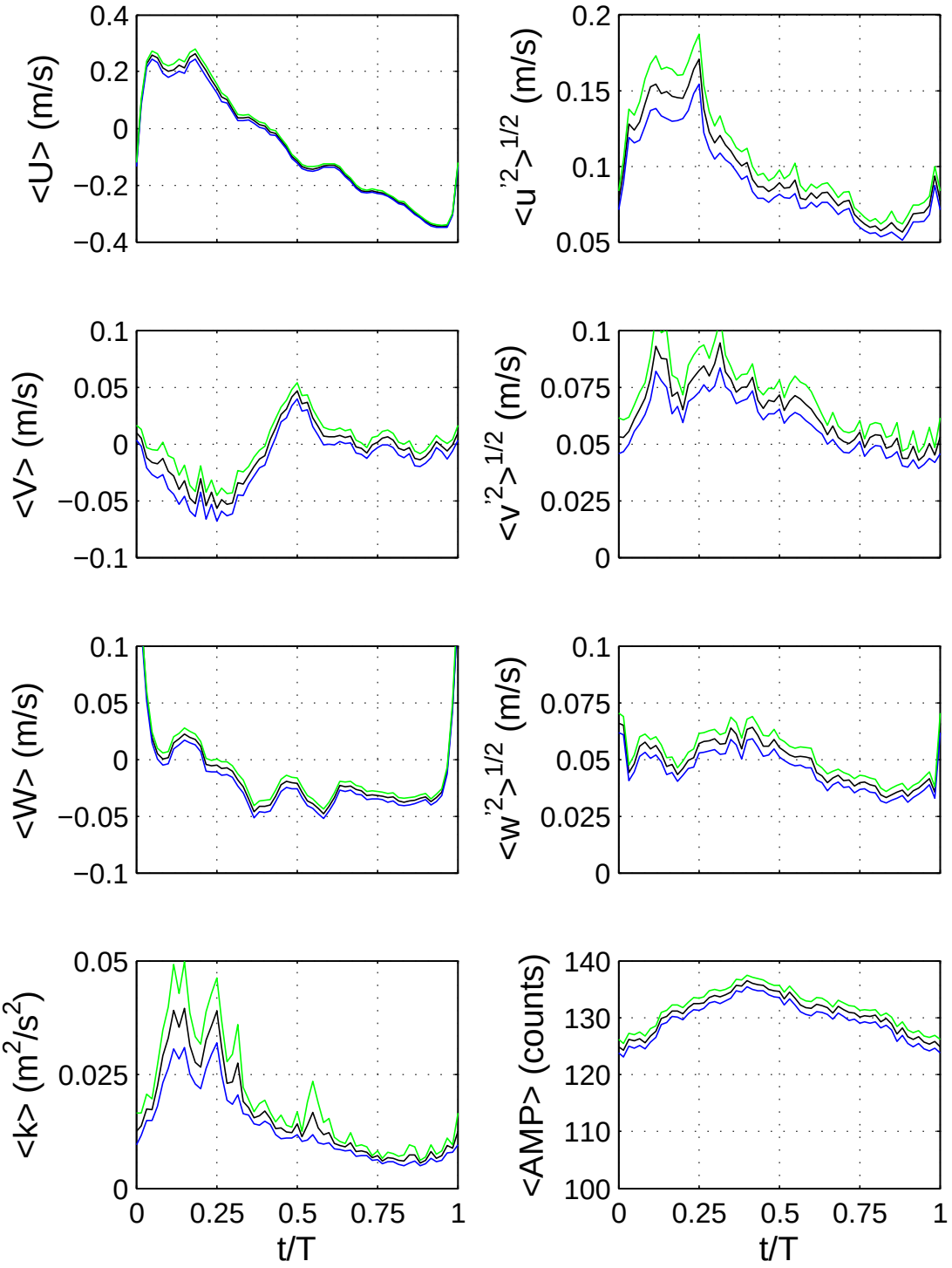

Figure 4.20: Run 16 Cart ADV02 phase averaged velocities, turbulent intensities, turbulent kinetic energy, and return signal amplitude at 0.107 m above the bed, center wing.

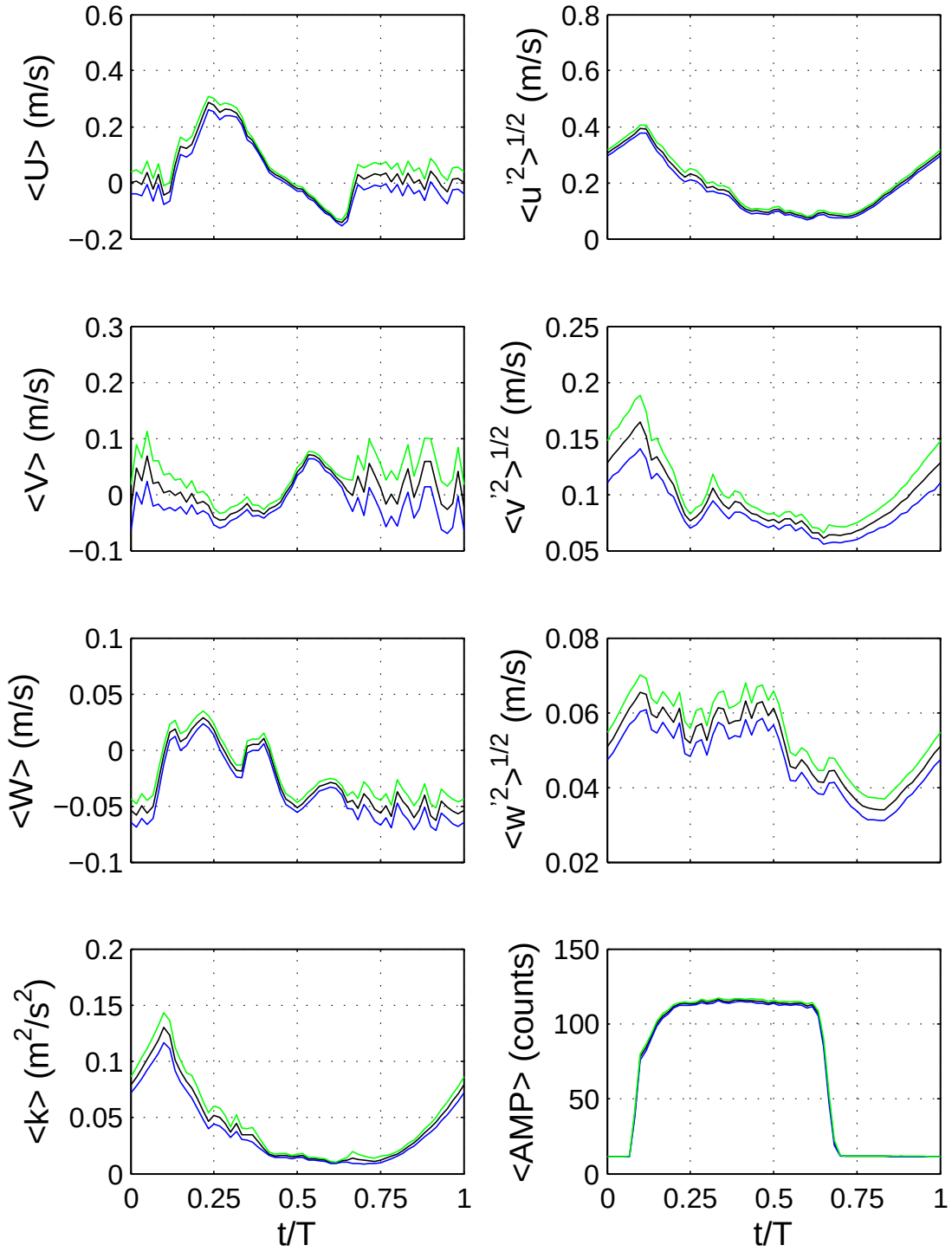

Figure 4.21: Run 16 Cart ADV05 phase averaged velocities, turbulent intensities, turbulent kinetic energy, and return signal amplitude at 0.14 m above the bed, left wing.

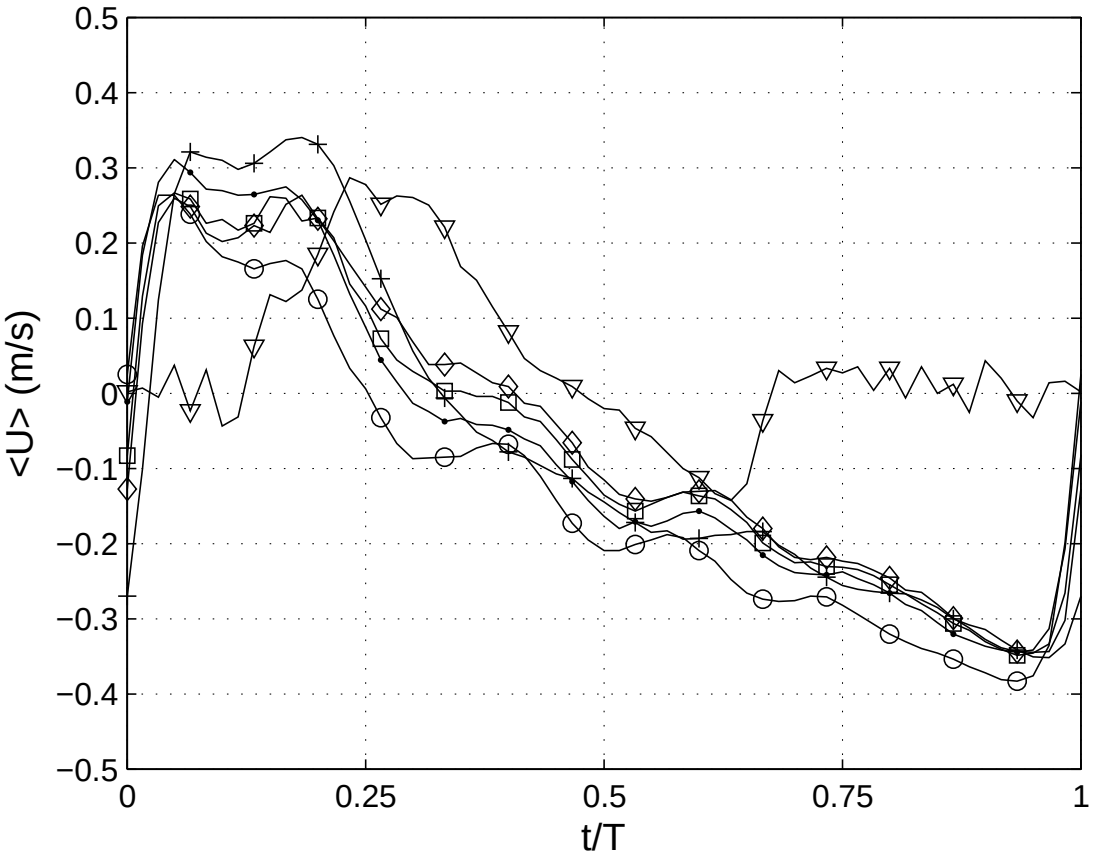

Figure 4.22: Run 16 Cart ADV phase averaged cross shore velocity U. ADV00 $-\bullet-$ at 0.027 m; ADV03 $-+-$ at 0.0436 m; ADV01 $-\circ-$ at 0.049 m; ADV07 $-\square-$ at 0.0678 m; ADV02 $-\diamond-$ 0.107 m; ADV05 $-\bigtriangledown-$ at 0.14 m.

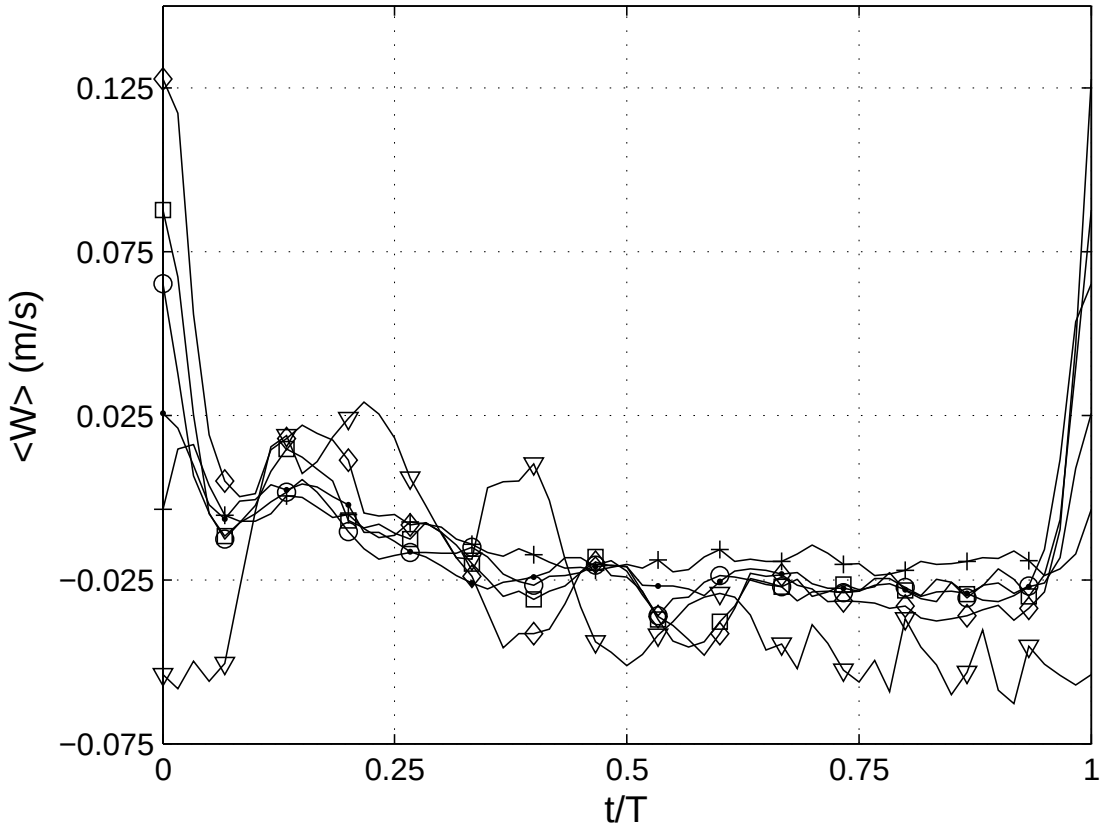

Figure 4.23: Run 16 Cart ADV phase averaged vertical velocity W. ADV00 $-\bullet-$ at 0.027 m; ADV03 $-+-$ at 0.0436 m; ADV01 $-\circ-$ at 0.049 m; ADV07 $-\square-$ at 0.0678 m; ADV02 $-\diamond-$ 0.107 m; ADV05 $-\bigtriangledown-$ at 0.14 m.

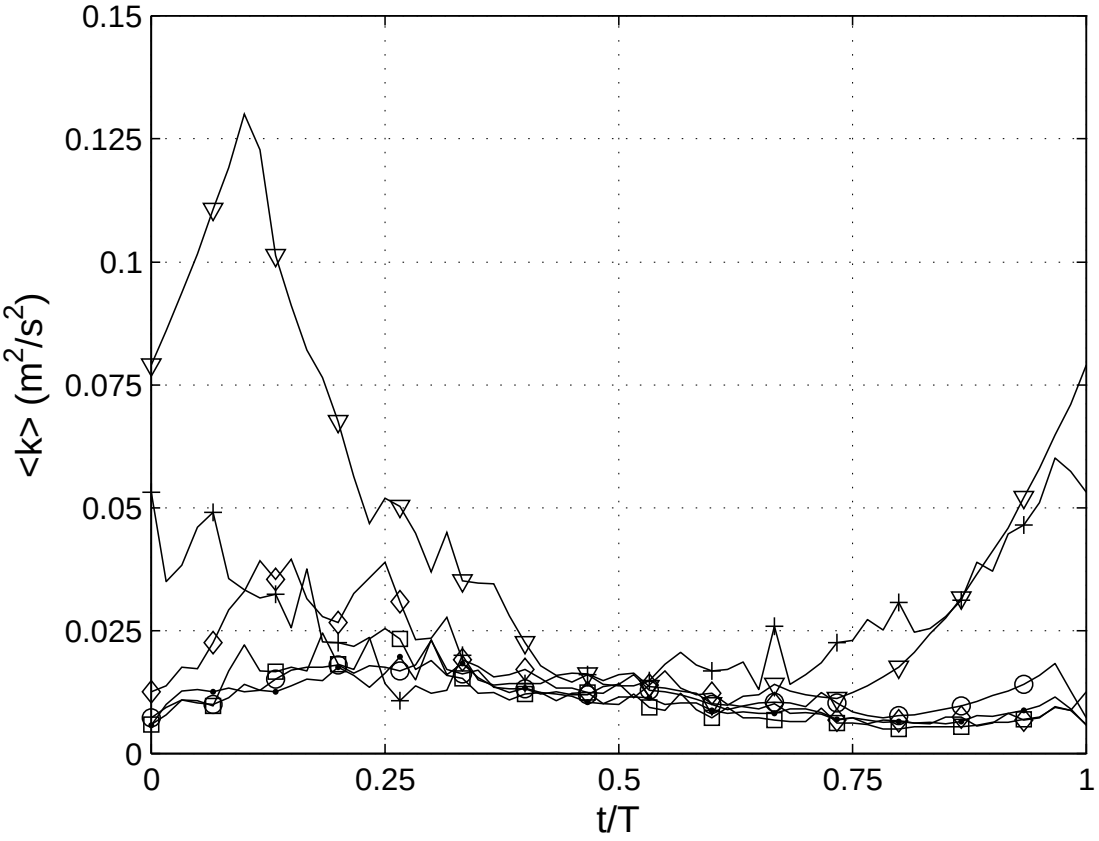

Figure 4.24: Run 16 Cart ADV phase averaged TKE (k). ADV00 $-\bullet-$ at 0.027 m; ADV03 $-+-$ at 0.0436 m; ADV01 $-\circ-$ at 0.049 m; ADV07 $-\square-$ at 0.0678 m; ADV02 $-\diamond-$ 0.107 m; ADV05 $-\bigtriangledown-$ at 0.14 m.

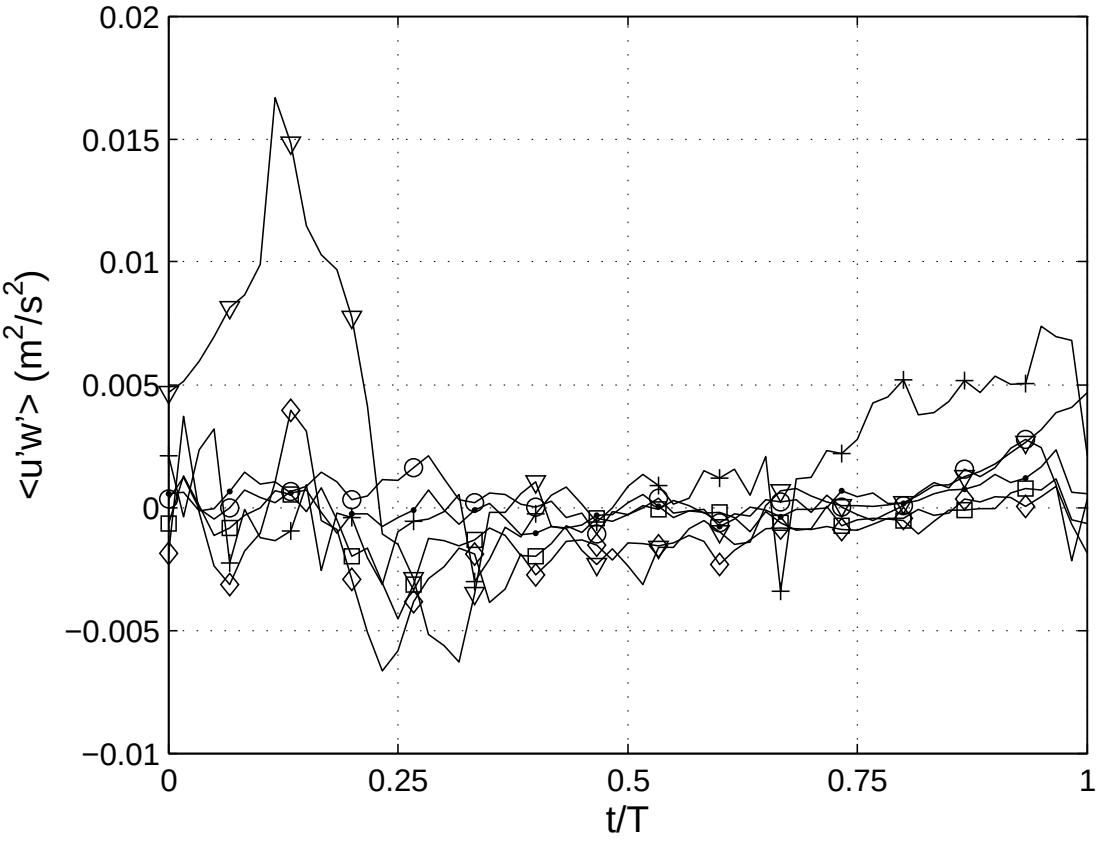

Figure 4.25: Run 16 Cart ADV phase averaged Reynold's stress $u'w'$. ADV00 $-\bullet-$ at 0.027 m; ADV03 $-+-$ at 0.0436 m; ADV01 $-\circ-$ at 0.049 m; ADV07 $-\square-$ at 0.0678 m; ADV02 $-\diamond-$ 0.107 m; ADV05 $-\bigtriangledown-$ at 0.14 m.

of the bore front, but it is not as pronounced as Runs 6 and 16. The return signal strength also remains constant throughout the phase and profile, indicating a consistently well mixed water column.

Run 21 shows the largest alongshore slope of any of the runs examined. The slope remains relatively constant and it appears as if features (the trough between the left and center wings) are moving across the tank. The along shore velocity is affected by this strong slope, remaining largely positive throughout the phase, with the only significant change in sign occurring on ADV01 on the right wing.

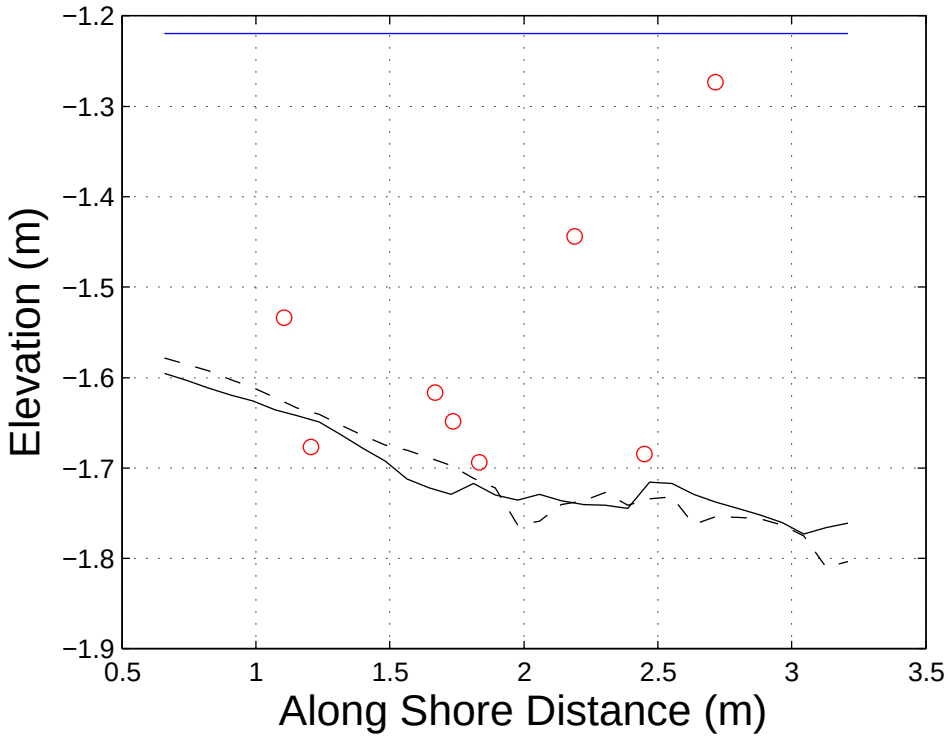

Figure 4.26: Run 21 bathymetry below the cart ADVs at the start (-) and end (- -) of the run looking offshore (same orientation as Figure 2.4). The solid flat line represents the SWL. ADVs are marked with ○.

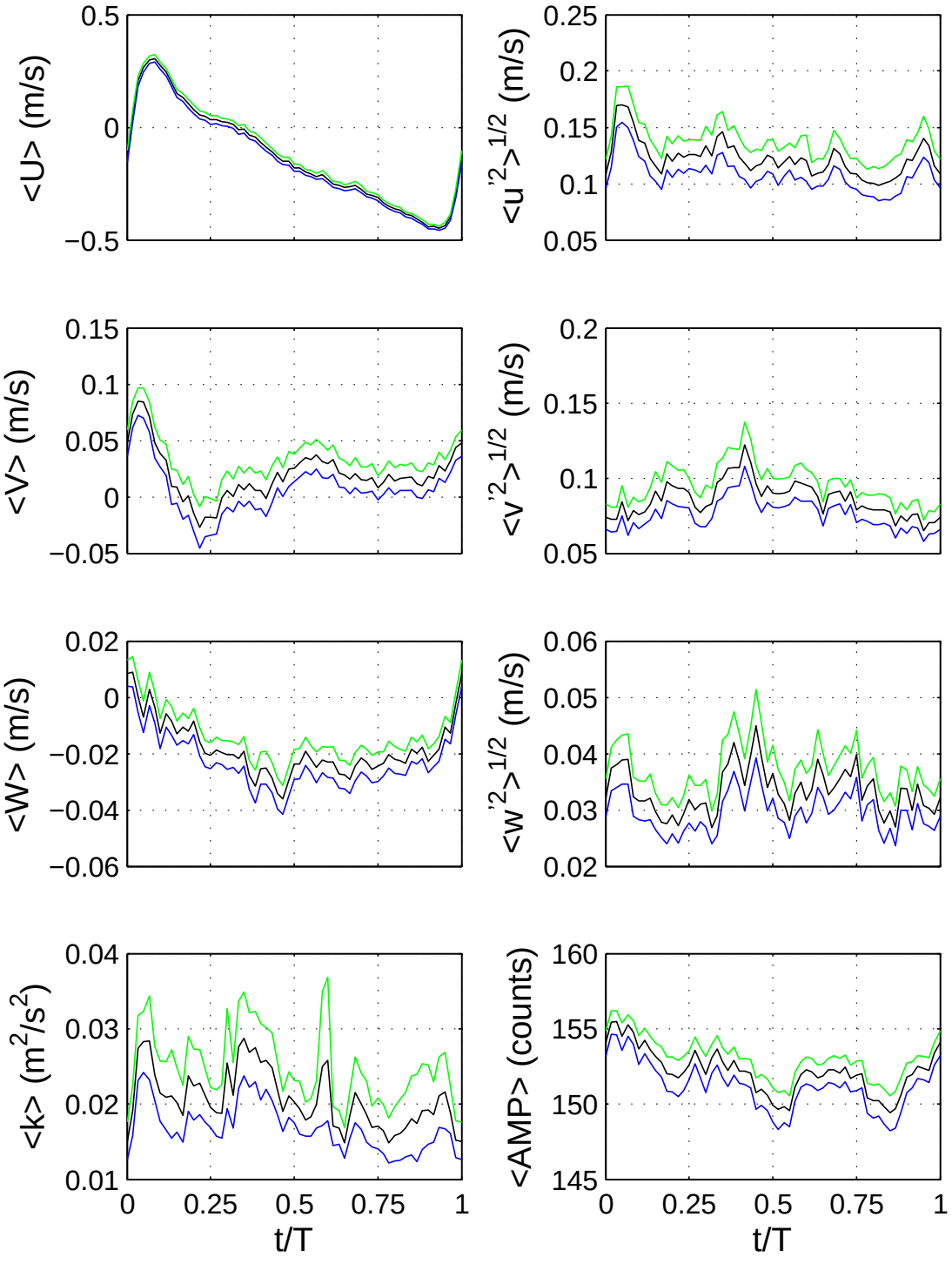

Figure 4.27: Run 21 Cart ADV00 phase averaged velocities, turbulent intensities, turbulent kinetic energy, and return signal amplitude at 0.027 m above the bed, center wing.

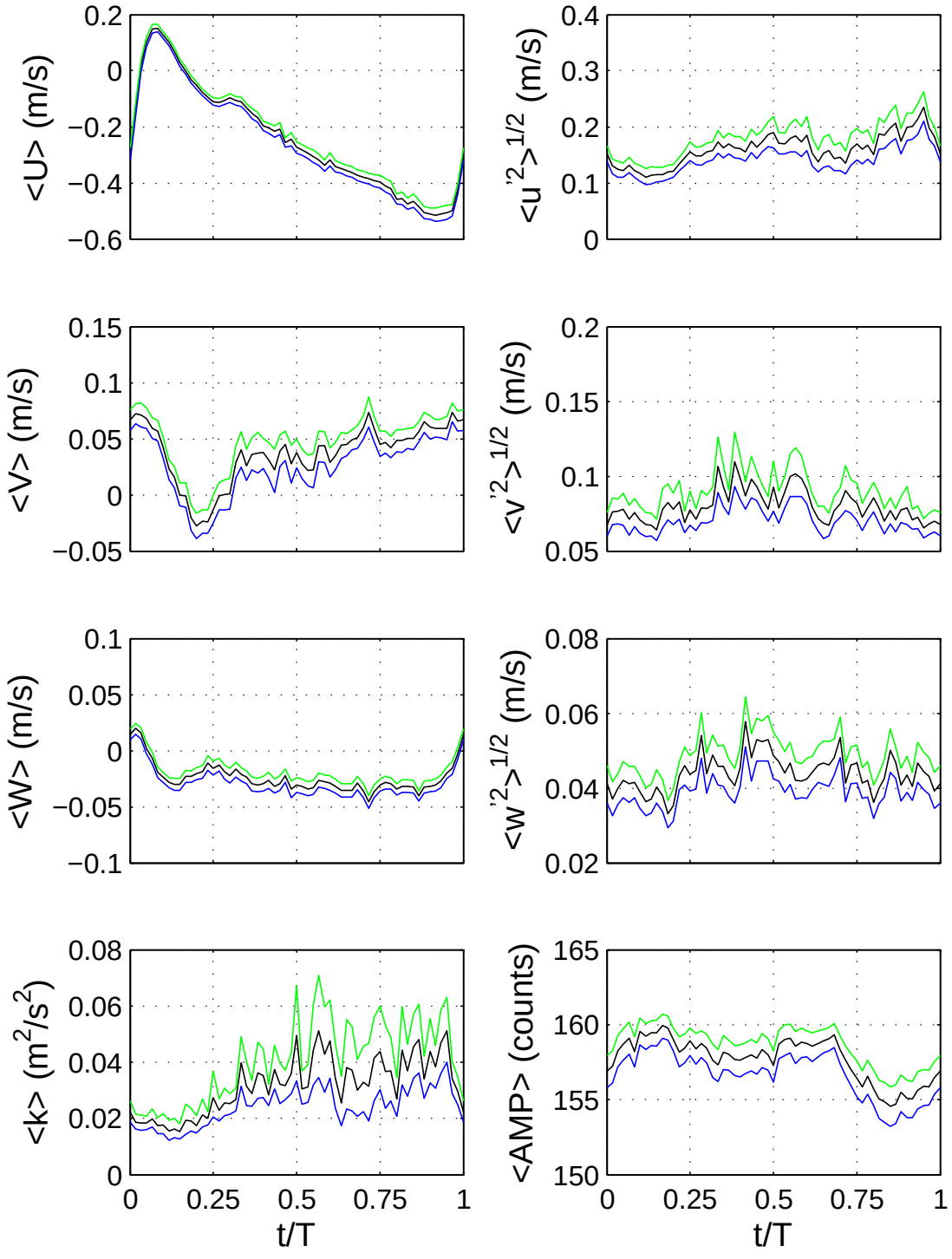

Figure 4.28: Run 21 Cart ADV01 phase averaged velocities, turbulent intensities, turbulent kinetic energy, and return signal amplitude at 0.038 m above the bed, right wing.

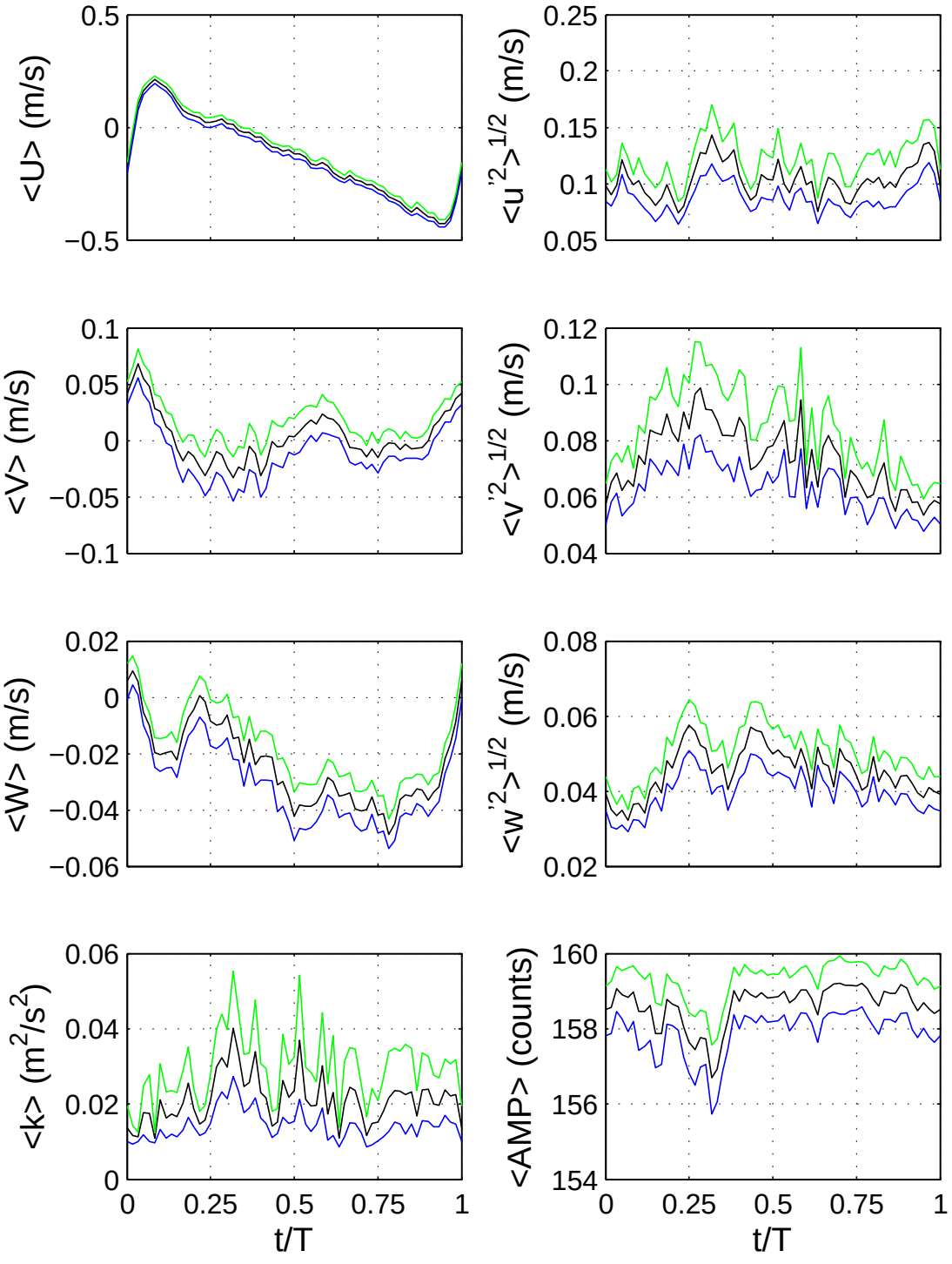

Figure 4.29: Run 21 Cart ADV07 phase averaged velocities, turbulent intensities, turbulent kinetic energy, and return signal amplitude at 0.0798 m above the bed, center wing.

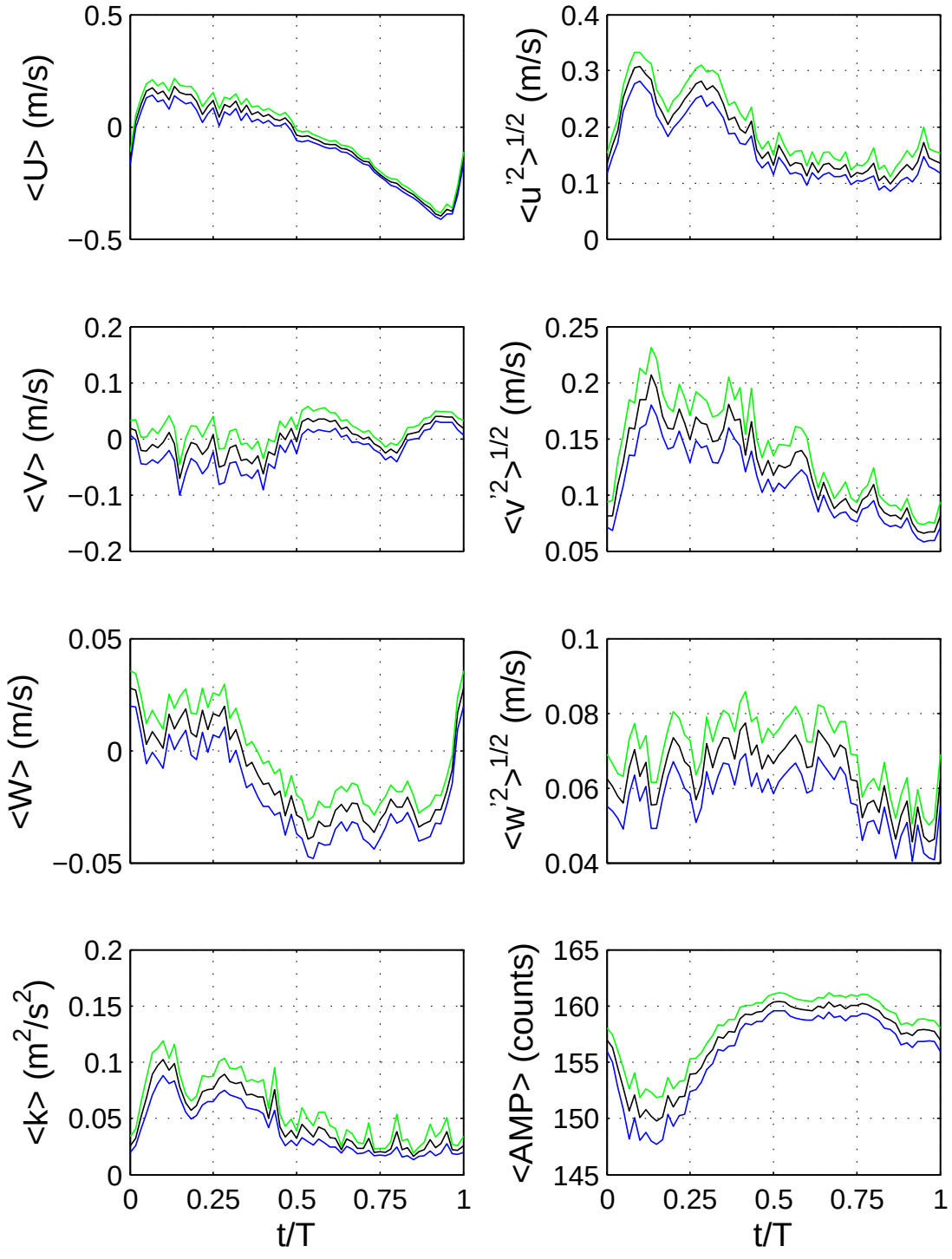

Figure 4.30: Run 21 Cart ADV05 phase averaged velocities, turbulent intensities, turbulent kinetic energy, and return signal amplitude at 0.104 m above the bed, left wing.

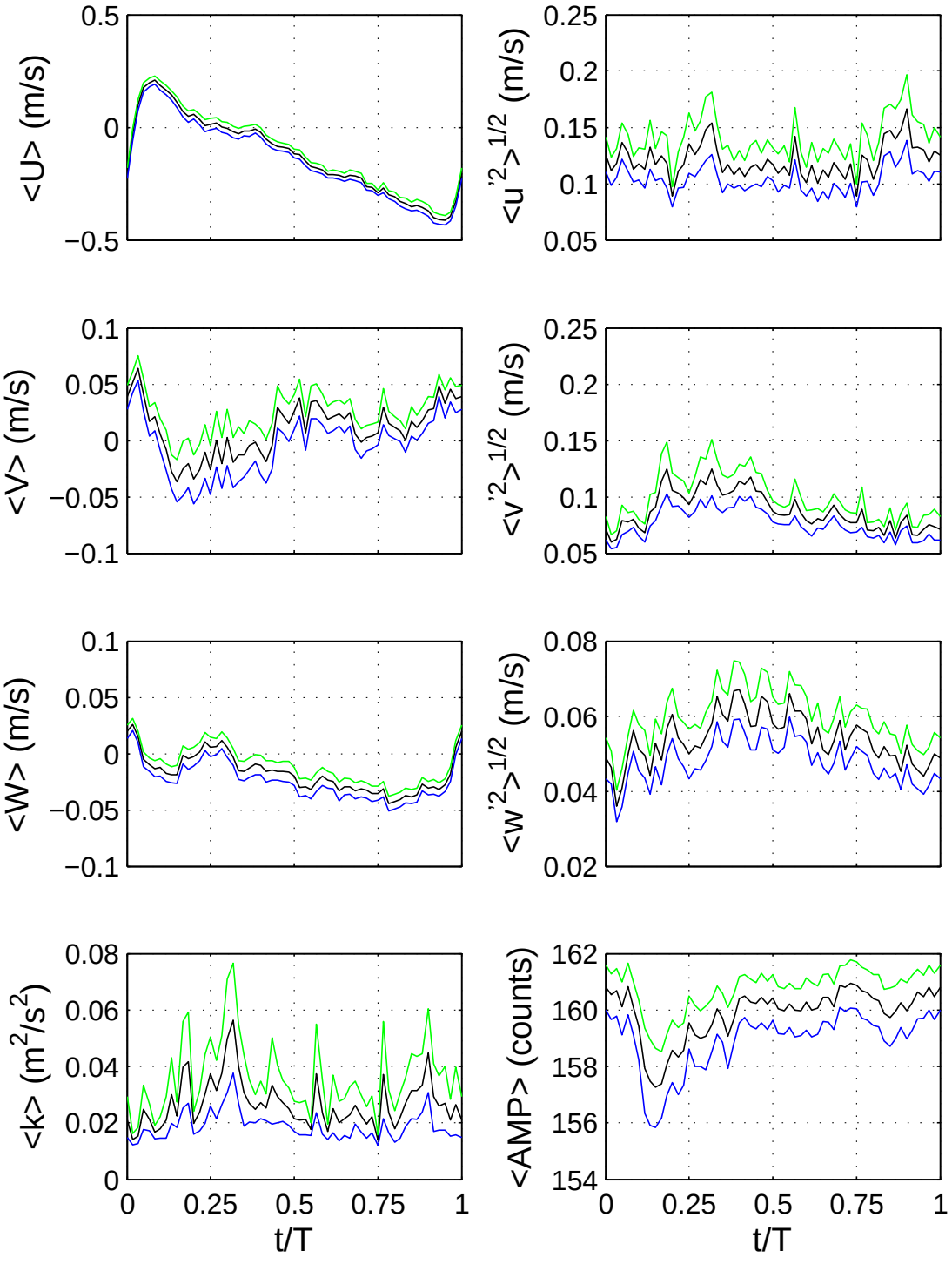

Figure 4.31: Run 21 Cart ADV02 phase averaged velocities, turbulent intensities, turbulent kinetic energy, and return signal amplitude at 0.107 m above the bed, center wing.

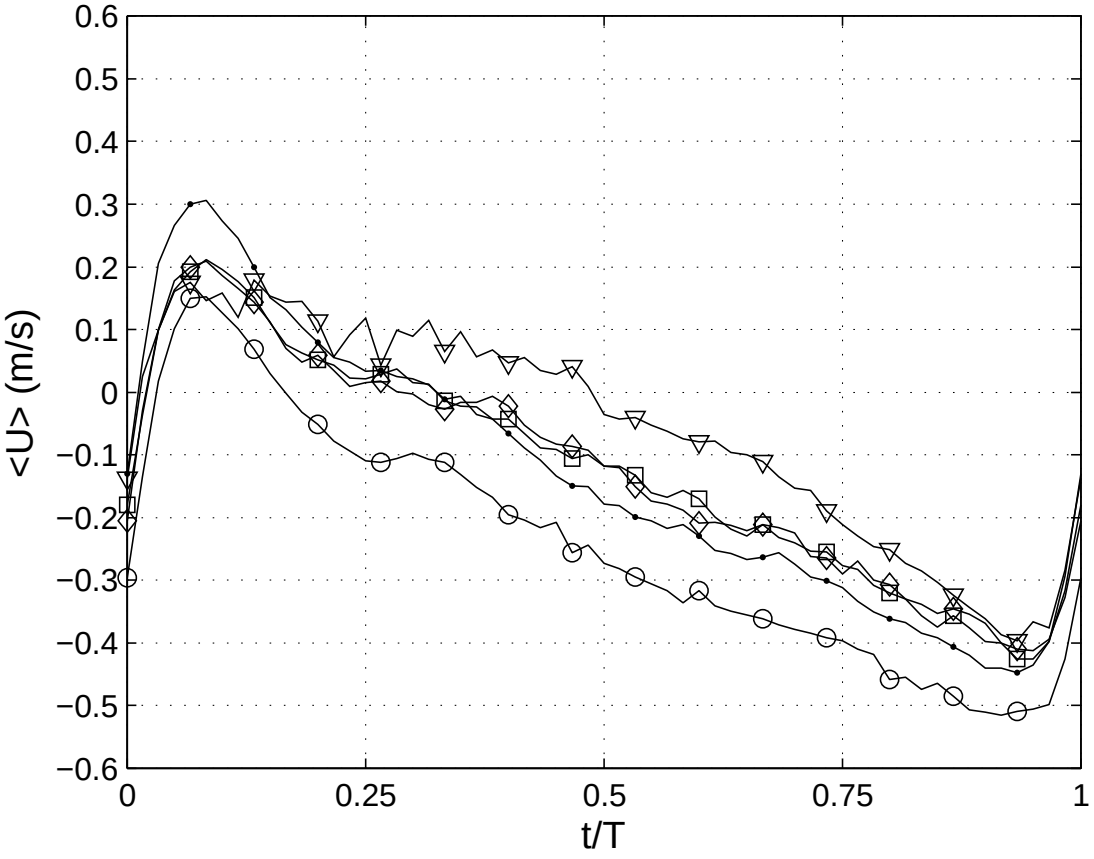

Figure 4.32: Run 21 Cart ADV phase averaged cross shore velocity U. ADV00 $-\bullet-$ at 0.027 m; ADV01 $-\circ-$ at 0.038 m; ADV07 $-\square-$ at 0.0798 m; ADV05 $-\triangledown-$ at 0.104 m; ADV02 $-\diamond-$ 0.107 m.

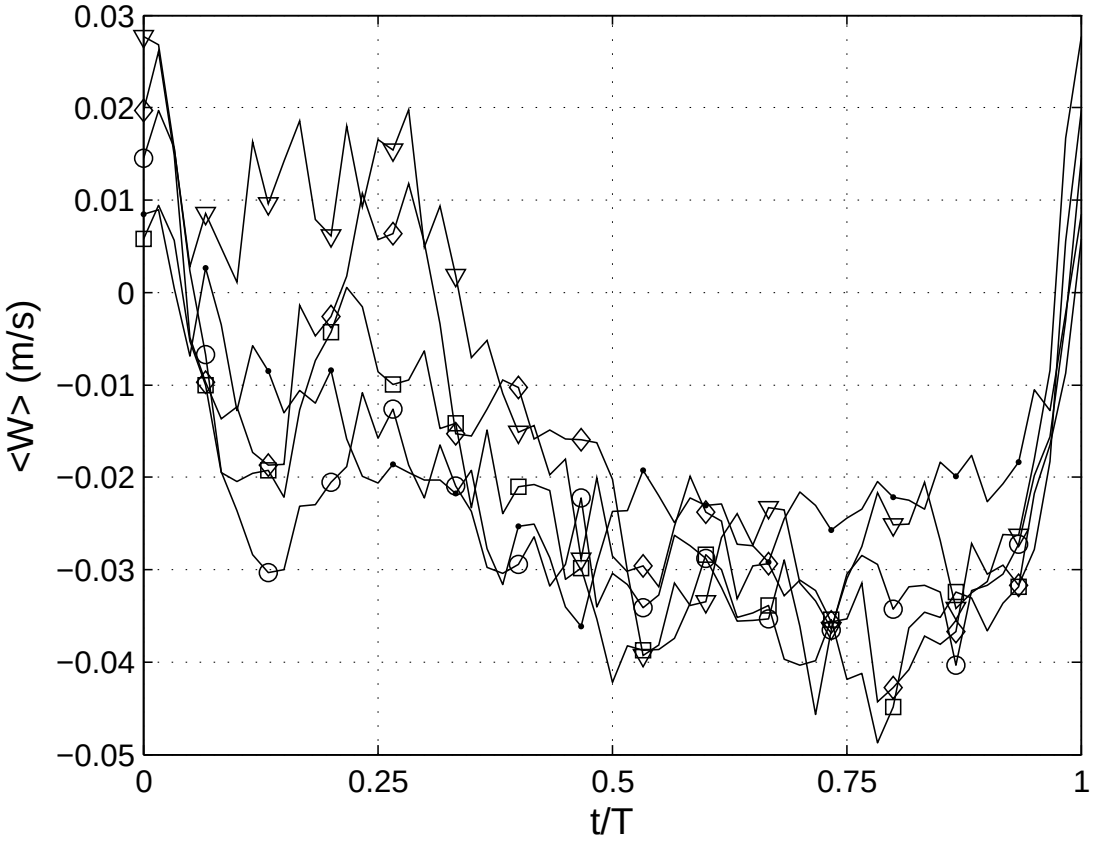

Figure 4.33: Run 21 Cart ADV phase averaged vertical velocity W. ADV00 $-\bullet-$ at 0.027 m; ADV01 $-\circ-$ at 0.038 m; ADV07 $-\square-$ at 0.0798 m; ADV05 $-\bigtriangledown-$ at 0.104 m; ADV02 $-\diamond-$ 0.107 m.

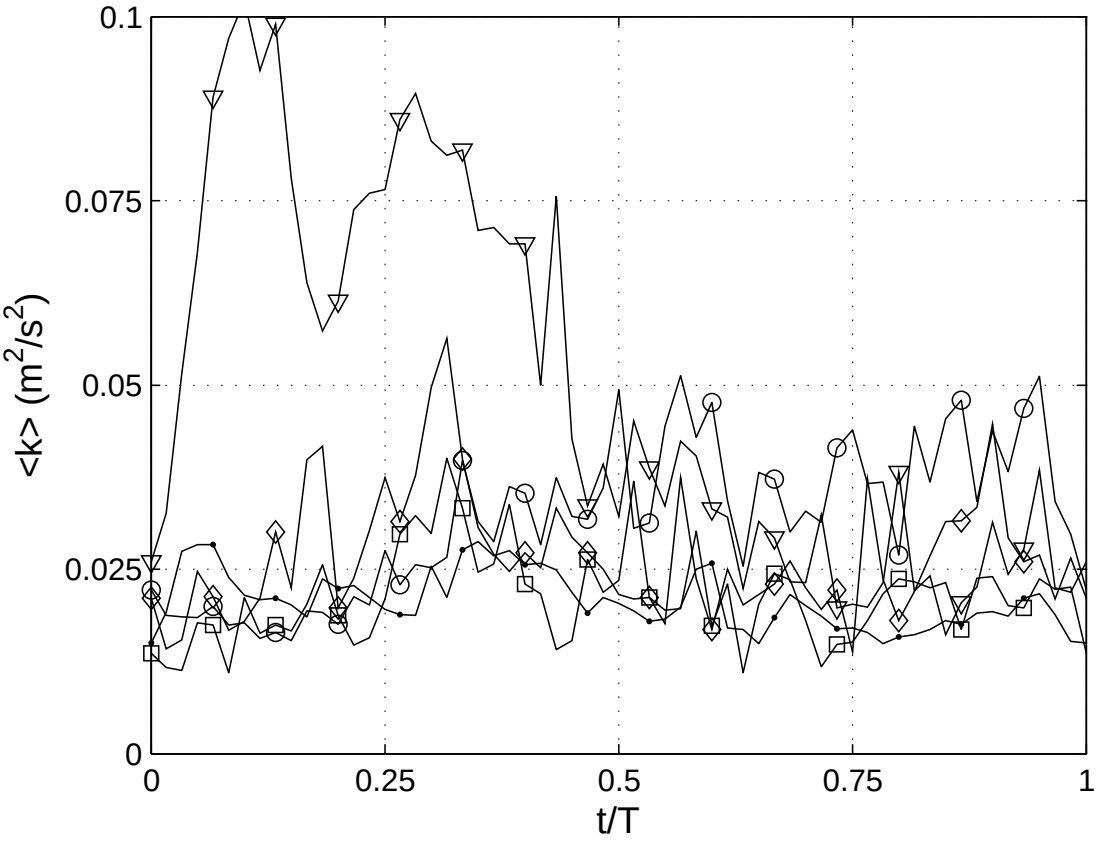

Figure 4.34: Run 21 Cart ADV phase averaged TKE (k). ADV00 $-\bullet-$ at 0.027 m; ADV01 $-\circ-$ at 0.038 m; ADV07 $-\square-$ at 0.0798 m; ADV05 $-\bigtriangledown-$ at 0.104 m; ADV02 $-\diamond-$ 0.107 m.

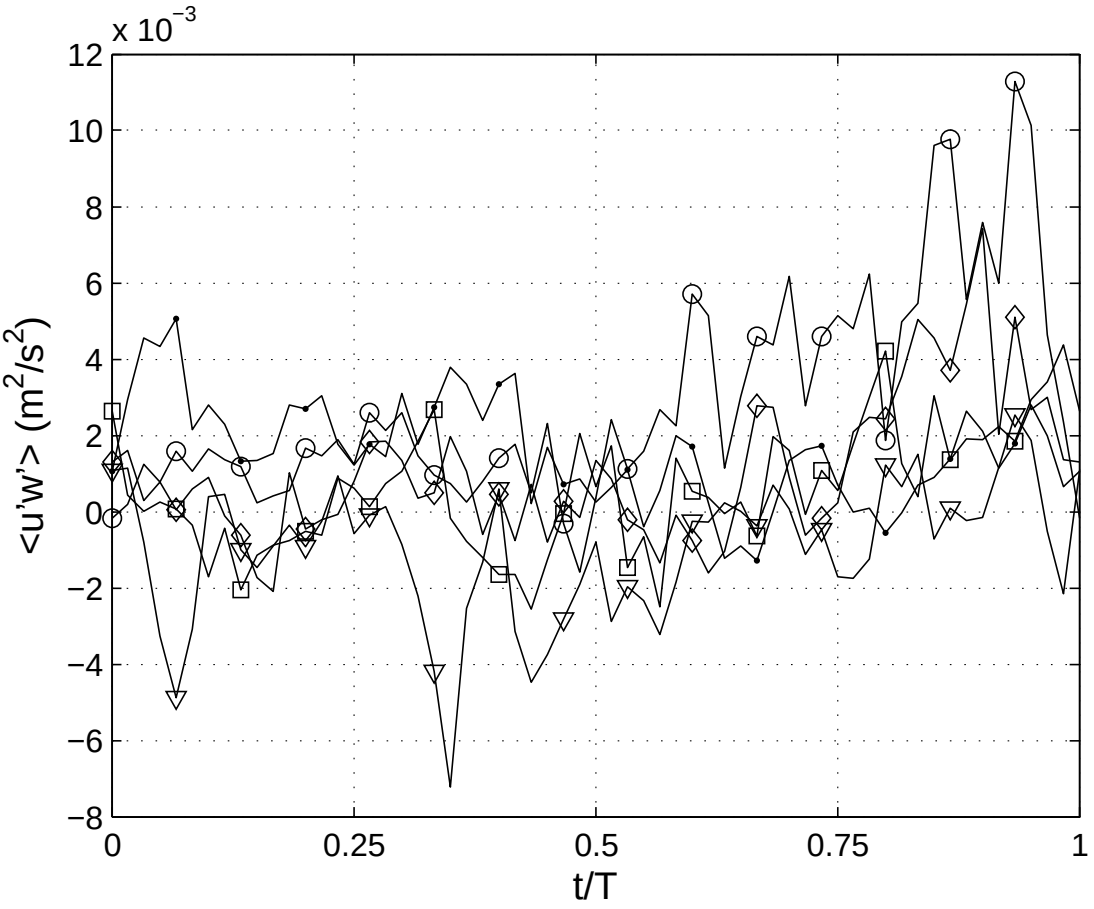

Figure 4.35: Run 21 Cart ADV phase averaged Reynold's stress $u'w'$. ADV00 $-\bullet-$ at 0.027 m; ADV01 $-\circ-$ at 0.038 m; ADV07 $-\square-$ at 0.0798 m; ADV05 $-\bigtriangledown-$ at 0.104 m; ADV02 $-\diamond-$ 0.107 m.

4.4 Reynold's Stresses and TKE

The six Reynold's Stresses from each ADV available were calculated using the decomposed turbulent velocity signal and were then phase averaged. Plots for each run of the Reynold's stress $u'w'$ are presented in Figures 4.14, 4.25 and 4.35, along with the TKE from each ADV for each run in Figures 4.13, 4.13 and 4.34. Near the surface around t/T = 0.25 there is a downward spike in each run in the plotted Reynolds stress measured by the the near surface ADVs and an associated increase in TKE throughout the water column. The plunging lip of the breaking wave driving down through the water column and the strong onshore flow associated with breaking cause this change in sign in the Reynolds stress. There is little change in the magnitude of this spike across the three runs, with the primary difference between the three the amount of variance in $u'w'$. Generally speaking, this tends to increase with wave height.

TKE does not exhibit a strong variance with wave height, at least in this basic analysis. Run 16, the smallest wave height, has a higher peak TKE at the surface than Run 6, but this peak decays quickly. Lower down in the water column, there appears to be a fairly uniform level of turbulence across the three runs and little variation with phase. As stated previously, turbulence increases significantly with the arrival of the bore front and decays rapidly before flow reversal.

4.5 Dissipation Estimates

An example frequency spectra computed from one of the cart ADVs is shown in Figure 4.36. The inertial subrange, indicated by a -5/3 slope is apparent beginning around 1 Hz. The spectra rolls off before the dissipation range is reached, but

dissipation can still be estimated by using Taylor's Frozen Turbulence Hypothesis.

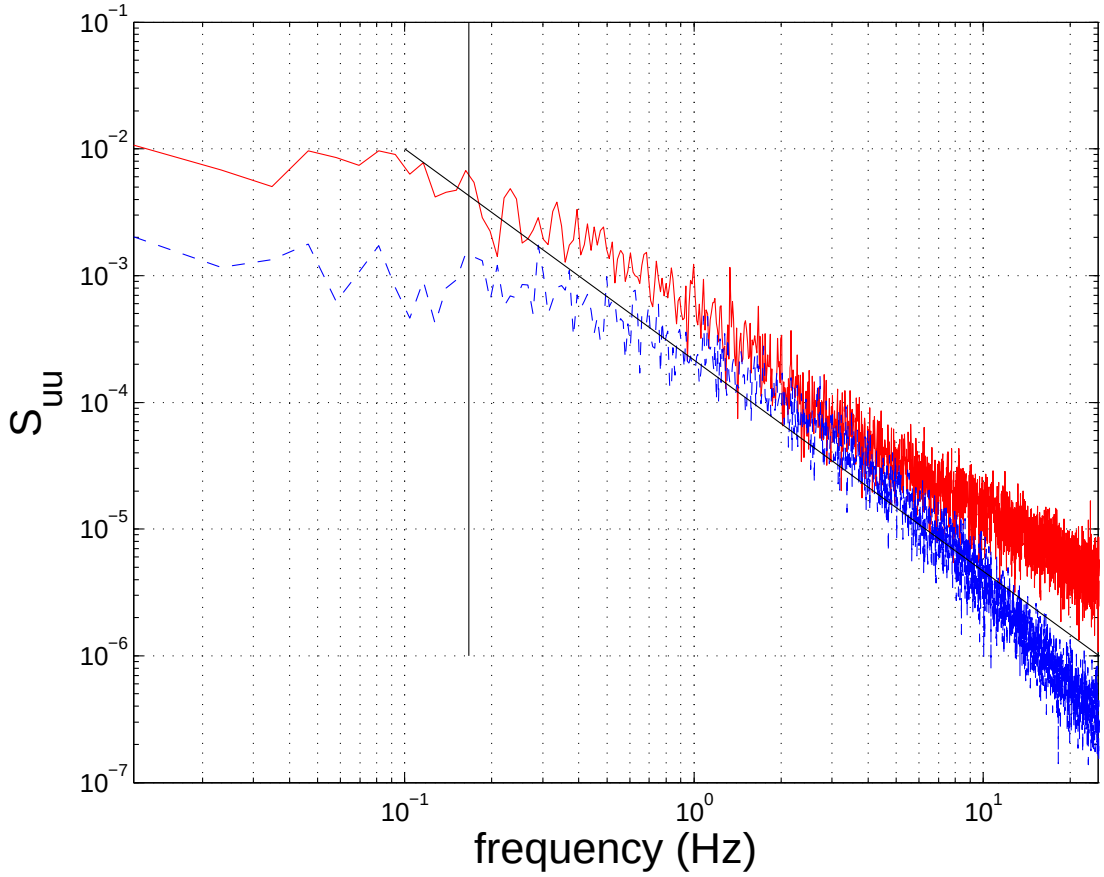

Figure 4.36: Run 6, cart ADV07 spectra located approximately 5 cm above the bed. A -5/3 slope indicative of the inertial subrange is apparent beginning around 1 Hz.

The use of Taylor's Frozen Turbulence Hypothesis is problematic at best in a periodic flow where the mean flow changes sign and its scale is phase dependent, and because of flow reversal goes to zero at some point in the phase. A critical assumption in Taylor's hypothesis is the scale of the turbulent fluctuations is much smaller then the mean flow, i.e. $\sqrt{u'^2} \ll U$, where U is the mean flow. This assumption does not hold in the inner surf zone throughout the phase. Even when this assumption is met (i.e. when the bore front passes) defining an appropriate

scale for U is not a simple task.

Anisotropy of the turbulence at larger scales also makes it inadvisable to use Taylor's hypothesis, although in the dissipative range theory suggests the flow becomes isotropic. Given all of these problems, it is still routinely used in the analysis of turbulence in the surf zone because of it's simple implementation. Cowen et al. (2003) showed under spilling breakers Taylor's hypothesis provided reasonable estimates of spectra while it generally overestimates values for plunging waves. Given the weakly plunging waves in this study, we can expect reasonable estimates of dissipation by invoking Taylor's hypothesis in the present flow, but they are order of magnitude estimates and not exact values.

As a review, Taylor's hypothesis states when the mean flow is large compared to the magnitude of the turbulence, a stationary probe is essentially measuring a "frozen" field of turbulence being advected past the probe, since the time scale associated with the mean flow past the probe is large compared to the turbulence. Using this information we can approximate a spatial derivative using a temporal derivative as

$$\frac{\partial}{\partial t} = U\frac{\partial}{\partial x} \tag{4.9}$$

If the spatial derivative being approximated is $O(5\eta)$, where η is the Kolmogorov length scale, a direct estimate of dissipation can be calculated from its definition in the k-equation and an assumption of isotropic turbulence (generally applicable at the dissipative scale). In a phase averaged sense, this is

$$\epsilon = 2\nu < s_{ij}s_{ij} >= 15\nu \left(< \frac{\partial u_1'}{\partial x} > \right)^2 \tag{4.10}$$

Unfortunately, the ADV records can approximate the spatial derivative by in-

voking Taylor's Hypothesis down to $O(20\eta)$ making the above spatial derivative based estimate unavailable. An alternative does exist, again involving a transition from a temporal to spatial domain, but this time in Fourier space where a spatial spectra is estimated from a temporal (frequency based) spectra, with wave number k defined as

$$k = \frac{2\pi f}{U} \tag{4.11}$$

The temporal, one-dimensional spectra are defined as (Pope, 2000)

$$E_{ij}(\kappa_1) \equiv \frac{1,\pi}{i} nt - \inf, \inf R_{ij}(e_1 r_1) \exp -i\kappa_1 r_1 dr_1 \tag{4.12}$$

Where R_{ij} is the two point velocity correlation. It should be noted that in the present context, there is no difference between the two-sided ($\int -inf, inf$) and one-sided $\int 0, inf$) spectral estimates as long as the variance is preserved correctly when calculating them. The spectra calculated from the ADV records are one-sided spectra. One other point to note is that the limits in the integrals above should in practice be replaced by the Nyquist frequency because aliasing will wrap the energy outside the interval $[-f_n, f_n]$ into this region in measurements, where f_n is the Nyquist frequency.

According to Kolmogorov's hypotheses, at high Reynold's number the high wave number section of the spectra adopts universal forms. Of interest in estimating dissipation is the inertial subrange, which will show up as a flat section of the compensated spectra (Figure 4.37. From the value of $S_{uu}k^{5/3}$ (y-axis), dissipation can be estimated using the 1D spectra (Pope, 2000).

$$E_{uu}(\kappa_1) = C_1 \varepsilon^{2/3} \kappa_1^{-5/3} \tag{4.13}$$

$$E_{ww}(\kappa_1) = C_1' \varepsilon^{2/3} \kappa_1^{-5/3} \tag{4.14}$$

Where the subscripts u and w refer to velocity spectra related to that component. The constants C_1 and C_1' have values of $\frac{18}{55}C$ and $\frac{24}{55}C$ respectively. C is another constant, called the Kolomogorov constant which has been shown experimentally to be 1.5 (Pope, 2000).

Using the above information, for each cart ADV two estimates of dissipation were made, one each from the cross shore and vertical velocity spectra. Results are presented in Figures 4.38 - 4.40. The estimates are in general believable as they are of a reasonable magnitude. Near the surface dissipation increases significantly, and often this value is much larger than the rest of the water column and is off the axes.

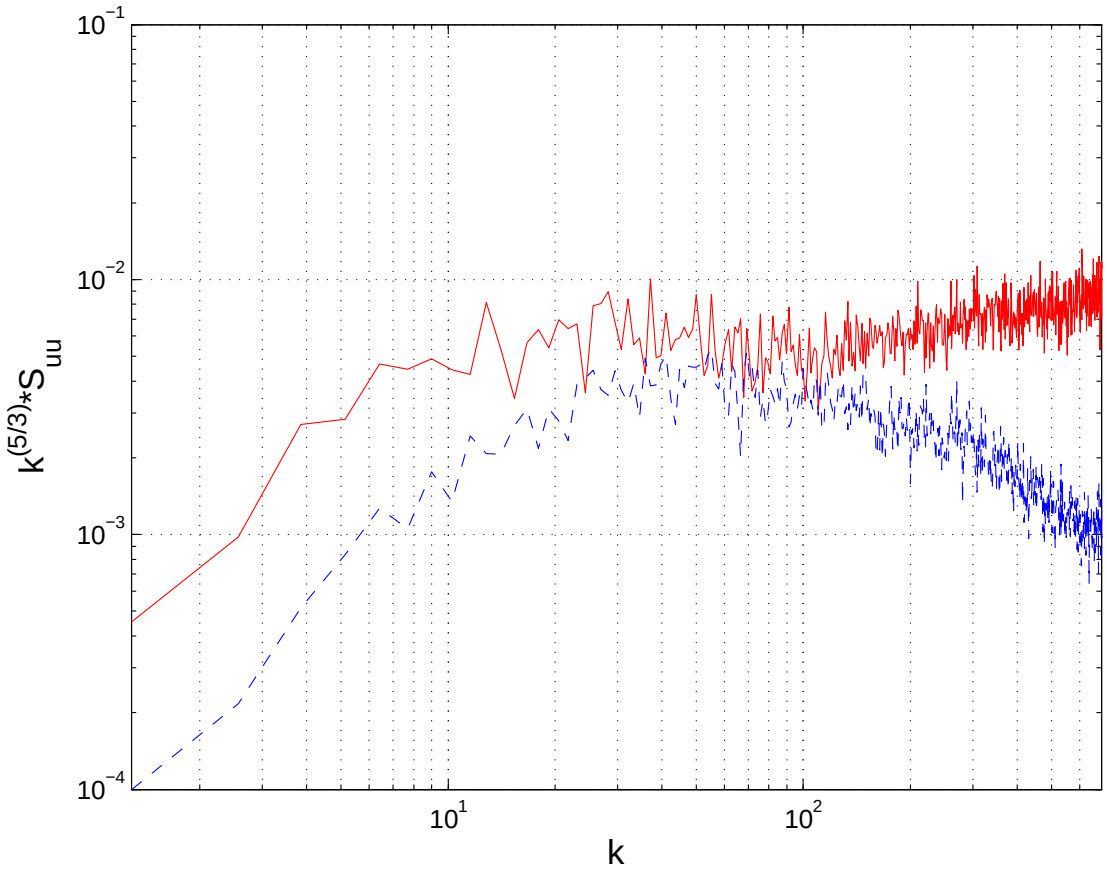

Figure 4.37: Example compensated spectra. The inertial subrange is the flat section in the middle of the plot. The two lines represent the cross shore (−)and vertical components (−−). The lower level for the vertical component is anistropy in the flow.

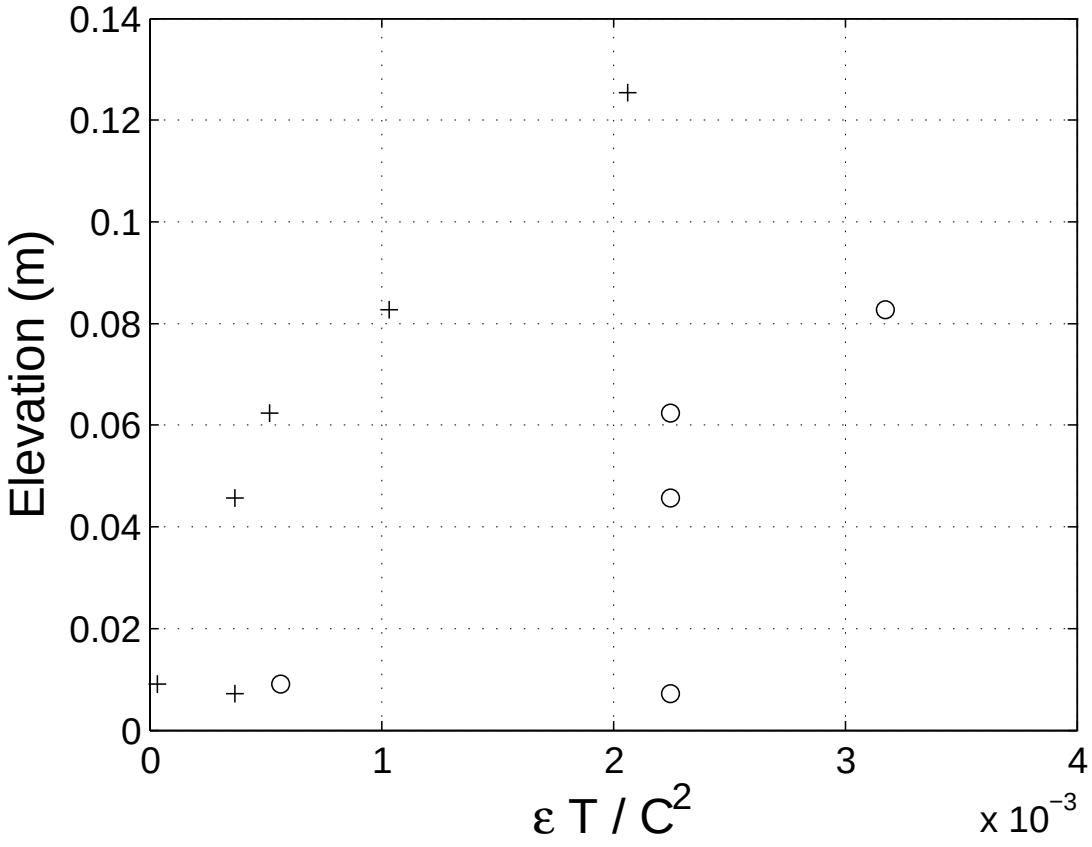

Figure 4.38: Run 6 dissipation profile. The horizontal estimates are marked by ∘ and the verical by +.

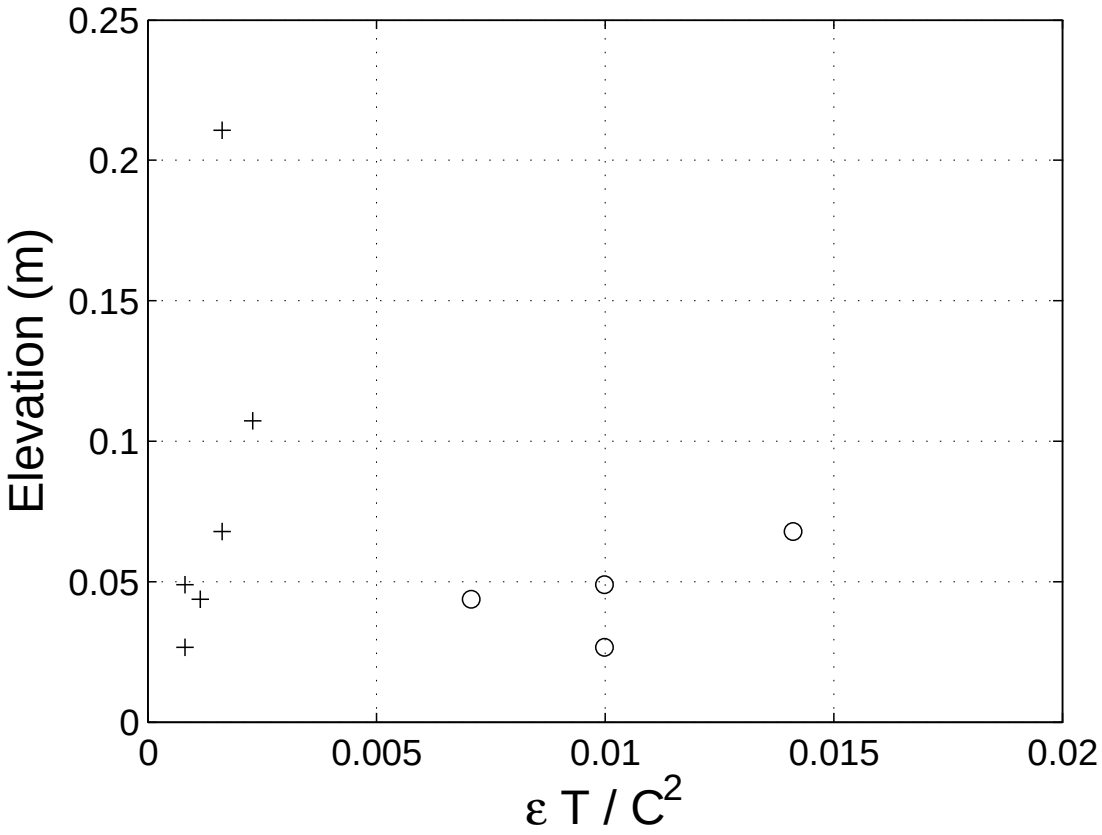

Figure 4.39: Run 16 dissipation profile. The horizontal estimates are marked by ∘ and the verical by +.

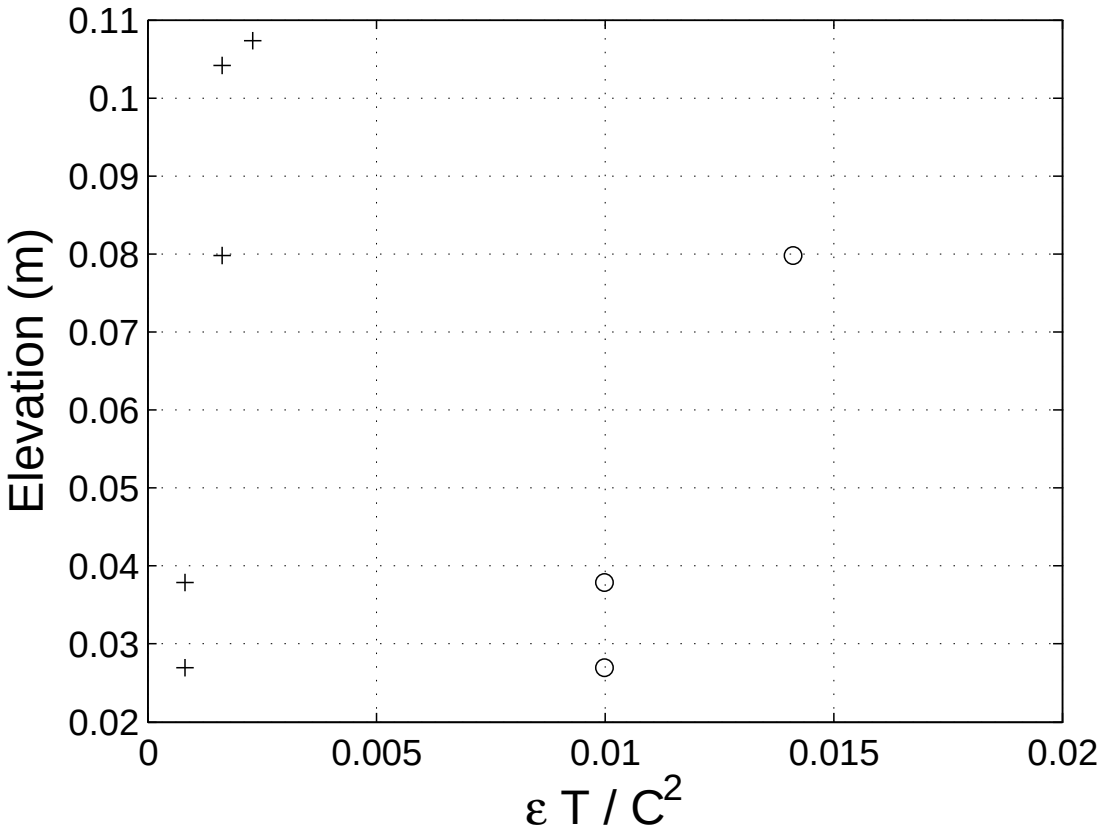

Figure 4.40: Run 21 dissipation profile. The horizontal estimates are marked by ∘ and the verical by +.

Chapter 5

Conclusions

5.1 Recommendations for Future Large Scale Work

Working in the Large Wave Flume or scales similar to it in the lab is a difficult endeavor. Experiments have all of the complexity and variance of field experiments, but also all of the control of a lab experiment. While there are obvious problems with reflection and wall effects from working in a tank (e.g. the bathymetry changes under the cart ADVs), wave conditions can be simplified compared to the field, repeated with varying bathymetry and tuned to create specific conditions. One problem with this is the obvious desire to repeat an experiment to near perfection. While this is a possibility with smaller scale studies, it is nearly impossible at this scale. True repeatability is not possible because of the large number of degrees of freedom (bathymetry being the biggest influence).

The large amount of instrumentation needed to monitor the tank requires constant attention to ensure high data quality. As measurement scales become smaller, the complexity of the instrumentation increases and requires more attention to ensure proper operation. All of these factors and the cost associated with working at large scale necessitates planning and testing of equipment prior to the start of experiments to make the most of the limited time the facilities are available. Having enough people to cover each major station (e.g. swash zone PIV, surf zone velocity/swash auxiliary sensors, offshore velocity, wave paddle/free surface), examine data after each run and alter the setups appropriately would help ensure data quality as well. Of the many problems discovered in the current data, several could have been avoided had either more time been spent on site on first pass

analysis, or more personnel been available to monitor instrument stations.

There is an obvious trade off between personnel and finances in these situations and having enough work to go around. This is one of the sad truths of large scale data collection, it is one of the most dull and unglamorous occupations when things are working, but one of the more stressful occupations when things are not working. It is better to have too many people however since there is always analysis to be done.

Ideally, with proper testing, all equipment will function properly for the duration of an experiment. In reality, this is almost never the case as equipment will break, malfunction, and in general not work properly for no discernible reason. It is important to consider this when planning experiments so that goals are not too lofty and a reasonable schedule is kept that does not generate too much wear and tear on people and equipment. Systems which are new either from a use standpoint (e.g. the Nortek Vectrinos) or from a development standpoint e.g. the buried PIV systems) warrant special attention and should be tested to a reasonable degree prior to using them to collect "real" data.

Specifically for CROSSTEX, more development and testing needed to be done on the entire data acquisition system being deployed prior to experiments beginning. Specific areas which needed attention are the PIV systems and the ADVs used in the surf zone. Both of these pieces of equipment were very new and the lack of familiarity with their operation and reliability negatively impacted data collection efforts. The number of personnel on hand to conduct experiments also could have been increased, allowing more on site examination of data and hopefully improving it's quality from run to run and saving some wear and tear on both personnel and equipment.

While more in depth analysis will show how beneficial working at this scale is to study swash and surf zone processes, there are obvious problems that do not reflect natural beach processes. With larger facilities, with an along shore length scale larger then in the LWF, along shore transport might be easier to eliminate than in the LWF. Stepping the experiments up to field scale in a natural setting would likely prove too costly for a single group to conduct and any efforts to repeat parts of these experiments would best be conducted in collaboration with one or more research groups with specific regions to monitor and some overlap in monitoring capabilities. A more cooperative effort by each of the groups involved might lead to a more refined and complete data set then what is presently available.

5.2 Discussion

Of the 25 runs conducted during the swash zone portion of CROSSTEX, three have been examined extensively in this document. Several others have seen less in depth analysis (average quantities and basic screening). From the data analyzed (free surface, offshore velocity, surf zone velocity and swash zone pressure) the runs have proven to be generally of a repeatable nature for examination of phase averages and suitable for use as driving conditions for use in a numerical model and comparison with model results.

No significant problems have arisen in the analysis in terms of data quality. The most significant problems have been with synchronizing the various instruments and dealing with data gaps. The surf zone ADVs could have improved data quality slightly with some refinement of the setups, but given the number deployed (11 total) the data is overall very good.

Novel measurements such as the buried pressure sensors in the swash zone and

the offshore ADCP have proven to be very successful and with some refinement could easily become fairly common practice for work in wave tanks. The ADCP obviously suffers some constraints here because of its size, but smaller units are available and the technology is continuously advancing. Novel uses such as the application here will provide impetus for manufacturers to consider the research market as both a test bed for new designs and a learning ground for new applications for existing systems. The pressure sensors, with a more careful setup including more exact positions could easily provide critical information of bed mobility, valuable to modelers and experimentalists.

While the flow in the wave tank is 2-D outside the breaker line, the results from the surf zone demonstrate a very 3-D flow. Strong localized bathymetry affects sensors spaced along the shore making a vertical profile almost impossible to construct. Still, phase averaged and turbulent quantities seem to behave in a fairly consistent manner and meaningful conclusions about sediment transport and resuspension can still be made from the data. Finally, the turbulence in the surf zone shows some similarities to prior studies, but does not easily fit into the two well defined regimes discussed by Ting and Kirby (1994). Defining what regime (spilling or plunging) the wave fits into is difficult since there is a vagueness in calculating the descriptive non-dimensional numbers, such as the Iribarren number, over a mobile bed with varying slope and without an exact value for the breaking wave height.

Future work should include a detailed study of the surf zone turbulence, including an attempt to close the k-equation and examination of the OBS measurements for comparison to the ADV backscatter signals. Comparison with model results could also highlight interesting and unexpected features of the flow. The offshore

boundary condition does not require more extensive examination given it's utility and excellent agreement with linear wave theory. Pressure data can be examined alongside the PIV data sets to look at correlations between the pressure gradient, phase and whether accretion or erosion is occurring.

Finally, given the large amount of data still to be examined, several different passes should be employed to narrow focus on either a specific instrument, or a specific region of the tank. Since many runs are available with the same wave height and different bathymetry, a sensitivity analysis on how significantly bathymetry affects the flow could be conducted. Comparison between numerical results and experimental results for these same runs could also reveal shortcomings in the model or instrumentation setup used here. The Swash Zone CROSSTEX data set is probably the most complete data set collected at this scale. With the ability to examine not just mean flow but detailed turbulence measurements at a variety of scales, it is a unique opportunity to examine near shore processes in a relatively controlled environment.

BIBLIOGRAPHY

Bagnold, R., 1954: Experiments on a gravity-free dispersion of large solid spheres in a newtonian fluid under shear. *Proceedings of the Royal Society of London A*, **225**, 49–63.

— 1963: *The Sea: Idea and Observations*, Interscience, chapter Beach and Nearshore Processes: Part 1. Mechanics of Marine Sedimentation. 507–528.

— 1966: An approach to the sediment transport problem from general physics. Technical report, U.S. Geologic Survey.

Baldock, T. and D. Simmonds, 1999: Separation of incident and reflected waves over sloping bathymetry. *Coastal Engineering*, **38**, 167–176.

Battjes, J., 1974: Surf similarity. *Proceedings of the 14th Coastal Engineering Conference*, 466–479.

Beach, R. and R. Sternberg, 1991: Infragravity driven suspended sediment transport in the swash, inner surf, and outer surf zone. *Coastal Sediments*, 114–128.

Beach, R., R. Sternberg, and R. Johnson, 1992: A fiber optic sensor for monitoring suspended sediment. *Marine Geology*, **103**, 513–520.

Blankaert, K. and U. Lemmin, 2006: Means of noise reduction in acoustic turbulence measurements. *Journal of Hydraulic Research*, **00**, 1–15.

Cowen, E. A., I. M. Sou, P. L.-F. Liu, and B. Raubenheimer, 2003: Particle image velocimetry measurements within a laboratory-generated swash zone. *Journal of Engineering Mechanics*, **129**, 1119–1129.

Crossett, K. M., T. J. Culliton, P. C. Wiley, and T. R. Goodspeed, 2005: Population trends along the coastal united states: 1980-2008. Report, NOAA.

Dean, C., 2001: *Against the Tide*. Columbia University Press.

Efron, B. and R. Tibshirani, 1994: *An Introduction to the Bootstrap*. Chapman and Hall.

Frigaard, P. and M. Brorsen, 1995: A time domain method for separating incident and reflected irregular waves. *Coastal Engineering*, **24**, 205–215.

Galvin, C., 1972: Wave breaking in shallow water. *Waves on Beaches and Resulting Sediment Transport*, R. Meyer, ed., Academic Press, 413–456.

Goda, Y. and Y. Suzuki, 1976: Estimation of incident and reflected waves in random wave experiments. *Proceedings of the 15th Coastal Engineering Conference*, 828–845.

Gordon, L. and J. Cox, 2000: Acoustic dopple velocimeter performance in a laboratory flume. Technical report, NortekUSA.

Gordon, R. L., 1996: *Acoustic Doppler Current Profiler Principles of Operation A Practical Primer*. RD Instruments, 9855 Businesspark Ave. San Diego CA 92131, 2nd edition.

Goring, D. G. and V. I. Nikora, 2002: Despiking acoustic doppler velocimeter data. *Journal of Hydraulic Engineering*, **128**, 117–126.

Jarrell(retired), J. D., M. Mayfield, E. N. Rappaport, and C. W. Landsea, 2000: The deadliest, costliest, and most intense united states hurricanes from 1900 to

2000 (and other frequently requested hurricane facts). Technical report, NOAA. URL http://www.nhc.noaa.gov/pastcost.shtml

Katori, S., 1983: Field experiment of sediment transport by streamer and trap. Technical Report 17, NERC.

Kline, S. and F. McClintock, 1953: Describing uncertainties in single sample experiments. *Mechanical Engineering*, 3–8.

Leatherman, S. P., B. C. Douglas, and J. L. LaBrecque, 2003: Sea level and coastal erosion require large-scale monitoring. *Eos Transactions AGU*, **84**, 13. URL http://www.agu.org/pubs/crossref/2003/2003EO020001.shtml

Lohrmann, A., B. Hackett, and L. P. Røed, 1990: High resolution measurements of turbulence, velocity and stress using a pulse-to-pulse coherent sonar. *Journal of Atmospheric and Oceanic Technology*, **7**, 19–37.

Mansard, E. and E. Funke, 1980: The measurement of incident and reflected spectra using a least squares method. *Coastal Engineering*.

Mei, C., 1989: *The applied dynamics of ocean surface waves*. World Scientific.

Pope, S. B., 2000: *Turbulent Flows*. Cambridge University Press, 1st edition.

Scott, C. P., D. T. Cox, S. Shin, and N. Clayton, 2004: Estimates of surf zone turbulence in a large-scale laboratory flume. *Proceedings of the 29th International Conference*, J. M. Smith, ed.

Shaw, W. and J. Trowbridge, 2001: The direct estimation of near-bottom turbulent fluxes in the presence of energetic wave motions. *Journal of Atmospheric and Oceanic Technology*, **18**, 1540 – 1557.

Snyder, W. H. and I. P. Castro, 1999: Acoustic doppler velocimeter evaluation in stratified towing tank. *Journal of Hydraulic Engineering*, **125**, 595–603.

Sou, I. M., 2005: *An Experimental Investigation of Turbulence Structures Within the Surf and Swash Zones*. Ph.D. thesis, Cornell University.

Stacey, M. T., S. G. Monismith, and J. R. Burau, 1999: Measurements of reynolds stress profiles in unstratified tidal flow. *Journal of Geophysical Research*, **104**, 10,933–10,950.

Tennekes, H. and J. L. Lumley, 1972: *A First Course in Turbulence*. The MIT Press.

Thornton, E. B. and R. J. Calhoun, 1972: Spectral resolution of breakwater reflected waves. *Journal of the Waterways, Harbors and Coastal Engineering Division*, **98**, 443–460.

Ting, F. C. and J. T. Kirby, 1994: Observation of undertow and turbulence in a laboratory surf zone. *Coastal Engineering*, **24**, 51–80.

— 1995: Dynamics of surf-zone turbulence in a strong plunging breaker. *Coastal Engineering*, **24**, 177–204.

— 1996: Dynamics of surf-zone turbulence in a spilling breaker. *Coastal Engineering*, **27**, 131–160.

Trowbridge, J., 1998: On a technique for measurement of turbulent shear stress in the presence of surface waves. *Journal of Atmospheric and Oceanic Technology*, **15**, 290–298.

Wahl, T. L., 2003: Discussion of "despiking acoustic doppler velocimeter data" by derek g. goring and vladimir i. nikora. *Journal of Hydraulic Engineering*, **129**, 484–487.

Watts, G., 1953: Field investigation of suspended sediment in the surf zone. *Proceedings of the 4th Internation Conference on Coastal Engineering*, 181–199.